# Analytical electron microscopy studies of grain boundary segregation and embrittlement.

# INFORMATION TO USERS

This manuscript has been reproduced from the microfilm master. UMI films the text directly from the original or copy submitted. Thus, some thesis and dissertation copies are in typewriter face, while others may be from any type of computer printer.

**The quality of this reproduction is dependent upon the quality of the copy submitted.** Broken or indistinct print, colored or poor quality illustrations and photographs, print bleedthrough, substandard margins, and improper alignment can adversely affect reproduction.

In the unlikely event that the author did not send UMI a complete manuscript and there are missing pages, these will be noted. Also, if unauthorized copyright material had to be removed, a note will indicate the deletion.

Oversize materials (e.g., maps, drawings, charts) are reproduced by sectioning the original, beginning at the upper left-hand corner and continuing from left to right in equal sections with small overlaps. Each original is also photographed in one exposure and is included in reduced form at the back of the book.

Photographs included in the original manuscript have been reproduced xerographically in this copy. Higher quality 6" x 9" black and white photographic prints are available for any photographs or illustrations appearing in this copy for an additional charge. Contact UMI directly to order.

**UMI**

A Bell & Howell Information Company
300 North Zeeb Road, Ann Arbor MI 48106-1346 USA
313/761-4700 800/521-0600

# ANALYTICAL ELECTRON MICROSCOPY STUDIES OF GRAIN BOUNDARY SEGREGATION AND EMBRITTLEMENT

by

Vicki J. Keast

Presented to the Graduate and Research Committee

of Lehigh University

in Candidacy for the Degree of

Doctor of Philosophy

in

Materials Science and Engineering

Lehigh University

21st August, 1998

Approved and recommended for acceptance as a dissertation in partial fulfillment of the requirements for the degree of Doctor of Philosophy

8/21/98
Date

Dissertation Director

8-28-98
Accepted Date

Committee Members

Name of Committee Chair

Name of Committee Member

Name of Committee Member

Name of Committee Member

## ACKNOWLEDGMENTS

Firstly and foremostly I would like to thank Professor David B. Williams for being the best advisor a girl could ask for. Professor Williams provided me with unlimited support, encouragement and guidance and yet allowed me the freedom to direct my own research. I am very grateful for the opportunities he has given me to further both my professional and personal development, not to mention being responsible for my coming to Lehigh in the first place. My experience here has been very rewarding and this is in no small way due to Professor Williams, his indomitable cheerfulness and the esteem and admiration with which I regard him.

Thank you also to my committee members, Professor Katy Barmak, Professor Jeffrey M. Rickman and Professor David E. Luzzi, for their willingness to be involved in this work and the feedback they have provided. Dr. John Bruley taught me just about everything I know about EELS and most of what I know about STEM, for which he has my eternal gratitude. It would have taken me twice as long to complete this work if it were not for the headstart John gave me. Dr. Masashi Watanabe was an irreplaceable resource and the answer to any question about XEDS is "Masashi will know". Thanks Masashi for being an extra pair of hands and brain during the probe size measurements. More importantly I thank Masashi for his warm, sincere friendship and for being my "big brother" and confidant.

This work could never have been done if it were not for the technical staff. I bow down and worship the ground Dave Ackland walks on. Mainly because he kept the VG 603 running for the whole time I was here (a feat that should be entered in the Guinness book of records). But also for his willingness to help with any problem and his calmness in the face of potential disaster ("which valve was I supposed to open?").

Kathy Repa, Arlan Benscoter and Andrea Pressler provided help in ways too numerous to count. But Kathy, it was your friendship and our chats that have kept me sane in this place!

Acknowledgments to the various groups who have provided material and samples; D. E. Luzzi of University of Pennsylvania, J. D. Embury of Los Alamos National Laboratory, D. M. Symons of Westinghouse-Bettis, L. -S. Chang and U. Alber of the Max-Planck Institut.

Thanks also to the other graduate students for their friendship, more than a few laughs (and debates) over the last few years and for providing the support that can only come through shared experience. Special mention goes to Derrick Carpenter for many many hours of conversation and mutual procrastination. We may not have solved the worlds problems, but he at least helped me understand some microscopy ones a little better. Having someone to bounce my ideas off was an invaluable help. Others that deserve mention; Anthony DiGiovanni, Jason Goodelle, Gene Lucadamo, Roger Ristau, Adam Scotch, Paul Sheedy, Gary Thompson and Dave Whittle, all of whom were willing to listen when I was feeling chatty. Acknowledgments to my companions on the 3 pm WaWa walk - you know who you are!

There are number of people to thank in my refuges away from the lab. Thanks to the girls of 535 Montclair for 2 years of fun and companionship and to my yoga teacher, Mary Rosenberger, for the hours of relaxation and for helping me refresh my outlook on the world.

Finally I would like to thank all the members of my family for their love, understanding and support. I hope in some small way this document will justify why I had to leave.

## CONTENTS

## LIST OF TABLES

## LIST OF FIGURES

## ABSTRACT

Grain boundary segregation and embrittlement in a number of systems has been investigated using analytical electron microscopy (AEM) techniques. Segregation to grain boundaries has been observed using X-ray energy dispersive spectroscopy (XEDS) with an unprecedented spatial resolution and sensitivity. 2D X-ray mapping of compositional distributions has been shown to be applicable to the case of equilibrium segregation and such maps contain the same information as can be obtained with other, more traditional, approaches. In addition to studies of the embrittling systems S-doped Ni and Bi- and Sb-doped Cu, Ag, which does not embrittle, has been observed at grain boundaries in Cu, the first direct measurement of Ag segregation in Cu.

Changes in the electronic structure, and hence bonding, at the grain boundaries in the presence of the segregants has been examined using the electron energy loss near edge structure (ELNES). In the embrittling systems of S-doped Ni and Sb-doped Cu, extra intensity in the ionization edge, just above the edge onset, was observed and is consistent with earlier measurements on Bi-doped Cu. No effect was seen with segregation of the non-embrittling Ag. The embrittling impurities are believed to reduce cohesion at the grain boundaries by changing the shape of the d-band, through bond rehybridization, and it is this change in shape that is observed as the extra intensity in the ELNES.

# 1. INTRODUCTION

The segregation of impurities to grain boundaries, often associated with a change in material properties, is a well known phenomenon. Although the technique of choice to examine segregation is often Auger electron spectroscopy (AES), analytical electron microscopy (AEM) techniques are also well developed and offer a number of advantages. One of the principal advantages of AEM over AES is that the sample does not need to be fractured, allowing examination of non-brittle grain boundaries.

X-ray energy dispersive spectroscopy (XEDS) is most often used to examine grain boundary segregation in the AEM and until recently, there were three main approaches to obtaining segregation information. Placing the small electron probe at the grain boundary while collecting an X-ray spectrum gives the maximum sensitivity for detection of the segregating species. Rastering the probe over a fixed area while collecting the spectrum allows for more accurate quantification, but with reduced detection sensitivity. Finally, a profile of segregant distribution perpendicular to the grain boundary can be obtained. Each of these approaches will be used in this work, where appropriate, and a detailed analysis of resolution, sensitivity and quantification will be given.

In addition to the traditional approaches, recent improvements in instrumentation, as implemented on the VG 603 at Lehigh University, have meant that it is now possible to obtain 2D maps of segregant distribution. The application of X-ray mapping to grain boundary segregation will be examined here and the information available in a map will be compared to that available by the other approaches.

Identifying and quantifying segregants at a grain boundary does not answer the questions regarding the effect segregants have on material properties and, in particular, why some segregants cause grain boundary embrittlement (GBE) and others do not. Even though the phenomenon of GBE has been identified of for many years, and there has been a great deal of experimental and theoretical work performed in an attempt to understand it better, the mechanism by which some impurities reduce the cohesion at the grain boundary has remained essentially unkown. In the last 2-3 years, experiments in the AEM, using electron energy loss spectroscopy (EELS), have shown that this technique is able to provide information about changes in bonding at grain boundaries.

The fine structure on the ionization edges in the EEL spectrum (called the electron energy loss near edge structure or ELNES) is directly related to the unoccupied density of states (DOS). Changes in the DOS will reflect changes in bonding and therefore the ELNES can provide bonding information. Examination of changes in the ELNES at grain boundaries containing an embrittling impurity can indicate how the segregant has weakened the bonding at the grain boundary.

In this work, the chemistry and bonding at grain boundaries in a number of different materials have been examined. Bi-doped Cu is a classic embrittling system and was the focus of earlier ELNES studies and the segregation studies will be extended here. Other dopants in Cu to be examined are Sb and Ag. Although Sb and Ag have similar atomic sizes, Sb, like Bi, embrittles Cu, while Ag does not. Comparisons of the effect on the electronic structure at grain boundaries due to segregation of these two species will help ensure that any changes in the near edge structure are actually associated with embrittlement. In addition the segregation of Ag to grain boundaries in Cu has never been directly observed, only inferred from diffusion studies or surface segregation studies. Another well known embrittling system, S-doped Ni, will also be examined,

and in this case the segregating impurity is smaller in atomic size than the matrix element.

In summary, there are two main goals of the research to be discussed here. Firstly, the unique microanalysis capabilities of the VG 603 dedicated STEM will be used to push the limits of resolution and detectability in segregation studies in the AEM. Secondly, by examining the ELNES of a number of embrittling and non-embrittling systems, a better understanding of the mechanisms for GBE will be attained.

# 2. BACKGROUND

## 2.1 Grain-Boundary Segregation

Grain-boundary segregation occurs when an excess concentration of an impurity or alloying element collects at the grain boundaries, usually after the material has been through some specific heat treatment. In many cases the segregating element will alter the properties at the grain boundary, and can thus significantly affect the bulk material properties. Sometimes impurity elements are deliberately added during processing to enhance the material properties. For example, the segregation of Y and La to grain boundaries in alumina improves the creep resistance (Cho et al. (1997)) and reduces the densification rate (Fang et al. (1997)). Cu is added to Al lines in interconnects in semiconductor devices to reduce susceptibility to failure by electromigration (Ames et al. (1970)). Segregating impurities can also have undesirable effects on material properties. Segregation can increase the tendency for grain boundary failure, for example through grain boundary embrittlement or intergranular stress corrosion cracking (Hondros and Seah (1977)). GBE is the subject of this thesis and will be reviewed in more detail in the next section. A segregating element does not necessarily have any influence on material properties. For example, Ag is known to segregate to the grain boundaries in Cu, but there has been no reported change in properties due to segregation.

Segregation is a consequence of a thermodynamic driving force and is thus reversible. Description of the segregation phenomenon has been found amenable to relatively simple thermodynamic theories (Hondros and Seah (1977)). There is a less common class of segregation phenomena termed non-equilibrium segregation, that is irreversible and arises from kinetic effects, but will not be discussed here. An understanding of the

origins for the driving forces for segregation may be understood when it is noted that there is a general correlation between high segregation levels and low solid solubility. Figure 2.1 shows a plot of the enrichment ratio, which is a measure of the grain boundary excess concentration, against solid solubility for number of binary systems (Hondros and Seah (1983)). This correlation suggests that the Hume-Rothery rules, which govern solid solubility, must also be important in determining segregation behavior.

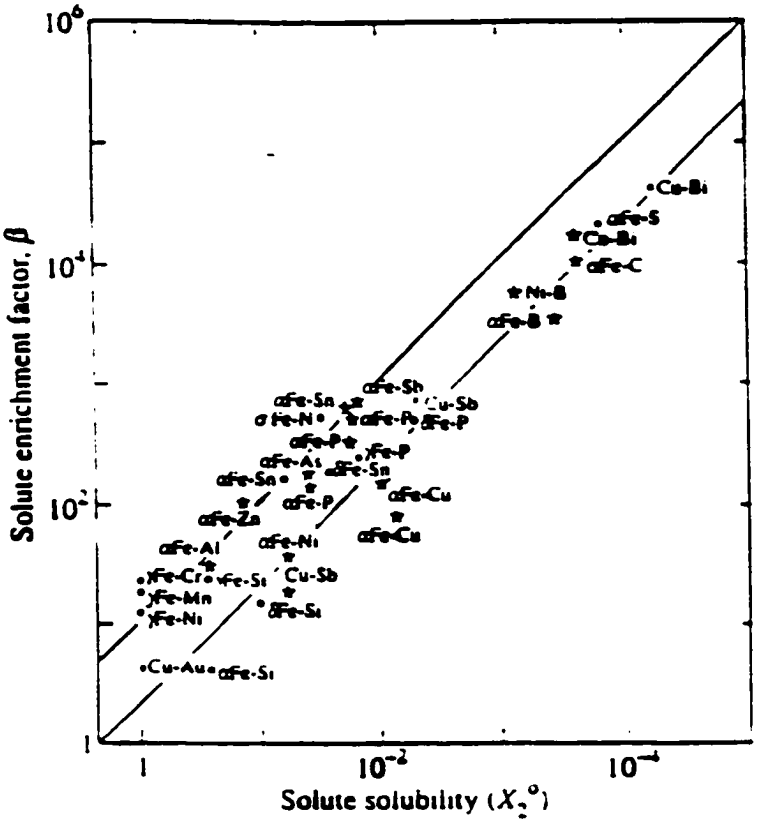


Figure 2.1 Experimentally determined enrichment ratios for various systems plotted against solid solubility (from Hondros and Seah (1983)).

The Hume-Rothery rules state that if two atomic species have either

i) a large atomic size difference

ii) a large valency difference

iii) a large electronegativity difference

then they will not form a solid solution. The application of the first condition to segregation is readily understandable because the extra free volume at the grain boundary provides atomic sites that can accommodate a size misfit. The other two conditions refer to a chemical incompatibility such that the two materials would prefer to form a compound. Briant (1990) has interpreted this to mean that there may be more favorable bond geometries, similar to those found in the compounds, at the grain boundary than in the bulk. Although, qualitatively, there is an inverse relationship between solid solubility and segregation levels, Briant (1996) has shown that there is no quantitative, predictive relationship.

Most of the thermodynamic descriptions of segregation are based on solid-state analogues of gas-adsorption theories and reviews can be found in a number of sources (for example, Hondros and Seah (1977), Lejcek and Hofmann (1995)). The simplest and earliest approach was taken by McLean (1957), based on Langmuir-type adsorption. It is assumed that there is only one element segregating and a fixed number of identical and non-interacting segregation sites. This approach results in a segregation isotherm, often called the McLean isotherm

$$\frac{X_B}{X_{B_0} - X_B} = \frac{X_C}{1 - X_C} \exp\left(\frac{E_l}{RT}\right) \qquad (2.1)$$

where

$X_B$ = boundary concentration

$X_{B_0}$ = saturation boundary concentration

$X_C$ = bulk concentration

$E_l$ = grain boundary adsorption energy

R = universal gas constant

T = temperature

The theory predicts, as expected, that segregation increases with decreases in temperature and increases in solute concentration, up to some saturation level. The predictive ability of the theory is limited because calculation of the adsorption energy is not always easily performed.

An alternate approach is based on the truncated Brunauer, Emmett and Teller (BET) theory, a simplification of the full BET theory applied to the case of monolayer segregation. In this case, the theory was developed using statistical mechanics, but with the same assumptions described in the McLean theory. The solid-state expression for this approach is given by

$$\frac{X_B}{X_{B_0} - X_B} = \frac{X_C}{X_{C_0}} \exp\left(\frac{E}{RT}\right) \tag{2.2}$$

where $X_{C_0}$ is the solute molar fraction at the solubility limit. The energy term E is now the difference between the free energy of adsorption of the first layer and the free energy of condensation of the subsequent layers and is a term that is more easily estimated. The McLean and truncated BET models both assume monolayer levels of segregation, whereas the full BET theory allows for multilayer segregation. The solid-state analogue of the full BET theory may be written

$$\frac{X_{B_0}}{X_B} \frac{X_C}{X_{C_0} - X_C} = \frac{1}{K} + \frac{K-1}{K} \frac{X_C}{X_{C_0}} \tag{2.3}$$

where K=exp(E/RT). For many systems segregation levels are on the order of a monolayer, but multilayer segregation has been observed, for example, in the Fe-Sn system (Seah and Hondros (1973)) and was well described by the multilayer BET theory.

The next level of complexity is called Fowler theory (Fowler and Guggenheim (1939)) and allows for site-to-site interactions and introduces an interaction energy, $\omega$, between nearest neighbors. The segregation isotherm becomes

$$\frac{X_B}{X_{B_0} - X_B} = X_C \exp\left[\frac{E_l - c\omega\left(X_B/X_{B_0}\right)}{RT}\right] \qquad (2.4)$$

which reduces to the McLean isotherm for $\omega = 0$. Expressions have also been developed to describe multicomponent systems, but, as may be expected, they are considerably more complex. The similarity in appearance of the different expressions 2.1 - 2.4 is by no means coincidental. In fact, as described by Lejcek and Hofmann (1995), they all have their basis in a common, general segregation equation, and it is the simplifying assumptions that are chosen that give rise to the different expressions. The appropriate choice of segregation isotherm will depend on the system under investigation. The McLean isotherm being the first and simplest has most frequently been applied, for example to Cu-Sb (Chuang et al. (1982), Bokstein et al. (1993)), Fe-Sb (Mast et al. (1996)), Ni-S (Mulford (1983)) and Cu-Bi (Michael and Williams (1984)), although a recent investigation on the Cu-Bi system suggested that the a two-layer Fowler-type isotherm may be appropriate (Chang et al. (1997)).

One problem with such thermodynamic treatments is that they assume that segregation levels are the same to all grain boundaries, whereas usually there is a spectrum of segregation levels depending on grain-boundary crystallography. The Cu-Bi system, displays a large degree of anisotropy, first observed by Powell and Woodruff (1976) to be much larger than had previously been seen in the Fe-Sn and Fe-S systems. Further studies on Bi-doped, <100> Cu bicrystals confirmed that segregation levels vary with grain-boundary misorientation (Fraczkiewicz and Biscondi (1985)). It is not surprising that segregation levels are highly dependent on grain-boundary crystallography, as it can

easily be imagined that there are certain grain boundary structures which have a larger number of favorable sites for segregation. One limiting case is that of coherent twin boundaries, in which there would be no sites for segregation, and it is generally believed that segregation does not occur at coherent twin boundaries. One example of segregation to a coherent twin boundary in Cu-Bi has been described (Luzzi et al. (1991)) and this will discussed in more detail in Section 6.4.

In general, low-angle boundaries have low levels of segregation, which increase monotonically with misorientation up to around 15°. This would be expected if it is assumed that the impurity elements prefer to reside at the areas of large atomic misfit around dislocation cores. It might also be expected that grain boundaries with a low $\Sigma$ value (where $\Sigma$ is the reciprocal of the density of coincidence site lattice points) would have lower levels of segregation than random, high-angle boundaries. These boundaries have high symmetry and lower interfacial energy and therefore potentially fewer energetically favorable segregation sites. However, no systematic variation of segregation levels with $\Sigma$ has been observed. An explanation may lie in the fact that the orientation of the grain boundary plane, not only the misorientation between the grains, is of importance in determining the segregation sites available in the grain boundary plane. An investigation into anisotropy in the Ni-S system (Bouchet and Priester (1986)) proposed that it is the atom density in the grain boundary plane which is the determining factor for segregation levels (high density = low segregation). Lejcek and Hofmann (1995) reviewed the role of grain boundary crystallography on segregation for many systems and concluded that there is no simple geometric parameter that can be used to explain or predict segregation levels. Understanding of the relationship between grain boundary structure and segregation is complicated by the fact that the segregation itself can cause rearrangement of the grain boundary. Grain boundary faceting has been

observed and is reversible upon desegregation (Donald and Brown (1979), Ference and Ballufi (1988)). Anisotropy of segregation and faceting could be described as two aspects of the same concept, that certain grain boundary structures can more easily accommodate segregants. In one case the segregant goes to the most energetically favorable boundary, and in theother case the segregant rearranges the boundary into a more energetically favorable structure.

In order to better understand the role of atomic structure at grain boundaries, and more recently, the effect of segregation on atomic structure, a number of atomistic studies have been performed. Most of the studies have focused on identifying which sites in a relaxed grain boundary structure are most favorable for segregation. As an example, the segregation of Bi to the $\Sigma$=5 (310) boundary in Cu was investigated and the atomic sites with high segregation energy identified (Vitek et al. (1993)). Recent experimental investigation of this structure using high-angle, annular dark-field imaging (HAADF or Z-contrast imaging) in the STEM confirmed the validity of this structure (Chisolm, private communication). Interestingly, similar and separate atomistic studies of Sb (Chang et al. (1984)) and Ag (Menyhard et al. (1994)) segregation to the same $\Sigma$=5 (310) Cu grain boundary gave the same segregation sites. Bi, Sb and Ag all segregate to the same sites in this grain boundary structure but Bi and Sb both embrittle Cu, while Ag does not. This suggests that the structural rearrangements at the grain boundaries are not important in determining the changes in properties upon segregation. Sb and Bi both have partially filled p shells but Ag, like Cu, has a full d shell and partially filled s shells, which suggests that electronic effects are probably responsible for embrittlement. Understanding the segregation process does not necessarily lead to an understanding of how the segregant has changed the properties at a grain boundary.

## 2.2 Grain Boundary Embrittlement (GBE)

GBE occurs when the segregating impurity in some manner reduces the cohesion at the grain boundary and the material now fails in a brittle manner, via intergranular fracture. Very small bulk concentrations of impurity elements, when allowed to segregate, can result in high concentrations at the grain boundaries and thus drastically alter the cohesion. The impurity levels that can produce embrittlement are sometimes below the levels of control in commercial practices and it is for this reason that the phenomenon of GBE is of particular concern to industry.

The temper embrittlement of steels is perhaps the most industrially important example of GBE and it occurs after the steel has been annealed, used or cooled through a particular temperature range (usually 350-600 °C). The large number of alloying elements and potential embrittling impurities in Fe and Fe alloys has made a comprehensive understanding of temper embrittlement difficult. However, P, S, As and Sb have all been associated with temper embrittlement, with P being the most common. The alloy composition has a very strong influence on the degree of embrittlement with Ni, Cr and Mn generally promoting, and Mo reducing, embrittlement. Although the interactions between impurity and alloying elements is quite complex, it was pointed out by Bulloch (1994) that the primary factor in P embrittlement of steels is the level of P segregation and the various effects of alloying elements, microstructure and temperature is just to alter the P segregation levels.

The embrittlement of Cu by Bi is a classic example of GBE and was first documented by Hampe (1874). Unlike some other systems, it is a simple case in which only the two elements, Cu and Bi, are involved. It is the combination of simplicity and historical significance which makes the Cu-Bi system one of the more extensively studied

embrittling systems. Investigations whose purpose is to gain a better understanding of the general phenomenon of GBE often use the Cu-Bi as a model system. The problem of ensuring that Bi does not contaminate Cu is one that is still of concern to industry today (Hoffmann (1994), Piret (1994), Serrano et al. (1994)). Voce and Hallowes (1947) were the first to suggest that the brittleness of Bi-doped Cu was due to a film of Bi at the grain boundaries and, in a discussion of this paper, McLean (1947) suggested that segregation was responsible. Direct confirmation of segregation did not appear until the development of Auger electron spectroscopy (AES) and the Cu-Bi system was among the earliest examined using this technique (Joshi and Stein (1971)). There is evidence that Sb and Te also embrittle Cu and Cu alloys (McLean (1952), Marcus and Paton (1974)), although the investigations into these two systems are not as extensive as for the Cu-Bi system. Very little is known about Cu-Te in particular.

It had been known for some time that S impurities in Ni could cause embrittlement (Merica and Waltenberg (1925)), but once again it was not until 1974 that segregation was directly confirmed using AES (Johnson (1974)). The question of embrittlement of Ni by S is a little more complex in that there are still questions regarding environmental effects. It is well established that segregation of S promotes H embrittlement in Ni (Jones et al. (1980)), but Hagiwara and Chene (1984) found Ni to be ductile when not charged with H, even in the presence of S. More recent investigations (Lassila and Birnbaum (1987)) found that low S concentrations enhanced H embrittlement and that the Ni did indeed remain ductile when not charged with H, but for high S concentrations, brittle intergranular fracture occurred, even without H charging. So, even though it does appear that S can embrittle Ni without H, given the experimental difficulties in directly detecting H in a material, there may always remain questions as to the role H in the embrittlement process.

It should also be noted that impurities that segregate to the grain boundaries do not necessarily induce embrittlement. For example, Ag segregates to Cu grain boundaries but does not embrittle them. At the other extreme, $Ni_3Al$ boundaries are intrinsically brittle, but become ductile on the segregation of B (Aoki and Izumi (1979)). In general, the materials that are embrittled are transition metals (Fe, Ni, Cu) and their alloys and the embrittling species come from group IV, V or VI of the periodic table (Sn, P, As, Sb, Bi, S, Te). Any explanation as to the mechanism for GBE should account for these trends. It should also account for the cases where a co-segregant reduces embrittlement. For example, co-segregation of Ti in Ni-Cr steels has been observed to mitigate the effect of Sb embrittlement (Ohtani et al. (1976)) and similarly Mo counteracts the effects of P in intergranular embrittlement of Fe (Kimura et al. (1986)).

It is well established that the severity of embrittlement generally increases with the increasing bulk concentrations of impurities. As the bulk concentration of impurity rises, the excess concentration at the grain boundary also increases, at least up to some saturation value (cf. the segregation isotherms in Section 2.1), and the material becomes more brittle (Joshi and Stein (1971), McMahon (1976), Loier and Boos (1981), Li et al. (1990), Bulloch (1994)). Mechanical behavior investigations on bicrystals have shown that the severity of grain boundary embrittlement is also dependent on grain boundary crystallography (Chuang et al. (1982), Russell and Winter (1985), Miura et al. (1993), Miura et al. (1994)). There is some evidence that the low-energy, low-$\Sigma$ boundaries are less embrittled than random boundaries, as are low angle boundaries. It is highly conceivable that differences in degree of embrittlement between grain boundaries of different crystallography are purely due to different segregation levels between these boundaries. However, a complete set of experiments that tie together crystallography, segregation levels and mechanical properties has not yet been performed. An attempt

was made by Chuang et al. (1982) with bicrystals in the Cu-Sb system. However, the segregation levels in this study were measured using AES and uncertainties in the fracture path limited knowledge about segregation to the non-brittle grain boundaries.

## 2.3 Mechanisms for GBE

Once it was determined that grain-boundary segregation was responsible for embrittlement, and that deleterious segregants could be routinely identified using AES, questions arose as to the mechanism for GBE. It would be tempting to state simply that the impurities weaken the bonding at the grain boundary and therefore reduce grain-boundary cohesion. However, the matrix material is usually a ductile material and (Hondros and McLean (1974)) showed that, at least for the case of Bi in Cu, the ductile behavior within the Cu grains is unchanged by the presence of Bi; i.e. dislocations remain free to move through the grains as before. Therefore the interaction of dislocations with the grain boundary should also be considered.

There is evidence, both in S-doped Ni (Floreen and Westbrook (1969)) and B-doped $Ni_3Al$ (Schulson and Baker (1992)) that the slope of the Hall-Petch relation is influenced by the segregation of impurities. In other words, the effectiveness of the grain boundary in transmitting slip has been altered by the segregant. During straining, dislocations will pile up at a grain boundary at the head of a slip band. The boundary can accommodate the local stress intensity by the formation and movement of grain boundary dislocations or by the emission of dislocations from grain-boundary dislocation sources into the other grain. A segregating impurity may change the way both of these processes occur. In-situ TEM deformation studies in Ni-S (Lee et al. (1989)) and $Ni_3Al$-B (Lee et al. (1991)) have shown that the dislocation behavior was unaltered by segregation, ductile alloys relieved stress concentrations by slip

transmission and brittle alloys through intergranular cracking. A change in cohesion at the grain boundary was suggested to be the reason for the different behavior.

Once an atomically sharp grain-boundary crack has been nucleated, whether it will propagate depends upon a trade off between dislocation emission blunting the crack tip and atomic decohesion propagating the crack. Calculations and experiment (Mason (1979), Wang and Anderson (1991)) have revealed that the dislocation emission process and the availability of slip planes could explain the experimentally observed variation (Russell and Winter (1985), Wang and Anderson (1991), Miura et al. (1993)) in the degree of embrittlement with grain-boundary misorientation. However, it is the reduction in grain boundary cohesion that determines the transformation from crack-tip blunting to crack propagation for a given grain boundary structure.

The conclusion that can be drawn is that, although the ductile behavior is important in the fracture process it is the reduction in cohesion at the interface that is the determining factor in grain-boundary embrittlement.

Using the Griffith approach the stress, $\sigma_F$, at which a crack, length c, begins to propagate in a material of elastic modulus E is given by

$$\sigma_F = \left(\frac{2E\gamma'}{\pi c}\right)^{1/2} \tag{2.5}$$

where $\gamma'$ is the energy required per unit area of surface created and $\gamma'=w_{rev}+\gamma_p$, where $\gamma_p$ is the plastic work, and the reversible work of fracture for a grain boundary is,

$$w_{rev}=2\gamma_s-\gamma_b \tag{2.6}$$

and $\gamma_s$ and $\gamma_b$ are the surface and grain boundary energies respectively. As discussed above, the plastic work term is not considered important when describing the change in

cohesion due to GBE. Hondros and McLean (1974) measured surface energies of Cu, for a number of Bi concentrations, using the thin-foil zero-creep technique and grain boundary energies using dihedral angles of thermally etched boundaries. They then applied equation 2.6 to determine the energy for fracture and how this energy behaves with Bi content. They found that both the surface energies, $\gamma_s$, and grain boundary energies, $\gamma_b$, decrease with Bi concentration, but the net result was a reduction in $w_{rev}$ ($w_{rev}$(CuBi)/$w_{rev}$(Cu) = 0.55) and therefore also cohesion. Measurement of surface and grain boundary energies for Cu doped with Sb were made by Inman et al. (1963), although they did not apply these values to equation 2.6. When their values for $\gamma_s$ and $\gamma_b$ are inserted into equation (2.6) it gives $w_{rev}$(CuSb)/$w_{rev}$(Cu) = 0.50. In other words, a reduction in grain boundary cohesion of around 50% is sufficient to produce embrittlement.

An alternate approach is to describe the ideal work of reversibly separating an interface against atomic cohesion as being equal to the area under the stress-displacement curve and therefore

$$w_{rev} = \int_0^\infty \sigma d\delta \qquad (2.7)$$

It can be shown (Hirth and Rice (1980), Rice and Wang (1989)), assuming rapid separation with a fixed amount of non-mobile segregant, $\Gamma$, and equilibrating chemical potential $\mu$, that equation 2.7 leads to

$$w_{rev} = \gamma_0 - \int_0^\Gamma \{\mu_b(\Gamma) - \mu_s(\Gamma/2)\} d\Gamma \qquad (2.8)$$

where $\gamma_0$ is the work to separate the interface with no segregant ($\Gamma$=0). This expression links the reduction in cohesion to quantities which, in principle. can be obtained from

solute segregation studies. To proceed further, the McLean model can be adopted, where the chemical potentials are represented by

$$\mu_b(\Gamma_b) = \Delta g_b^0 + RT \ln\left\{\Gamma_b / \left(\Gamma_b^{max} - \Gamma_b\right)\right\} \tag{2.9}$$

$$\mu_s(\Gamma_s) = \Delta g_s^0 + RT \ln\left\{\Gamma_s / \left(\Gamma_s^{max} - \Gamma_s\right)\right\} \tag{2.10}$$

These are substituted into equation 2.8, and the ln() terms in the resultant expression are usually small enough to be neglected to give

$$w_{rev} = \gamma_0 - \left(\Delta g_b^0 - \Delta g_s^0\right)\Gamma \tag{2.11}$$

where the $\Delta g_s$ and $\Delta g_b$ terms are the segregation energy of the impurity from the bulk to the surface and grain boundary respectively. According to this analysis, the determining factor in GBE is the relative free energies of segregation between the surface and grain boundaries. Rice and Wang (1989) made an attempt, using the available experimental data for impurities in Fe, to correlate segregation energy differences to embrittlement sensitivity. However, they were unable to draw any firm conclusions, except to say that the hypothesis was not disproved. The problem is that there are large uncertainties in obtaining reasonable values, experimentally or theoretically, for segregation energies and there is no good experimental measure of embrittlement sensitivity. The other major flaw in the approach, is that the newly created fracture surfaces are assumed to be at thermodynamic equilibrium and that the fracture process is reversible. Neither of these assumptions reflects the actual process. It is unlikely that an understanding of the thermodynamics of segregation will lead to a real understanding of why GBE occurs.

Another popular approach to understanding GBE has been to consider the fracture process at the atomic level. That is, through understanding how segregating elements change the chemical bonds at the grain boundary, we will approach a better

understanding of the embrittlement problem. The first model to describe GBE in terms of weakened atomic bonds at the grain boundary was by Losch (1979) and described the effect of S in Ni. S, like most embrittling elements has a partially filled p shell and p electrons tend to form localized, directional covalent bonds. It was suggested that the S at the grain boundary forms strong hybridized bonds involving S 3p electrons and Ni 4s electrons. There are now less Ni 4s electrons to participate in the Ni-Ni metallic bonds that are usually formed by the Ni 3d and 4s electrons. An important consequence of this model is that the fracture does not occur by breaking metal-impurity bonds, but rather by breaking the weakened metal-metal bonds. Molecular dynamics studies (Ishida and Mori (1985), Peng et al. (1992)) have demonstrated that on application of a stress, a grain boundary will fracture between the metal-metal bonds rather than the metal-impurity bonds.

A similar model was suggested by Messmer and Briant (1982), which was drawn from the results of cluster quantum-mechanical calculations using a self-consistent field (SCF) real-space method, the SCF-X$\alpha$ approach. It was noted that the embrittling impurities are more electronegative than the host metal atoms, and will therefore draw charge away from the host metal atoms. A strong heteropolar (i.e. ionic) bond is formed between the impurity and nearest metal atoms, and therefore less charge is available to participate in the metal-metal bonds. Cohesive enhancers, such as C or B, on the other hand, were observed to form homopolar bonds, and did not draw charge from the metal atoms.

A number of similar investigations have since been performed in order to further elucidate the mechanism of GBE. Initial calculations by Krasko and Olsen (1990) using linear muffin-tin orbitals (LMTO) band structure calculations, found that there was a charge transfer from P atoms to Fe atoms, exactly opposite to that observed by Messmer

and Briant (1982). However, after further work (Wu and Freeman (1994)) they concluded that P induced rehybridization of the bonds at the grain boundary resulted in weakened Fe-Fe bonds. The inconsistencies in charge transfer direction were thought to be a consequence of ambiguities in the definition of charge transfer. When the case of B in Fe was examined (Wu et al. (1994)) it was seen that the B had an even larger effect on the Fe-Fe bonding, and it was concluded that a reduction in Fe-Fe bonding was not responsible for embrittlement. The approach taken by Wu and Freeman (1994) was interesting in that they were able to link quantum-mechanical calculations at the atomic level with the thermodynamic approach as represented by equation (2.11). Wu and Freeman (1994) compared the total energies obtained from the calculations for grain boundaries and free surfaces, with and without segregants, to come up for values for $\Delta g_s$ and $\Delta g_b$. This study also showed that impurity induced reconstruction of the grain boundary is very important in determining segregation energies.

Studies on the Fe-P and Fe-B system have also been made by Hashimoto et al. (1984), with the LMTO method, and in this case a distinctly different behavior was observed for P segregation, as opposed to B segregation. Both P and B produced bonding orbitals within a cluster at the boundary, but P weakened the bonding between the cluster and the surrounding matrix and B did not. Another set of calculations using the SCF $X\alpha$ approach confirmed these conclusions (Mori and Ishida (1986)).

Eberhart et al. (1984) claimed that a reduction in cohesive strength across the grain boundary is not sufficient to explain embrittlement; there must also be an increase in shear strength. According to their calculations, at some critical impurity concentration the impurity-impurity reactions become important. Eberhart et al. (1984) studied the Ni-S system and suggested that a network of strong S-S bonds in the grain boundary works with the weakened Ni-Ni bonds to produce GBE.

It can be seen that the various quantum-mechanical calculations have failed to come to a consensus about how bonding is changed as a consequence of segregation. The different types of behavior observed may simply be a consequence of the different structures and calculation methods chosen by different research groups. There is a clear need for experimental evidence describing changes in bonding at grain boundaries. Despite the differences of interpretation of the impurity-metal interaction, the proposed mechanisms for embrittlement and the quantum-mechanical calculations reviewed above, all suggest that a reduction of electrons available to participate in metal-metal bonds adjacent to the grain boundary is an important factor in GBE.

## 2.4 Experimental Techniques

Early techniques used to examine the chemistry of grain boundaries were indirect and were generally unable to identify segregants without some a priori knowledge. Quantification of segregation levels was most reliably performed through the indirect technique of measuring grain boundary energies and then using the Gibbs adsorption isotherm to determine a grain boundary coverage, $\Gamma$,

$$\Gamma = -\frac{1}{RT}\frac{d\gamma_b}{d\ln X_c}\bigg|_T \qquad (2.12)$$

The development of AES in the early 1970's allowed for the direct identification and quantification of the segregating species. It has since been the most extensively used technique to study segregation. In AES, a beam of electrons with an energy of 1-3 keV is directed at the surface of the material to be studied. The atoms in the material are ionized through the loss of a core electron and relax through the emission of Auger electrons (or X-rays). The Auger electrons have a characteristic energy depending on the atomic number and are collected and measured so that the elements present can be

identified. The Auger electrons are only emitted from a few atom layers below the surface and hence AES is a surface-sensitive technique. AES has a very high spatial resolution, a few atomic layers, perpendicular to the surface (or fractured boundary) and can be as low as 10-20 nm in lateral resolution (Hofmann (1990)). The Auger electron spectrum contains some information about the bonding state of the atoms, but this aspect of the spectrum has found limited application to date.

Another surface-sensitive technique with high depth resolution that has been used in segregation studies is secondary ion mass spectrometry (SIMS). A focused ion beam is used to sputter atoms from the surface and those that have been ionized are collected and identified. The lateral resolution is on the order of 1 μm or less, but the sensitivity is very high, therefore it is possible, as long as bulk concentrations are in range of a few ppm, to detect segregation in boundaries that are oriented perpendicular to the surface of the material (Hofmann (1990)). The main limitation of SIMS is that quantification is very unreliable. SIMS is however, one of the few experimental techniques that can identify hydrogen.

In x-ray photoelectron spectroscopy (XPS), otherwise called electron spectroscopy for chemical analysis (ESCA), a monochromatic beam of x-rays is directed at a material surface and the energy of the ejected photoelectrons is measured. The energy of the ejected electrons is related to the energy of the core electron states of atoms in the surface atomic layers. Although XPS could be used for elemental identification, it has primarily been used to provide information about the valence state of the surface atoms. The energy of the core electron levels shift upon valence changes and the energy resolution of XPS is sufficient to measure these chemical shifts (Turner (1993)). With XPS, the chemical state of the atoms at the grain boundary can, in principle, be probed. Hintz et al. (1983) observed a chemical shift in the S 2p line, relative to elemental S, for

grain boundaries in embrittled Ni. The chemical shift indicated an increase in the electron density in the vicinity of the S atom and, therefore, is consistent with the embrittlement mechanism of Messmer and Briant (1982). However, no corresponding change was observed for the Ni line and the explanation for this was that the Ni signal results primarily from Ni below the surface atoms not bonded with S. The role of H must also be considered, because if H were present it may be expected to bond with the S at the grain boundary, causing the observed chemical shift. In contrast to the results on Ni-S, Hallam and Wild (1995) observed, using XPS, that P at grain boundaries in Fe-Ni alloys is in the elemental state.

The three techniques described above are all surface techniques and to study grain boundary segregation it is necessary to fracture the material intergranularly. This is a disadvantage if one wishes to study differences between strongly and weakly embrittled boundaries or alternatively some other grain boundary phenomenon. It may also lead to erroneous results for segregation levels. The fracture path will most likely follow the most embrittled grain boundaries, which will be those containing the most amounts of segregants. Grain boundaries that contain little or no segregation will not be probed. The fracture path will also become important in determining the measured segregation levels for a given boundary. For example if the fracture path deviates even slightly from the exact grain boundary plane, then lower segregation levels will be recorded. The mechanisms for GBE, as described earlier, suggested that fracture occurs through the breaking of the metal-metal bonds. It is generally assumed that the segregant is equally divided between the two fracture surfaces, but it is conceivable that the fracture path may follow just beside the grain boundary plane, in which case one fracture surface will have a greater concentration of segregant. A number of experiments have found that the segregant is equally distributed between the fracture surfaces (Powell and Mykura

(1973), Briant (1983)), however in a couple of cases the segregant has been found to be distributed unequally between the fracture surfaces (Menyhard and McMahon (1991), Menyhard et al. (1991)). Given these considerations, it would be preferable to use an experimental technique that does not require the specimen to be fractured.

In field ion microscopy (FIM), a very strong field is applied to a specimen which is in the shape of a fine tip and the surface atoms are removed and analyzed. It has been used to study the structure of internal interfaces with high spatial resolution. When combined with time of flight mass spectrometry it is called the atom probe (or APFIM) and can provide chemical information with atomic level resolution. For example, Krakauer and Seidman (1994) used APFIM to obtain quantitative segregation levels for an Fe(Si) alloy as a function of grain boundary crystallography. However, FIM has found limited application due to instrumental complexity and difficulty in preparing suitable specimens.

There are a number of experimental techniques based on electron microscopy. High resolution electron microscopy (HREM) has been used extensively to study the internal atomic structure of grain boundaries. The limitation of HREM in segregation studies is that it is not chemically sensitive. The only way in which a segregant can be "seen" in HREM is through the effect it has on the grain boundary structure. Interpretation of HREM images is almost always ambiguous and, in general, image simulations should be performed in order to properly understand the structure. In other words, one needs to hypothesize what the structure is to be able to interpret the results of HREM. Such an approach was taken by Luzzi et al. (1991) to describe Bi at $\Sigma$=3 grain boundaries in Cu. An ordered intergranular phase of Bi was suggested, and image simulations gave good agreement with experimental HRTEM images. Some structural information from grain

boundaries can be obtained through x-ray or electron diffraction, but these are not routinely used for interfaces, and certainly not for segregated interfaces.

The relatively recent technique of Z-contrast imaging, like HREM can provide atomic structure information, but unlike HREM it is chemically sensitive and the images are relatively straightforward to interpret. A very nice application of this has been observed in the segregation of Bi to a $\Sigma$=5 grain boundary in Cu (M. F. Chisolm, private communication). The Bi atoms were clearly observed at the grain boundary and the segregation sites correlated with a simulated grain boundary structure. At this stage atomic resolution Z-contrast imaging is still a specialized technique with only a few laboratories working in the area. The disadvantage of both HREM and Z-contrast imaging is that there must be a common low index direction, in both grains on either side of the boundary, and the boundary plane must also be parallel to this direction. Therefore, only a small, special subset of all grain boundaries can be examined.

## 2.5 Analytical Electron Microscopy

In addition to structural information, electron microscopy can provide chemical information and in a scanning transmission electron microscope (STEM), this information can be obtained with a spatial resolution that can be < 1 nm. A simplified schematic of the processes occurring in the STEM is shown in Figure 2.2. Reviews of the optics of image formation and diffraction in the STEM can be found in Crewe (1973), Brown (1981) and Batson (1988) and many microscopy texts. An extremely brief introduction will be given here.

A small, high-energy (100-300 keV), electron probe is focused on a thin specimen (normally < 200 nm) and the electrons in the probe interact with the specimen in a number of ways. To form an image of the specimen the probe is scanned over the

specimen and a detector collects the transmitted electrons that have been scattered less than a given collection angle to form a bright-field (BF) image.

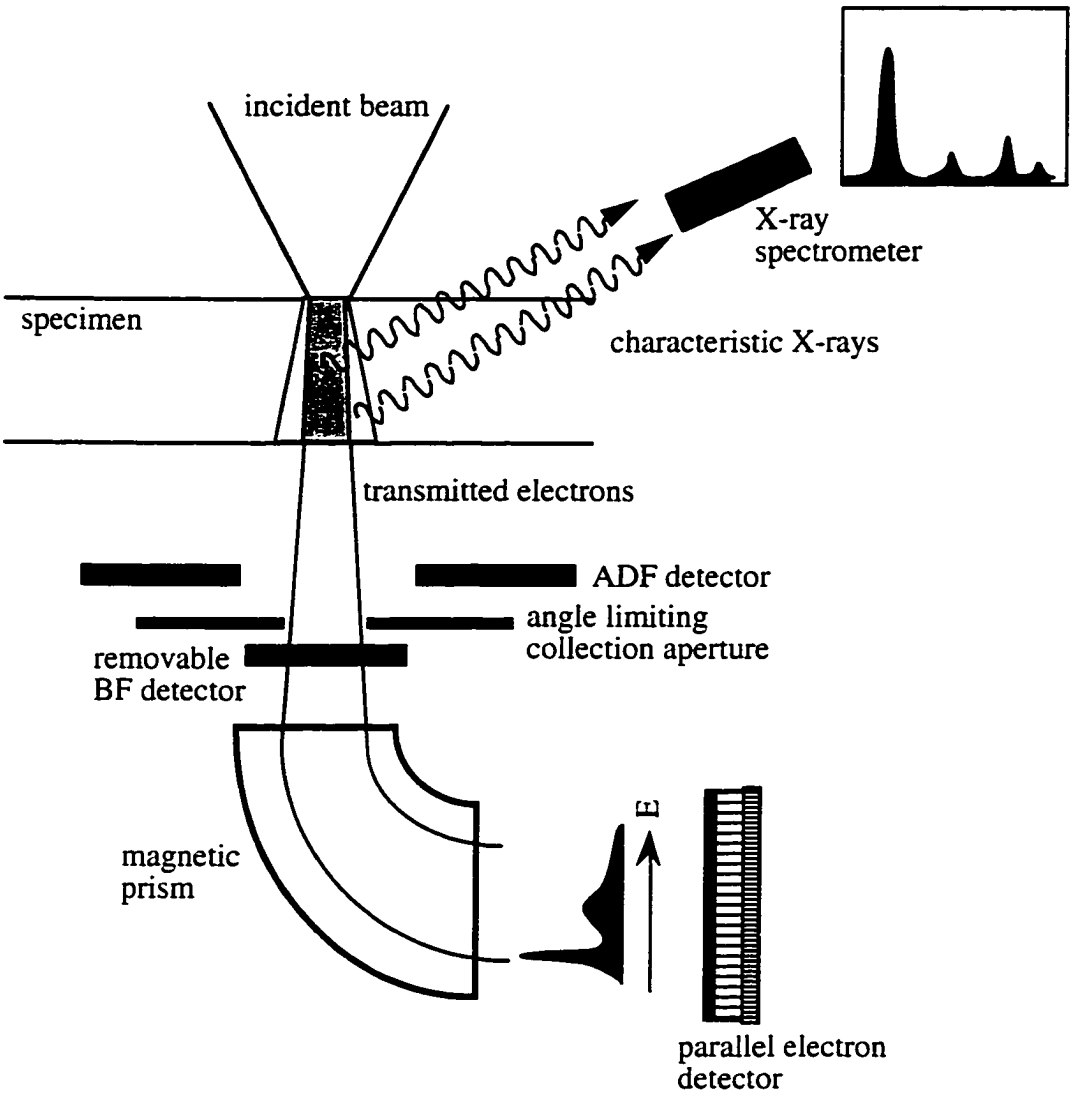


Figure 2.2 Schematic of a STEM

When the collection angle is relatively small then the images in the STEM, through reciprocity, can be interpreted in same way as BF images in the TEM. However, the images are collected serially, rather than in parallel as done in the TEM and, and for similar recording times. the quality of the images is worse. This poor collection efficiency can be overcome to some extent by the other common imaging mode in the

STEM. A detector which collects electrons scattered with angles between some minimum and maximum values (usually 10 mrad - 100 mrad) is used to form an annular-dark field (ADF) image. Diffraction information is also available in the STEM either by rocking-beam methods, which are analogous to selected-area diffraction patterns in the TEM, or through the use of a CCD camera beyond the specimen, an approach commonly called microdiffraction.

The advantage of STEM over TEM is generally not considered to be through the imaging capabilities, but rather because of the analytical information obtainable when the small electron probe is placed on a feature of interest in the specimen, such as a grain boundary. As in AES, some of the atoms in the specimen are ionized by the electrons in the probe. However, in the STEM it is usually the X-rays that are emitted during relaxation that are analyzed to provide information about the elemental species present. The X-rays are emitted isotropically but only those within a small solid angle are collected by an X-ray spectrometer, nearly always of the energy-dispersive (XEDS) type. Characteristic peaks, whose energy depends on the elemental species present, are produced in the X-ray spectrum and quantification to produce compositional ratios is relatively straightforward (Cliff and Lorimer (1975)).

The first demonstration of the applicability of XEDS in the STEM to detecting equilibrium segregation was by Doig and Flewitt (1977). This and other early experiments on first generation TEM/STEM systems, for example Ti in steel (Faulkner and Hopkins (1977)) and Bi in Cu (Baumann and Williams (1981)), had fairly poor spatial resolution, 50 nm or greater. However, the development of dedicated STEMs with field emission guns (FEG), increased both the spatial resolution and sensitivity of the technique and hence it found more extensive application (see for example Vander Sande et al. (1984), Vatter and Titchmarsh (1989), Williams and Romig (1989)). For

systems which are not intrinsically brittle, such as Cu segregation in Al, it has been particularly useful (Small et al. (1994)). The details of spatial resolution, detectability and quantification for XEDS in the STEM will be discussed in more detail in Chapter 3.

The other main analytical approach in the STEM, electron energy-loss spectroscopy (EELS), is based on measuring the energy of the electrons that are transmitted through the specimen. This is normally done by passing the electrons through a magnetic prism in order to disperse the electrons in energy. A parallel recording system consisting of a scintillator coupled to a photodiode array is used to collect an energy spectrum (Krivanek et al. (1987)). A schematic of a typical energy loss spectrum is shown in Figure 2.3 (from Brydson (1991)).

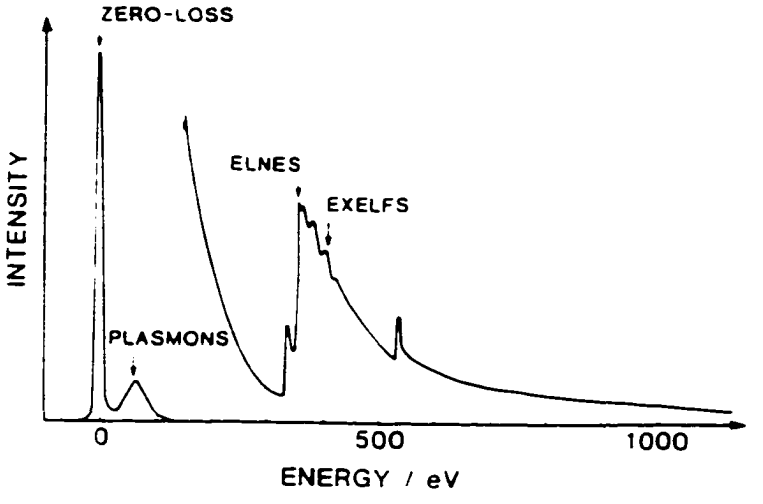


Figure 2.3 Schematic of the electron energy loss spectrum (from Brydson (1991) )

Except in very thick specimens, most of the electrons pass through the specimen without losing any energy and contribute to the zero-loss peak (ZLP). The next most intense peak in the spectrum is the plasmon peak which arises from losses by collective excitation of the valence electrons (Egerton (1996)). The energy of the plasmon peak is related to the electron density in the material but the most common use of the plasmon peak is for thickness determination. There are also low-energy-loss features that are due

to excitation of a single electron out of the valence band, but the interpretation of these is, with a few exceptions, difficult and has found limited application.

The features in the spectrum that have found the largest application are the ionization edges which arise from the excitation of the core electrons into the unoccupied free-electron-like states above the Fermi level, $E_F$. The ionization edge is superimposed on an exponentially decreasing background which is normally removed before analysis. The edges have a characteristic energy of onset which can be used to identify the elements present and the areas under the edges can be used for quantification (Egerton (1996)). Although in principle, EELS has a higher detection sensitivity than XEDS, particularly for light elements (Leapman and Hunt (1991)), it has not found as extensive application to segregation studies. One of the few examples being the observation of the segregation of B, which is difficult to detect with XEDS, to grain boundaries in $Ni_3Al$ (Muller et al. (1996)).

There are a few different approaches to obtaining information about grain boundary composition by using a small electron probe and these are illustrated schematically in Figure 2.4.

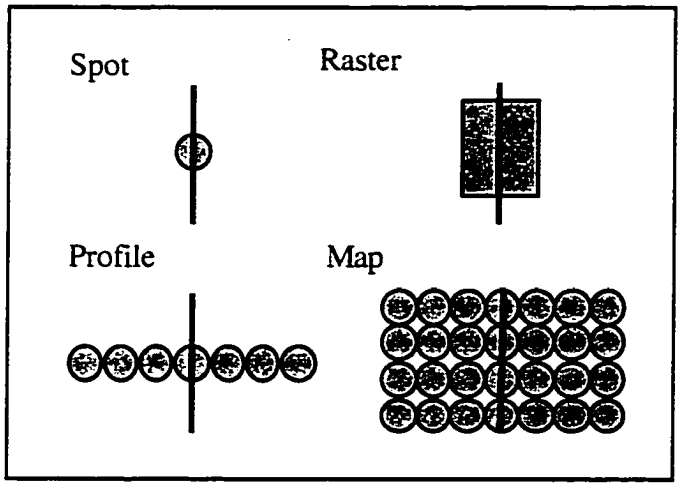


Figure 2.4 Different modes of obtaining grain boundary composition in AEM

The first approach, and that taken by Doig and Flewitt (1977), is to simply place the small electron probe on the specimen and measure the resultant X-ray spectrum or energy-loss spectrum. This approach is most appropriate for a rapid survey of the elements at the grain boundary, and should always be compared to a spectrum taken from within a grain. Spot mode will give the maximum sensitivity for a given total acquisition time, however, quantification is relatively inaccurate as the probe size and beam broadening are not usually well known. To improve accuracy of quantification, at the expense of detectability, the probe can be rastered over a fixed area (usually ~10-20 nm square) while the appropriate signal is collected. In this way, the "probe size" becomes well defined and beam broadening has a smaller contribution. Recent experiments and modeling have shown that even in the raster approach, if accurate quantification is desired, beam broadening should not be neglected (Alber et al. (1997)).

Another common approach to measuring segregants (Hall et al. (1981), Vander Sande et al. (1984), Titchmarsh (1986), Small et al. (1994), Muller et al. (1996)) is to step the incident beam along a line perpendicular to the grain boundary. The XEDS or EELS spectra collected at each point are then individually quantified to obtain a profile of segregant across the grain boundary. For equilibrium segregation, the width of this profile is primarily determined by the size of the electron probe. The level of segregation can be determined by integrating under the profile (Titchmarsh (1988)). Recent advances using multivariate statistical analysis to analyze a series of X-ray spectra taken from a profile across a grain boundary show promise, especially for the case when there are a number of different segregating species (Titchmarsh and Dumbill (1996,1997)).

The final approach, that of obtaining a two dimensional map of segregating species has found little application until recently. The main limitation arises because, to ensure collection times are not unacceptably long, given limitations in the mechanical stability

of the microscope stage and emission decay of the FEG, the collection time at each pixel point must be extremely short, on the order of 200 μs compared to 10-100 s for a typical single spectrum, and hence, very little signal is acquired. Recent advances in microscope design on the VG 603 at Lehigh University have allowed the collection of X-ray maps on a routine basis (Williams et al. (1997)). When X-ray mapping, pre-defined windows are used to select which peaks in the spectrum will contribute to the map, and a number of these elemental maps can be collected simultaneously. In principle, the full spectrum at each point can be stored and such an approach was suggested for EELS by Jeanguillaume and Colliex (1989) and called "spectrum imaging". EELS spectrum imaging has found some application to date (Hunt and Williams (1991), Colliex et al. (1994)), but segregation to grain boundaries using EELS spectrum imaging has not yet been observed. Mapping is the most preferable approach because the same data available from spot, raster and profile experiments can be extracted from the 2-D map but, *in addition* , a 2-D map contains information about the distribution of the segregant at different regions of the grain boundary. The main limitation of the mapping approach is poor statistics due to the very short dwell times.

There is one final approach to obtaining a 2D compositional map that does not rely on a STEM. An energy selecting filter is attached to a conventional TEM, and an image is formed using only electrons that have lost energy within a particular energy window (see Reimer (1995) for a discussion of energy filtered imaging). This is a parallel approach and therefore acquisition times are orders of magnitude smaller than those required for mapping in the STEM, but full spectral information is not available. There have been some examples of segregation studied with energy filtering (Bentley (1997), Menon et al. (1997)), however, these examples were on non-equilibrium segregation

phenomena and it remains to be seen whether the spatial resolution and sensitivity of energy filtered imaging is sufficient to observe equilibrium segregation.

## 2.6 Measurements of Electronic Structure

Analytical electron microscopy, as described above, can provide information about the identity, quantity and distribution of segregants at a grain boundary. However, it is unable to explain how the segregant changes the material properties. Knowledge of how the electronic structure, and hence bonding, at the grain boundary changes upon segregation will aid in answering this question.

There are a number of techniques that can provide information about electronic structure. As described previously, XPS can be used to find the valence state of the segregated atoms, but not a full description of the electronic structure. When an ultraviolet (UPS) or synchrotron source is used instead, the occupied valence states at the surface can also be probed with photoemission. To date, no studies of electronic structure have been performed on grain boundaries using these techniques. There are a few techniques that can provide information about the unoccupied electronic states such as inverse photoemission spectroscopy (IPS), bremmstrahlung isochromat spectroscopy (BIS) and X-ray absorption spectroscopy (XAS). None of these techniques has a spatial resolution sufficient to analyze changes in electronic structure at the grain boundary.

There is information in the electron energy loss spectrum about electronic structure and it is one of the few techniques that can observe changes in bonding at a grain boundary. Superimposed on the basic shape of the ionization edge are additional oscillations in the intensity. Oscillations at an energy > ~50 eV above the edge onset are called the extended energy loss fine structure (EXELFS) and can be used to find interatomic distances and coordination numbers. The oscillations within ~50eV of the edge onset are

called the electron energy loss near edge structure (ELNES) and are related to the local density of unoccupied electronic states. The unoccupied density of states (DOS) reflects the environment and bonding and hence the ELNES can be used to give information about interatomic bonding. The relationship between ELNES and the local DOS will be discussed more thoroughly in Section 3.2.

A few experiments have recently been performed, examining the changes in the ELNES at grain boundaries, in order to further elucidate the mechanism for grain boundary embrittlement. Earlier work on Bi-doped Cu observed an extra intensity in the Cu edge, just above the edge threshold, at grain boundaries containing Bi (Keast (1996), Keast et al. (1998)). Calculations of the electronic structure, using a $\Sigma$=3 grain boundary structure containing Bi proposed by Luzzi (1991), Luzzi et al. (1991), also showed a peak in the unoccupied DOS above the Fermi energy due to Bi. However this peak was at a different energy than the experimentally observed peak. It was thought that the discrepancy between the experimental and calculated results could be due to the different atomic structures examined. It would be desirable to perform experimental ELNES investigations on a grain boundary with the structure proposed by Luzzi (1991), Luzzi et al. (1991).

The observation on Bi-doped Cu are consistent with observations of Muller et al. (1996) on the intrinsically brittle $Ni_3Al$, where extra intensity in the Ni edge, in the peaks commonly called white lines, was observed at the grain boundaries. Upon doping with ductilizing B, this white-line intensity returns to the bulk value. That is, in both of these systems there is an increase of white-line intensity associated with brittle boundaries. In contrast, experiments on Fe - 0.4 wt% P saw a decrease in white-line intensity at the boundary (Ozkaya et al. (1995)). Interestingly, calculations of the expected change in

electronic structure at P doped boundaries also predicted a decrease in white-line intensity (Alvarez and Rez (1997)).

The experiments performed to date are promising, in that they demonstrate that the ELNES can probe bonding changes at grain boundaries, the understanding of how bonding at grain boundaries may be altered by a segregating impurity is far from complete.

## 2.7 Summary

The embrittlement of metals through the segregation of impurities to the grain boundaries is an important phenomenon that is not yet completely understood. The AEM has the capacity to identify and quantify these segregants, with a similar spatial resolution and sensitivity to other experimental techniques. It also has the advantage that the material does not need to be fractured, which allows for the examination of non-brittle grain boundaries. In this work, high resolution X-ray microanalysis will be performed on a number of systems, and the applicability of 2D X-ray mapping to segregation studies will be demonstrated. Further microanalysis will be performed on the previously studied Cu-Bi system, in particular a thorough examination of $\Sigma$=3 grain boundaries, as this boundary structure was that chosen for electronic structure calculations. Other systems to be studied include another classic embrittling system of S doped Ni, as well as Ag and Sb segregation in Cu. The segregation of Ag in Cu has only ever been observed using indirect techniques because it does not make the boundaries brittle and hence surface techniques cannot be used.

In addition to compositional information, changes in the electronic structure and, therefore, bonding can be examined using the ELNES. Earlier investigations have indicated that it is possible to observe such changes, and the approach will be extended

here. The effect of S on electronic structure in Ni will be examined. Similarly grain boundaries in Cu containing either Ag or Sb will be examined. Ag and Sb have similar atomic sizes, and yet different electron configurations. Sb, like Bi, embrittles Cu whereas Ag does not. Through these investigations a better understanding of how segregants alter the bonding at the grain boundary will be obtained and interpreted with reference to the segregation mechanisms described in Section 2.3.

An in-depth discussion of resolution and detectability in AEM, particularly as applied to segregation problems will be given in Chapter 3. A discussion of the relationship between the ELNES and the unoccupied DOS will also be given in Chapter 3. Chapter 4 will describe the experimental procedures used to obtain compositional and bonding information at grain boundaries and Chapter 5 contains the results from these studies. A discussion of the segregation studies and an interpretation of the ELNES results will be given in Chapter 6 and the conclusions from these studies in Chapter 7. Some suggestions for future work are made in Chapter 8.

# 3. ASPECTS OF EXPERIMENTAL TECHNIQUES

## 3.1 Resolution and Detectability in AEM

When the small electron probe of the STEM is placed on the specimen there is a volume of interaction between the electrons in the probe and the atoms in the specimen. There are two factors that contribute to this interaction volume. The first is the size of the incident electron probe and the second relates to how that incident probe is broadened as it passes through the specimen and interacts elastically with it. When using EELS, beam broadening is less important because, as can be seen by reference to Figure 2.2, the collection aperture of the spectrometer cuts off electrons that have scattered through large angles. For EELS, the interaction volume is therefore determined by the probe size and the collection angle of the spectrometer. Titchmarsh (1989) shows an example of the superior spatial resolution for EELS, relative to XEDS in thick samples.

The size and shape of the interaction volume and the electron distribution within it is important for a number of reasons. Firstly, the spatial resolution in AEM is determined by the size of the interaction volume. For example, one definition of spatial resolution is the diameter of the volume that contains 90% of the generated signal (Michael and Williams (1987)). Secondly, when the features of interest are smaller than the size of the interaction volume, then the compositional quantification for these small features will depend on the assumptions chosen for the interaction volume. Detectability limits can also be a function of both the interaction volume and incident probe current. The measured compositional distribution, either through mapping or profiling, will always be a convolution of the actual compositional distribution and the electron distribution. In the case of equilibrium grain boundary segregation, the segregation width is nearly

always narrower than the size of the interaction volume and therefore an understanding of the incident probe characteristics and the nature of beam broadening is crucial.

Very small incident probe sizes are obtainable in the STEM, down to the 2 Å level so, in principle, it should be possible to obtain analytical information with a spatial resolution approaching this dimension. However, this theoretical optimum is rarely achieved in practice: notable exceptions being the atomic resolution EELS of Browning and Pennycook (1995) on a $CoSi_2$/Si (111) interface and Batson (1993) on a Si/$SiO_2$ interface. Practical limitations occur because resolution and detectability are inextricably interlinked. As the probe size is reduced, the current in that probe is also reduced along with the generated signal. Similarly, as the specimen thickness is reduced in order to reduce beam broadening, less signal is generated and detectability will fall. For XEDS the best spatial resolution obtained to date is on the order of 2 nm (Grovenor et al. (1984), Michael et al. (1988), Long and Glaisher (1990)). One reason for the poorer resolution than EELS arises from the beam broadening contribution. Secondly, larger initial probe sizes, containing more current, are often used in order to compensate for the lower collection efficiency of XEDS.

### *3.1.1 Probe Size*

The relationship between the probe size and beam current arises from the brightness equation

$$\beta = \frac{4i}{(\pi\alpha d)^2} \qquad (3.1)$$

where the brightness $\beta$ is fixed throughout the electron microscope column. The brightness equation can be applied at the electron source in which case $\alpha$ refers to the divergence angle from the source, d refers to the size of the source and $i$ the current

emitted from the source. The pre-specimen optics of the STEM (consisting of the condenser and objective lenses and various apertures) produce a small, demagnified image of this source onto the specimen, in which case, the convergence angle $\alpha$, the beam current $i_b$ and the size of the demagnified probe, $d_g$ (often called the Gaussian probe size), will be related through equation 3.1. The advantage of using a high-brightness source, such as an FEG becomes immediately obvious from equation 3.1. That is, for a given probe size, or spatial resolution, a probe formed by a high-brightness gun will have a higher beam current and similarly, for a given beam current, a smaller probe can be formed.

There are a number of other contributions to the final probe size which are often, but arbitrarily, added in quadrature (Titchmarsh (1986), Michael and Williams (1987))

$$d = \left(d_g^2 + d_s^2 + d_d^2\right)^{1/2} \tag{3.2}$$

From equation 3.1, the demagnified source size, $d_g$, is given by

$$d_g = \frac{2}{\pi}\left(\frac{i_b}{\beta}\right)^{1/2}\alpha^{-1} \tag{3.3}$$

The objective lens introduces spherical aberration and the size of the disc of minimum confusion is given by

$$d_s = 0.5 C_s \alpha^3 \tag{3.4}$$

where $C_s$ is the spherical aberration coefficient of the lens.

The diffraction limit introduces another contribution

$$d_d = 1.22\lambda/\alpha \tag{3.5}$$

where $\lambda$ is the wavelength of the incident electrons and will be fixed by the accelerating voltage chosen. The objective lens also introduces chromatic aberration, but for most situations it is small enough to be neglected. Note that expressions 3.3-5 are all approximately consistent with the definition of a probe size measured at FWTM (full width at tenth maximum) which, assuming a 2-D Gaussian distribution, contains 90% of the electrons (Michael and Williams (1987)).

The choice of adding the various contributions to the probe size in quadrature has been the traditional approach, although it is not technically the correct approach. For example, equation 3.4 for the spherical aberration refers to the size of the disc of minimum confusion. The disc of minimum confusion actually lies in a different optical plane to the Gaussian image plane. A correct optimization will involve a full wave optical treatment, such as those performed by Crewe (1987) and Mory et al. (1987) and will determine not only an optimum convergence angle, but also an optimum defocus. The wave optical approaches predict optimum probe sizes smaller than those predicted by equation 3.2 and, in addition, do not usually include the effects of a finite source (equation 3.3). Addition in quadrature, although not fully correct has been found adequate for describing experimentally determined probe sizes (Titchmarsh (1986), Michael and Williams (1987)) and will be used here.

It follows from equations 3.1-5 that for the best spatial resolution we need high $\beta$, small $\lambda$ (i.e. large accelerating voltage) and small $C_s$. However, these are factors that are introduced during microscope design and, assuming the microscope is operated at its maximum accelerating voltage, are not under the control of the user. To produce the optimum probe size for a given microscope will involve an appropriate choice of the convergence angle, $\alpha$, and probe current, $i_b$. The (arguably) most sensible approach is to define what level of current is needed in the probe in order to detect a statistically

significant signal. Note that this minimum level will depend on the analytical technique chosen. In XEDS, it is sometimes considered that 1 nA of beam current is a reasonable level, however, if the collection efficiency is enhanced, a lower current may be acceptable. As stated previously, the collection efficiency for EELS is higher than XEDS and, therefore, in some cases it may be possible to operate with a lower beam current and hence better spatial resolution. In Z-contrast imaging, the requirements on beam current are not very stringent (typical beam currents being in the order of 0.01 nA), and therefore very small probe sizes can be used and atomic resolution imaging is possible.

The way that the STEM is operated is usually different depending on whether XEDS, EELS or imaging is being used. For normal operation of a STEM, there is a probe-defining aperture, called the real objective aperture (ROA), that defines the convergence angle onto the specimen. This aperture can be a source for stray x-rays, and therefore for XEDS, an aperture, called a virtual objective aperture (VOA), in a conjugate plane to the ROA but further away from the specimen is used. In this configuration the hole count, i.e. x-rays generated when the electron beam is not on the sample, is essentially zero. The optics of the two configurations, in terms of the role of the condenser lenses in optimization of the probe, as shown in Figure 3.1, are quite different. The size of the VOA aperture defines the beam current and the condenser lenses are then used to change the convergence angle and hence the probe size. The size of the ROA, on the other hand, defines the convergence angle onto the specimen and the condenser lenses are then be used to change the current in the probe. Optimization of the probe when using a VOA is relatively straightforward. The size of the VOA is chosen so that the probe will contain sufficient current to produce the required statistics in the X-ray spectrum. The condenser lenses are then used to set the convergence angle that gives the optimum

probe size for this beam current. Figure 3.2. shows the contributions to the probe size as a function of convergence angle for the 30 μm VOA and the 50 μm VOA in the VG 603 STEM at Lehigh University.

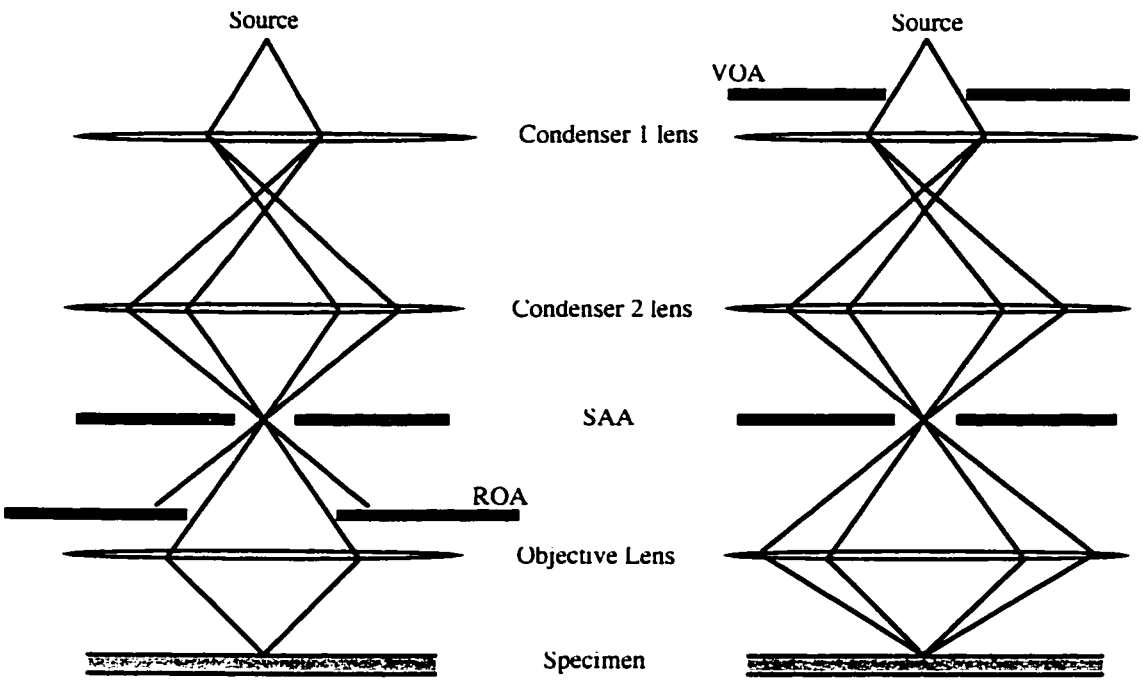


Figure 3.1 Comparison of pre-specimen optics in the STEM for the case of a ROA and a VOA. The ROA defines the convergence angle and the condenser lenses are used to vary the beam current. The VOA defines the beam current and the condenser lenses vary the convergence angle.

For a probe with a beam current of 0.6 nA, the theoretical optimum probe size of 1.4 nm (FWTM) occurs at a convergence angle of 7 mrad. The experimentally measured probe size is ~ 1.4 nm (FWTM) at a convergence angle of 6 mrad and the theoretical trends of convergence angle with probe size have been reproduced. It so happens, that for this microscope, the optimum convergence angle can obtained using only the second condenser lens. Appendix A contains details on the experimental measurements of probe size and how they compare to theoretical estimates. An important fact to note from Figure 3.2 is that the optimum convergence angle (and condenser lens settings), are different depending on the size of the VOA. Therefore, optimization of the condenser

lenses will depend on the size of the VOA chosen, if the smallest probe size for a given beam current is desired.

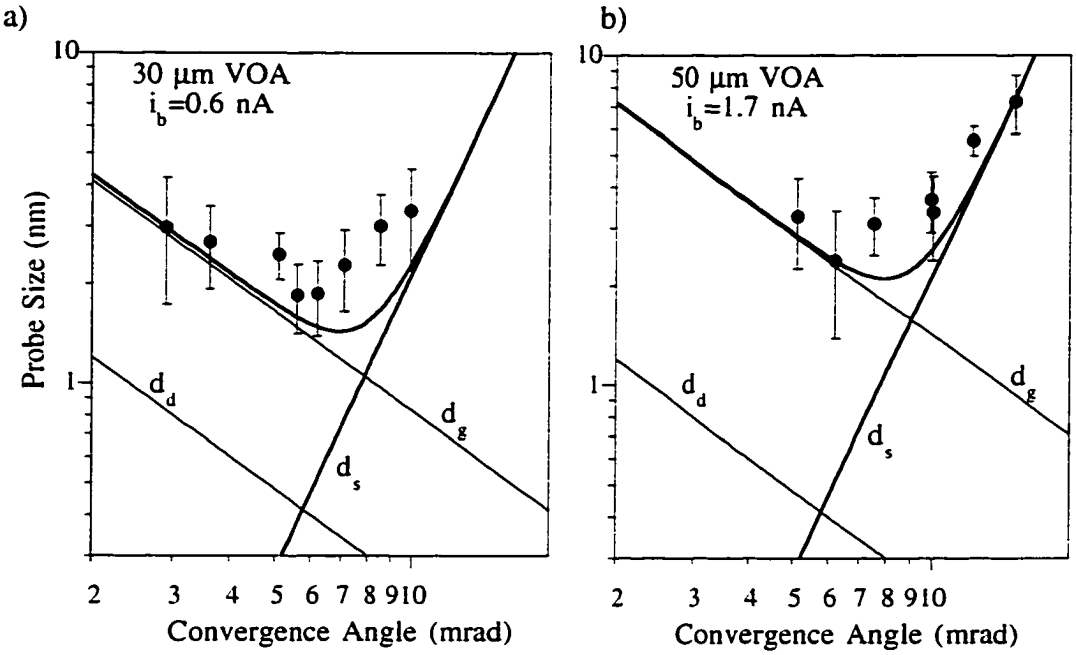


Figure 3.2 Experimental and theoretical probe sizes as a function of convergence angle, for a) the 30 µm VOA and b) the 50 µm VOA

The situation for the ROA is somewhat more complex. The convergence angle onto the specimen is fixed by the size of the ROA, and therefore the contributions of spherical aberration and the diffraction limit to the probe size are fixed by the choice of aperture. However, as the condenser lenses are changed, the current in the probe changes and thus the probe size will also change through the source demagnification term of equation 3.3. For the case when very small probes are required, conditions are chosen such that the $d_g$ term will be smaller than both $d_d$ and $d_s$ . This condition implies a very small beam current, and for the VG 603, it requires that $i_b$ <0.05 nA. Under this condition the optimum probe size will be obtained when

$$\frac{d\left(\sqrt{d_d^2 + d_s^2}\right)}{d\alpha} = 0 \qquad (3.6)$$

For the VG 603 this corresponds to a convergence angle of 5.0 mrad and would produce a minimum possible probe of 0.55 nm (FWTM). The 50 μm ROA with a convergence angle of 6.2 mrad is the closest to achieving this optimum.

The current necessary to ensure that $d_g$ is smaller than $d_d$ and $d_s$ is very much smaller than is typically used for microanalysis and, therefore, we usually have a significant contribution of the Gaussian probe size to the final probe size. Figure 3.3 shows how the beam current depends upon the setting of the first condenser lens for each of the four available ROA sizes in the VG 603. Figure 3.4 shows the calculated expected probe sizes for these beam currents with a few experimental measurements. In these figures the current in the 1st condenser lens is relatively high and there is a crossover between the 1st and 2nd condenser lenses. It also possible to obtain similar conditions but with a low 1st condenser lens current and no crossover.

The conclusion that can be drawn from Figure 3.4 is that when a beam current below ~1 nA is required, the 50 μm ROA will give the smallest probe sizes. If a beam current above 1 nA is required, then the aperture should be changed to the 70 μm ROA (and the condenser lenses adjusted) to give the optimum probe size. It should be noted that the curves in Figure 3.4 are very dependent on the value taken for the brightness. As discussed in Appendix A, the brightness has been measured to be $0.34 \times 10^{13}$ A/m$^2$/sr. If the nominal brightness value of $1 \times 10^{13}$ A/m$^2$/sr is used, then resultant plot of d vs. $i_b$ gives the 50 μm ROA as the optimum aperture regardless of the beam current. It is believed that the measured value for brightness is the most appropriate.

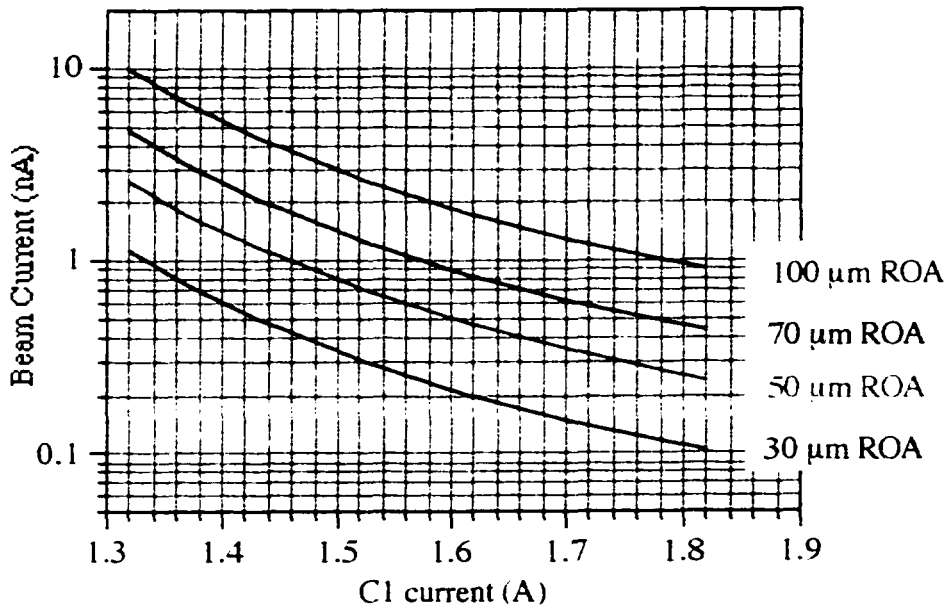


Figure 3.3 Probe current as a function of first condenser lens setting for each ROA.

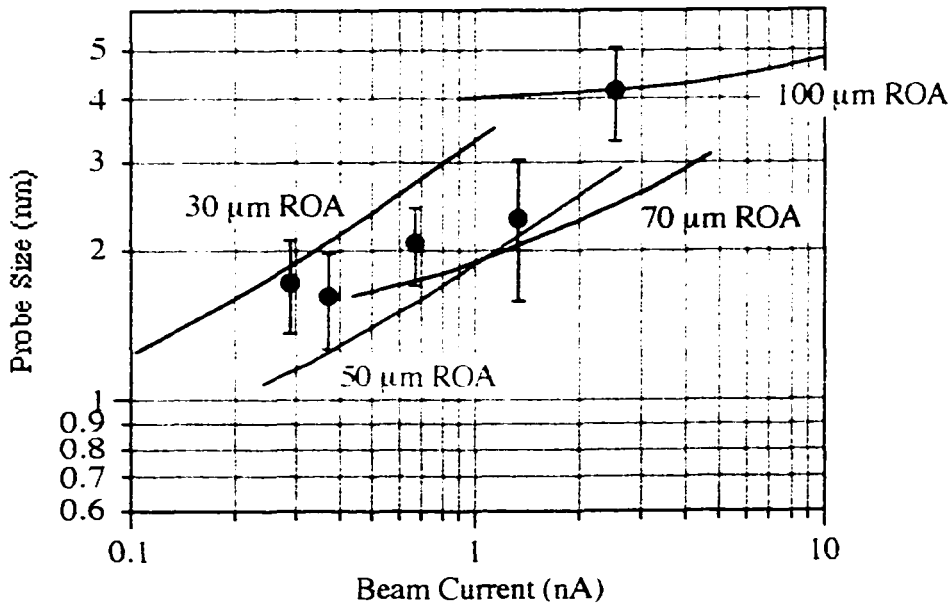


Figure 3.4 Probe size as a function of probe current for each ROA

### *3.1.2 Beam Broadening*

The preceding discussion provided a description of how the choice of microscope operating parameters governs probe size, for a given probe current. The beam broadening contribution to spatial resolution is less dependent on microscope operation, with the exception of accelerating voltage, and more a function of the specimen.

The first approach to describing the way the electron beam is broadened as it passes through the specimen was by Goldstein et al. (1977) where it was assumed that each incident electron suffered a single, large-angle Rutherford scattering event at the center of the foil. This gave rise to an expression for beam broadening, b, (in cm)

$$b = 6.25x10^5 \frac{Z}{E_0}\left(\frac{\rho}{A}\right)^{1/2} t^{3/2} \qquad (3.7)$$

where Z is the atomic number, $E_0$ is the incident beam energy (in eV), $\rho$ is the density ($g/cm^3$) and t is the thickness (in cm). Equation 3.7 is usually called the single-scattering approximation and describes the exit diameter from the foil that contains 90% of the scattered electrons.

This expression was modified by Reed (1982) where the assumption that scattering only occurred at the center of the foil was relaxed. The only effect was to change the coefficient in the equation to $7.21X10^5$. The assumption of a single-scattering event is actually unrealistic for the typical foil thicknesses used for microanalysis. Despite this, the single-scattering equation has been found to give reasonable agreement with experiment (Hutchings et al. (1979), Cliff and Lorimer (1981)). Cliff and Lorimer (1981) calculated an expression for beam broadening allowing for plural scattering and surprisingly found exactly the same expression as the single-scattering equation. There

are other, probably more correct, approaches to estimating the effects of beam broadening, such as the transport equation approach (Rez (1983)) and Monte-Carlo methods (Joy (1995)). However, the single-scattering equation provides a quick, rough estimate of the extent of beam broadening that can be expected under particular experimental conditions for a given material.

The other area of debate is the method by which initial probe size and beam broadening should be combined in order to come up with an estimate for the interaction volume and/or spatial resolution. The simplest model describes the interaction volume as a truncated cone with an upper diameter given by the probe size and the lower diameter given as the sum of the beam diameter and the beam broadening (see Figure 3.5) (Baumann and Williams (1981)).

The spatial resolution, R, was initially described as the diameter of this exit surface, that is, either $R = d+b$ or $R = (d^2+b^2)^{1/2}$. However, this will overestimate the measured resolution, because the signal is generated throughout the cone. An alternative description took R to be halfway through the diameter of the cone (Michael et al. (1990)). Another alternative would be to describe R as the diameter of the cylinder that contains the same fraction of the electrons (i.e. 90%) as the cone, in which case, $R = \sqrt{d + bd + b^2/3}$. Approaches such as this provide simple geometrical expressions to describe the interaction volume and can be used to describe spatial resolution or for more accurate quantification.

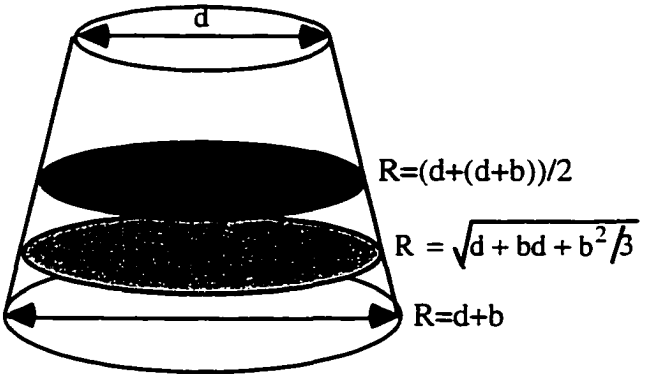


Figure 3.5 Truncated cone model of the interaction volume.

A full analysis would require a three dimensional description of both the compositional variations and the electron probe distribution. An analytic method was suggested by Doig et al. (1980) and Doig and Flewitt (1982) where it was assumed that the incident beam can be described as a Gaussian distribution, with a standard deviation $\sigma$, (note $d_{FWTM}=4.29\sigma$) and as the beam passes through the foil, the distribution is broadened but remains Gaussian and can be described by

$$I(x,y,t) = \frac{i_b}{\pi(2\sigma^2 + \beta t^3)} \exp\left(\frac{-(x^2+y^2)}{2\sigma^2 + \beta t^3}\right) \tag{3.8}$$

where

$$\beta = 500\left(\frac{4Z}{E_0}\right)^2\left(\frac{\rho}{A}\right) \tag{3.9}$$

If the electron probe, with intensity distribution I(x,y,t), is placed on the feature of interest, then the signal generated by that feature, I*, in a foil of thickness h is given by

$$I^* = K\int_{-\infty}^{\infty}\int_{-\infty}^{\infty}\int_{0}^{h} I(x,y,t)C(x,y,t)\,dx\,dy\,dt \tag{3.10}$$

where C(x,y,t) describes the compositional distribution and K is a constant relating the electron flux to the detected signal. For XEDS, K would describe the efficiency of X-ray generation, emission and detection. Even for the simplest compositional distributions, equation 3.10, with the expression for the electron distribution given by 3.8, usually cannot be evaluated analytically and must be solved numerically.

If an experimental distribution has been obtained by varying the probe position, for example, by measuring a grain boundary segregation profile, the measured distribution, I*(x,y), is given by a convolution of C(x,y,t) and I(x,y,t). That is

$$I^*(x,y) = K \int_{-\infty}^{\infty} \int_{-\infty}^{\infty} \int_{0}^{h} I(x',y',t) C(x-x',y-y',t) dx'\, dy'\, dt \qquad (3.11)$$

and once again this is usually only solvable by numerical methods. In principle, one could extract the actual compositional profile by deconvolution of the electron distribution from a measured profile. In practice this is rarely performed due to statistical limitations.

The other approach to solving such problems in a full three dimensional fashion is through the use of Monte-Carlo simulations (see Joy (1995) for a discussion of the application of Monte-Carlo techniques to problems in analytical electron microscopy). The analytical approach described above and the Monte-Carlo method have been shown to give similar estimates for spatial resolution (Doig et al. (1981)) and both approaches have been applied to equilibrium segregation problems. Doig and Flewitt (1982) applied their approach to predict segregation profiles and detectability criteria for a grain boundary segregant. Titchmarsh (1986) used the Monte-Carlo method to model a grain boundary segregation profile, which showed very good agreement with an experimental profile and quantification of grain boundary segregation was performed by scaling the

experimental profiles to the Monte-Carlo calculations. Further work (Vatter and Titchmarsh (1989)) extended the Monte-Carlo approach to different foil thicknesses, probe sizes and boundary tilts and found that the areas under the profiles were independent of these variables. The Monte-Carlo approach was also used to predict segregation profiles for the complex segregation distributions produced by radiation -induced segregation in steels (Titchmarsh and Dumbill (1996)). Comparisons of the theoretical predictions to experimental results have not been extensive or detailed, with the exception of Michael et al. (1990) who, using equations 3.8-11, modeled profiles across an interphase boundary and, in general, saw excellent agreement with the experimentally measured profiles. Most recently Alber et al. (1997) have used the analytical approach to include beam broadening into calculations of grain boundary composition for the case of a raster scan.

Unfortunately such examples that are already present in the literature cannot be directly applied to the experimental results obtained in this work. The calculations are dependent on the details of both the specimen and the electron probe. In particular, improvements in collection efficiency have allowed the use of smaller incident probes and the use of a 300 keV beam energy will substantially reduce beam broadening. New estimates of the interaction volume are required. This will enable the determination of spatial resolution, detectability limits, accurate quantification and a description of compositional profiles.

### *3.1.3 Quantification of a Grain Boundary Segregant*

There are a number of ways of describing the amount of segregant at a grain boundary, and one that is commonly used describes a concentration as either weight or atomic percent at the grain boundary. The disadvantage of such a description is that inherent in it is some assumption about the grain boundary width. This is usually arbitrary and

differs between different workers, particularly those using different experimental techniques. Sometimes the segregation levels are expressed in terms of a number of monolayers, but once again the definition of what constitutes a monolayer is both varying and arbitrary. The approach taken in this work will be to describe the segregation level in terms of a grain boundary coverage, $\Gamma$, expressed in atoms/nm$^2$. This approach assumes that all of the segregating atoms lie on a single 2D plane, and therefore removes the arbitrariness associated with a defined grain boundary width. This description will be physically unreasonable if more than one atomic plane is covered by segregant. Equilibrium segregation is usually on the order of 1 monolayer and so using $\Gamma$ should provide a reasonable description. To allow for comparison between different segregating systems, where the atomic sizes, and hence coverage for a "saturated" boundary, may vary, it will be helpful to have a description for the grain boundary coverage that constitutes a monolayer. The definition that will be used is due to Hondros and Seah (1977)

> "a monolayer contains $a^{-2}$ segregant atoms per unit area where $a^3$ is the atomic volume of the segregant. The atomic volume is usually determined from the first compound that occurs if the solute concentration is increased just beyond the solubility limit"

Obtaining $\Gamma$ from characteristic X-ray intensities in XEDS is a relatively straightforward procedure, although it requires a good knowledge of the interaction volume. Starting from the Cliff-Lorimer equation (Cliff and Lorimer (1975))

$$\frac{C_A}{C_B} = k_{AB} \frac{I_A}{I_B} \tag{3.12}$$

where the concentrations in the interaction volume, $C_A$ and $C_B$, are related to the intensities above background in the X-ray spectrum, $I_A$ and $I_B$ by a single constant $k_{AB}$. The k-factor, $k_{AB}$, can be determined experimentally or calculated theoretically (Wood et

al. (1984), Goldstein et al. (1986)). For grain boundary segregation the relative concentrations within the interaction volume, V will be given by

$$\frac{C_s}{C_m} = \frac{\Gamma A}{\rho V}\frac{A_s}{A_m} \tag{3.13}$$

where $A$ is the area of the grain boundary contained within the interaction volume, $A_s$ and $A_m$ are the atomic masses of the segregant and matrix respectively, and $\rho$ is the density (in atoms/nm$^3$) of the matrix. It follows from equations 3.12 and 3.13 that $\Gamma$ will be given by

$$\Gamma = \rho\frac{A_m}{A_s}k_{sm}g(d,h)\frac{I_s}{I_m} \tag{3.14}$$

where g(d,h) is a geometric factor related to the interaction volume (as g(d,h)=V/$A$) and will be a function of the incident probe size, d, and the specimen thickness, h.

For the case where we assume a probe of diameter d and no beam broadening then the interaction volume is simply described as a cylinder and

$$g(d,h) = \frac{\pi}{4}d \tag{3.15}$$

If we include beam broadening, b, which is a function of h, and a truncated cone model for the interaction volume then

$$g(d,h) = \frac{\pi}{4}\left(\frac{d^2 + bd + b^2/3}{d + b/2}\right) \tag{3.16}$$

If instead equations 3.8-10 are used to describe the electron intensity distribution, it can be shown that

$$g(\sigma,h) = \sqrt{\pi}\left[\frac{1}{h}\int_0^h \frac{1}{\sqrt{2\sigma^2 + \beta t^3}}\right]^{-1} dt \tag{3.17}$$

This expression is somewhat more complicated than the other approaches and the integral in this equation must be evaluated numerically, but it should provide more accurate values for segregant levels.

The values for g(d,h) as a function of thickness for these three models are shown in Figure 3.6 for a matrix of Cu (the values for Ni will be negligibly different) . The conditions chosen are the typical experimental conditions of a beam energy E = 300 keV and d = 1.4 nm (FWTM). The truncated cone model has been evaluated using incident beam diameters at both FWTM and FWHM.

It is evident from Figure 3.6, that the three models produce very different values for g(d,h). For example, at 100 nm , g(d,h) varies between 1 and 5. That is, the measured level of segregation could vary by a factor of 5, depending on how the interaction volume is estimated.

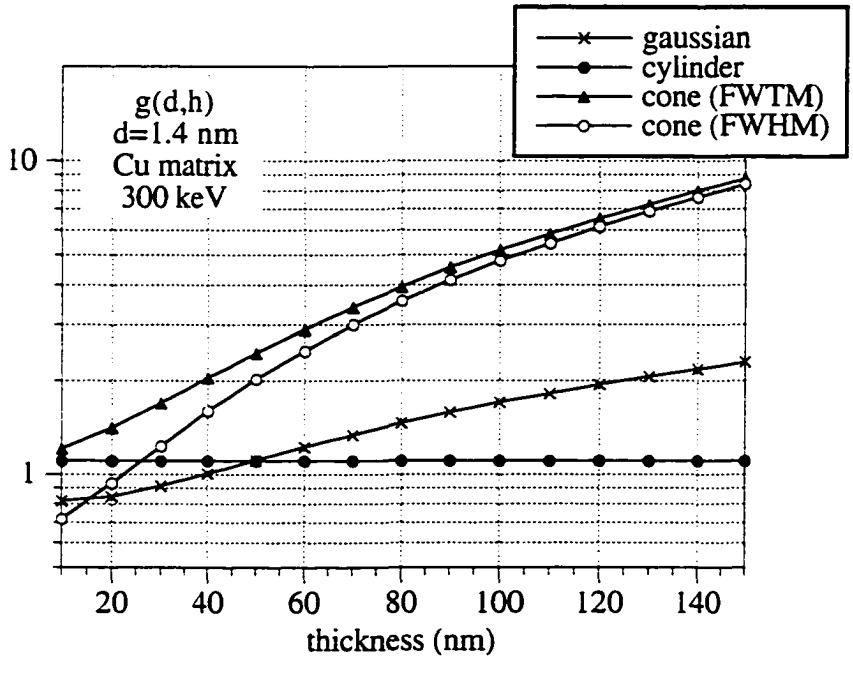


Figure 3.6 Calculations of the geometrical factor, g(d,h), for the different models of the interaction volume, as contained in equations 3.15 (cylinder), 3.16 (cone) and 3.17 (Gaussian).

To improve accuracy of quantification, by reducing uncertainties in the interaction volume, a raster scan can be used (Ikeda et al. (1993)). The interaction volume is then simply a rectangular prism and

$$g(d,h)=w \tag{3.18}$$

where $w$ is the width of the scan perpendicular to the boundary. As demonstrated by Alber et al. (1997), neglecting beam broadening may still reduce the accuracy of quantification (for example, a 20% overestimate of $\Gamma$ for $w$ = 16 nm and 150 nm of Cu-5 wt% Bi at 100 keV (Alber et al. (1997))). If the electron probe has the Gaussian intensity distribution, $I_{probe}$, given by equation 3.8 then the total electron distribution I(x,y,t) describing the raster scan is given by

$$I(x,y,t)=\int_0^w\int_0^l I_{probe}(x-x_b,y-y_b)dx_b dy_b \tag{3.19}$$

That is

$$I(x,y,t)=\frac{I_0}{4}\mathrm{erf}\left(\frac{x-w}{\sqrt{2\sigma^2+\beta t^3}}\right)\mathrm{erf}\left(\frac{y-l}{\sqrt{2\sigma^2+\beta t^3}}\right) \tag{3.20}$$

where $w$ is the dimension of the raster scan perpendicular to the boundary and $l$ is the dimension parallel to the boundary. The expression for the geometrical factor g(σ,h) becomes

$$g(\sigma,h)=\left[\int_0^h\int_{-\infty}^{\infty}\mathrm{erf}\left(\frac{x-w}{\sqrt{2\sigma^2+\beta t^3}}\right)dtdx\right]\Bigg/\left[\int_0^h\mathrm{erf}\left(\frac{-w/2}{\sqrt{2\sigma^2+\beta t^3}}\right)dt\right] \tag{3.21}$$

which in turn simplifies to

$$g(\sigma,h)=-hw\Bigg/\int_0^h\mathrm{erf}\left(\frac{-w/2}{\sqrt{2\sigma^2+\beta t^3}}\right)dt \tag{3.22}$$

Figure 3.7 shows values for g(σ,h) calculated from this equation, divided by *w* (equation 3.18). Once again d = 1.4 nm, E = 300 keV and the matrix is Cu. Figure 3.7 indicates that for a raster scan under these conditions, the assumption that the interaction volume is a rectangular prism will, in most cases, be sufficient. Beam broadening at 300 keV will not have a significant effect on measured segregation levels. Even at 150 nm, beam broadening will only introduce a ~5% error when scanning at 10 MX. Generally analysis is done with specimens thinner than 150 nm and often with larger areas scanned. There is a clear advantage to using a raster scan when accurate quantification levels are required and detectability is not a limitation.

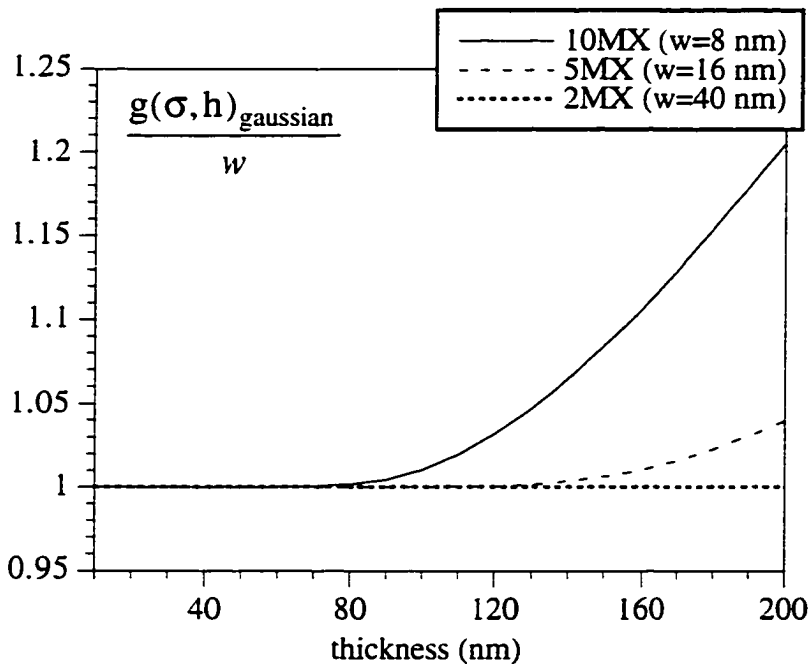


Figure 3.7 The effect of beam broadening on the quantification of a segregant when using raster scan. The actual geometric factor, g(σ,h), divided by *w* (g(d,h) for the nominal raster volume) is shown as a function of thickness for raster scans at 2, 5 and 10 MX.

In summary, although in principle quantification of a grain boundary segregant should be relatively straightforward, assumptions about the interaction volume must be made.

There is considerable uncertainty in the details of the interaction volume and it directly influences measured segregation levels through a geometrical factor, defined as g(d,h) above. When using spot mode in particular, the assumptions made will be very important and accurate quantification will require good knowledge of the probe size and specimen thickness. Using a raster scan vastly improves the accuracy of measured segregation levels, but this will be at the expense of detection sensitivity.

*3.1.4 Minimum Detectability*

An elemental peak in an X-ray spectrum will be statistically significant when the intensity in this peak, I, (including background) is given by

$$I - I^b \geq 3\sqrt{I} \tag{3.23}$$

where $I^b$ is the intensity in the background under this peak. At the detectability limit $I \approx I^b$ and so, using equation 3.14 we find that the minimum detectable amount of segregant will be given by

$$\Gamma_{min} = \rho \frac{A_m}{A_s} k_{sm} g(d,h) \frac{3\sqrt{I^b_s}}{I_m} \tag{3.24}$$

where $I^b_s$ is the intensity in the background under the elemental peak for the segregant and $I_m$ is the intensity in the elemental peak for the matrix. This analysis has neglected errors in determination of the background. We also know that

$$\begin{aligned} I_m &\propto i_b h \\ I^b_s &\propto i_b h \end{aligned} \tag{3.25}$$

and so for a given system

$$\Gamma_{min} \propto g(d,h) \frac{1}{\sqrt{i_b}} \frac{1}{\sqrt{h}} \tag{3.26}$$

If we temporarily neglect beam broadening (i.e. assume g(d,h) is given by 3.15), then $\Gamma_{min} \propto d/\sqrt{i_b}$. This demonstrates, as we might expect, that the most important parameter of the electron probe, in terms of detectability of a grain boundary segregant, is the current density, J. Interestingly, in the VG 603 for the 30μm VOA, J ≈ 0.3 nA/nm$^2$ and for the 50μm VOA, J ≈ 0.3 nA/nm$^2$. That is, neglecting beam broadening, the choice of aperture is arbitrary in terms of detection sensitivity of a grain boundary segregant. However, in the extreme limit of a very thick sample, where the interaction volume is almost completely dominated by beam broadening, it would be advantageous to use the larger aperture, as it will significantly increase the probe current without altering the interaction volume greatly. Thus, when beam broadening is included, detectability is a more complex function of the probe size and thickness. Figure 3.6 shows the right hand side of equation 3.24 as a function of thickness and probe size in the VG 603 for a matrix of Cu. The expression for g(d,h) based on the Gaussian model and given in equation 3.17 was used.

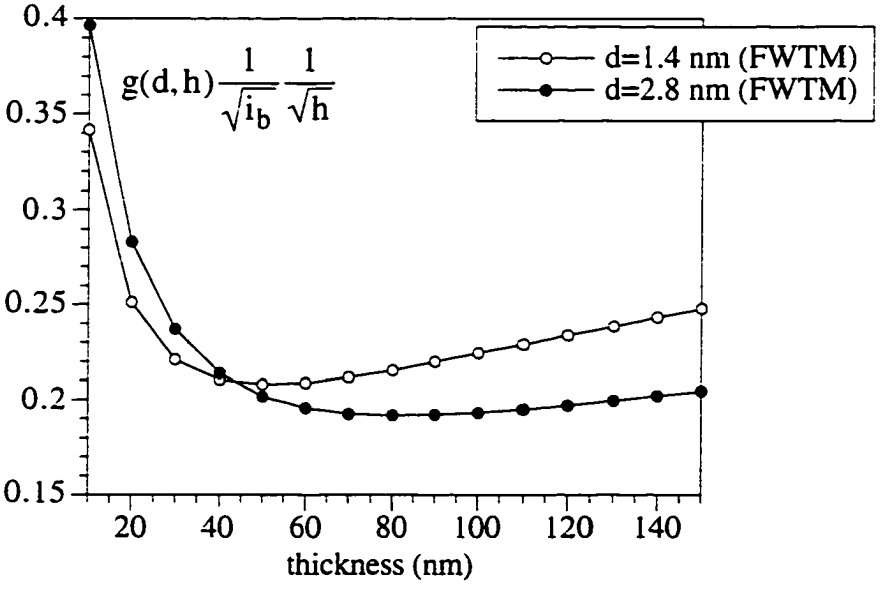


Figure 3.8 Detectability (equation 3.24) as a function of thickness for two of the optimal probe sizes available in the VG 603.

Figure 3.8 demonstrates, perhaps counterintuitively, that optimum detectability is not necessarily achieved in the thinnest samples (see also Doig and Flewitt (1982)) and, unless we are limited for some other reason to very thin samples, the smaller probe size also does not give optimum detectability. It should be noted that the detectability for the case of a raster scan is significantly worse and is off the scale of Figure 3.8.

### *3.1.5 Modeling an Equilibrium Segregation Profile*

As outlined previously, an experimentally measured segregation profile can be modeled as a convolution of the actual segregation profile with the electron distribution (equation 3.11). Assume for the time being that the segregant lies only on a 2D plane, oriented perpendicular to the beam, that is, C(x,y,t) = 0 except when x = 0 and is independent of y and t. Once again, we now need to assume an electron distribution.

For the simplest case of a cylindrical interaction volume, i.e. no beam broadening and a beam diameter d, equation 3.11 simplifies to

$$I(x) = K i_b \Gamma \frac{4h}{\pi d^2} \sqrt{d^2 - 4x^2} \qquad (3.27)$$

Quite often, profiles are plotted as a ratio of the segregant intensities to the matrix intensities, in which case, assuming the matrix is homogeneously distributed,

$$I_m = K_m i_b \rho h$$

and

$$\frac{I_s}{I_m}(x) = \frac{1}{k_{sm}} \frac{\Gamma}{\rho} \frac{A_s}{A_m} \frac{4}{\pi d^2} \sqrt{d^2 - 4x^2} \qquad (3.28)$$

Equation 3.28 will only be appropriate if the matrix signal is not reduced at the grain boundary due to the segregant.

Beam broadening can be included by using the truncated cone model, where the diameter of the cone at thickness t is given by $d+At^{3/2}$. The coefficient A comes from equation 3.7 and is a function of the matrix material and the beam energy.

$$I(x) = Ki_b\Gamma\frac{2}{\pi}\int_0^h \frac{1}{\left(d+At^{3/2}\right)^2}\sqrt{\left(d+At^{3/2}\right)^2 - x^2}\,dt \qquad (3.29)$$

This expression is considerably more complex than 3.28 and must be evaluated numerically. If instead we assume the Gaussian electron distribution as described by Equation 3.8 then we find

$$I(x) = Ki_b\Gamma\frac{1}{\sqrt{\pi}}\int_0^h \frac{1}{\sqrt{2\sigma^2+\beta t^3}}\exp\left(-\frac{x^2}{2\sigma^2+\beta t^3}\right)dt \qquad (3.30)$$

This expression will be no more difficult to evaluate numerically than that for the truncated cone model and is probably more accurate. We can also relax the assumption about a 2D grain boundary plane, and instead assume a concentration $C_0$ (in wt%) within a slab of width D at the grain boundary and we obtain

$$I(x) = K' i_b C_0\frac{1}{\sqrt{\pi}}\int_0^h \mathrm{erf}\left(\frac{x+D/2}{\sqrt{2\sigma^2+\beta t^3}}\right) - \mathrm{erf}\left(\frac{x+D/2}{\sqrt{2\sigma^2+\beta t^3}}\right)dt \qquad (3.31)$$

The grain boundary concentration, $C_0$, will have an equivalent number of segregant atoms to a 2D grain boundary with a coverage given by

$$\Gamma = C_0\rho D\frac{A_m}{A_s}$$

We will need to include the attenuation of the matrix signal due to the reduced amount of matrix material within this slab and we find

$$\frac{I_s}{I_m}(x) = \frac{1}{k_{sm}} \frac{C_0 f(x)}{(h - C_0 f(x))}$$

where $f(x)=I(x)/(Ki_bC_0)$.

As an example, $I(x)/(Ki_b\Gamma)$ for these different models is shown in Figure 3.9 for the case of a matrix of 100 nm of Cu, a 300 keV electron beam and $d_{FWTM}$=1.4 nm. The "slab boundary" has been taken to contain the same number of segregant atoms as the planar boundary and to be 2 nm wide. It can be seen that the widths, heights and shapes of these profiles are very different, depending on the model chosen. In Section 5.1.1 experimental profiles will be compared to these different models, so as to determine which model will best and most simply, describe the experimental profiles and consequently provide the best description of the interaction volume.

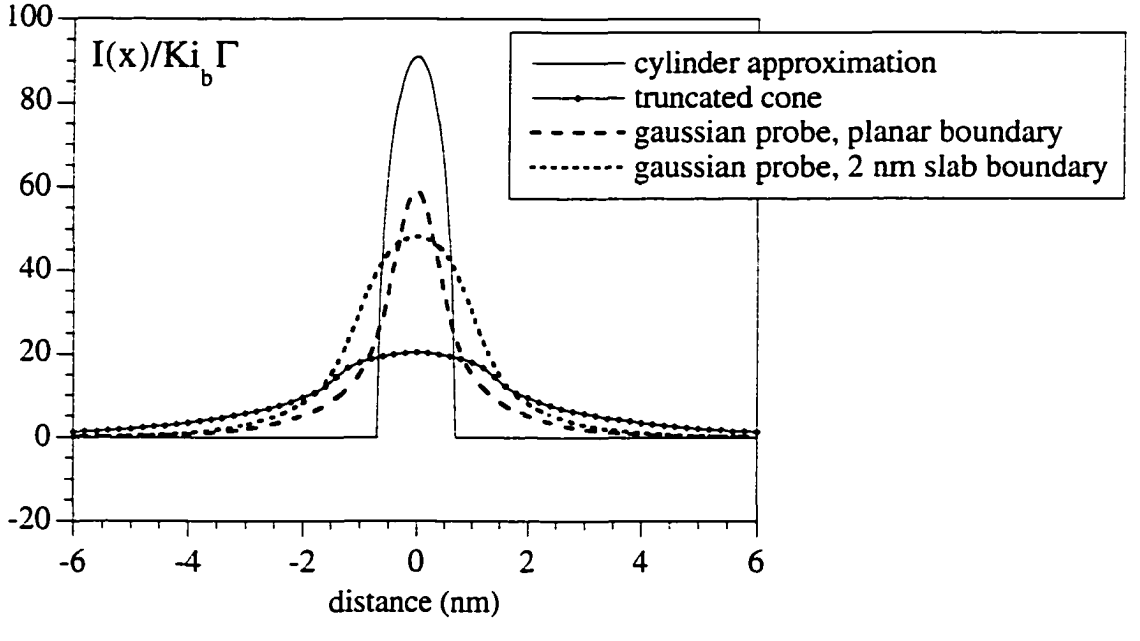


Figure 3.9 Profiles of grain boundary segregation, using the different approaches to modeling for a matrix of 100 nm of Cu and a 300 keV electron beam.

We can also consider a grain boundary inclined to the electron beam. For a 2D grain boundary plane with a projected width, due to inclination, of W (see Figure 3.10a) and a Gaussian probe

$$I(x) = Ki_b\Gamma\frac{1}{\sqrt{\pi}}\int_0^h \frac{1}{\sqrt{2\sigma^2+\beta t^3}}\exp\left(\frac{-(x-Wt/h)^2}{2\sigma^2+\beta t^3}\right)dt \qquad (3.32)$$

whereas for an inclined slab (see Figure 3.10b)

$$I(x) = Ki_bC_0\frac{1}{\sqrt{\pi}}\int_0^h \mathrm{erf}\left(\frac{x-Wt/h}{\sqrt{2\sigma^2+\beta t^3}}\right)-\mathrm{erf}\left(\frac{x-D-Wt/h}{\sqrt{2\sigma^2+\beta t^3}}\right)dt \qquad (3.33)$$

The profiles produced by these descriptions will have an asymmetric shape. Grain boundary inclination may be an important factor, as it is experimentally difficult to tilt a grain boundary precisely on axis. Generally is considered that the boundary inclination can be set within 1-2°. A boundary in a 100 nm thick foil, with a 2° tilt will have a projected width of 3.5 nm, and it is quite probable that the profiles obtained from such a boundary would reflect this grain boundary inclination.

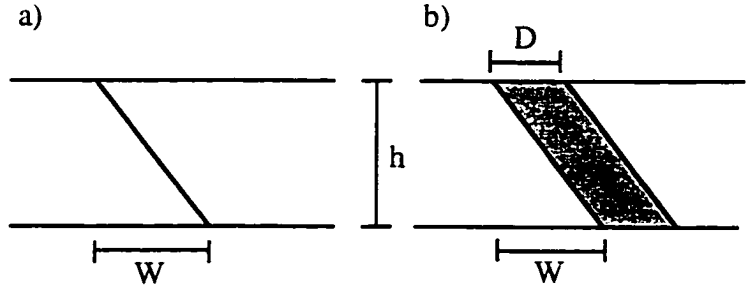


Figure 3.10 Schematic of a) an inclined planar boundary and b) an inclined slab

Segregation can be described by more complex distributions than a two dimensional plane or a homogeneous slab and both Gaussian (Hall et al. (1981)) and exponential decay (Doig and Flewitt (1982)) functions have been used. However, increasing the

complexity of the concentration distribution, increases the complexity of the mathematics considerably. The actual segregation distribution is expected to be much narrower than the measured distribution and so assumptions about the actual distribution are to a certain extent arbitrary For example, the theoretical profile generated by a planar grain boundary and a 0.2 nm slab (the typical spacing of the close packed planes in Cu) are indistinguishable. Using the simplest models is probably adequate.

## 3.2 ELNES and the DOS

### *3.2.1 Theoretical Description*

In Chapter 2 it was stated that the ELNES contains information about the local DOS. To understand how this relationship arises, consider Figure 3.11. Ionization edges occur when the incident electron excites an electron from the core shell of an atom in the sample into an unoccupied state above the Fermi level.

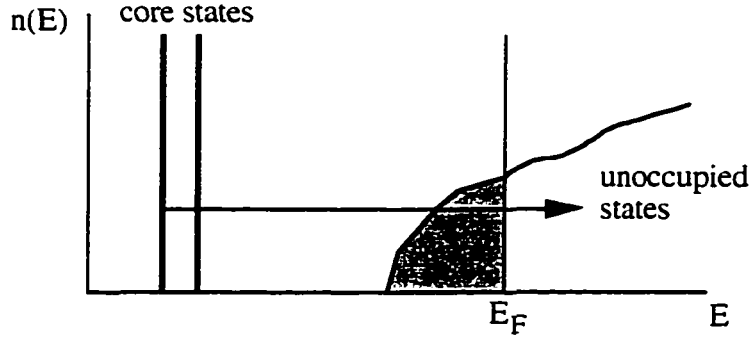


Figure 3.11 Schematic of the electronic transitions which produce ionization edges in the electron energy loss spectrum. n(E) is the number of electrons with energy E.

We can describe the initial and final state of the electron in the sample that undergoes the transition with wavefunctions $|i\rangle$ and $|f\rangle$ respectively. If it is then assumed that the incident electron can be expressed as a plane wave in both initial and final states, then

the differential cross section for such a transition, with a momentum transfer q, is (Manson (1978))

$$\frac{d^2\sigma}{d\Omega dE} = \frac{4\gamma^2}{a_0{}^2q^4}\left|\langle f|\exp(i\mathbf{q}\cdot\mathbf{r})|i\rangle\right|^2\rho(E) \qquad (3.34)$$

$\rho(E)$ is the density of final states with energy E. The term $\gamma$ is the usual relativistic correction and $a_0$ is the Bohr radius. Note that this approach is a one-electron approximation, that is, the excitation process has no effect on the remaining electrons in the sample and all electrons experience the same effective potential. It should be noted that a very similar expression to 3.34 describes the XAS process and that XAS and EELS are entirely analogous (Sawatzky (1991)).

In the limit where $\mathbf{q}\cdot\mathbf{r} << 1$, the exponential term in equation 3.34 can be approximated as

$$\exp(i\mathbf{q}\cdot\mathbf{r}) \approx 1 + i(\mathbf{q}\cdot\mathbf{r}). \qquad (3.35)$$

This is equivalent to assuming a small momentum transfer, which is practically achieved by limiting the angular distribution (< 50 mrad) of the electrons that contribute to spectrum by using a small entrance aperture to the spectrometer. The initial and final states are assumed to be orthogonal so $\langle f|i\rangle=0$ and we have

$$\frac{d^2\sigma}{d\Omega dE} = \frac{4\gamma^2}{a_o{}^2q^2}\left|\langle f|r|i\rangle\right|^2\rho(E) \qquad (3.36)$$

There are two contributions to the scattering cross section in equation 3.36, the matrix term $\langle f|r|i\rangle$ and the unoccupied DOS term $\rho(E)$. The matrix term is an overlap integral between the initial and final states and is generally found to be slowly varying with E. This term gives the basic edge shapes (Leapman et al. (1980)) and is modulated by the

DOS term. The area under the ionization edges can be used to determine the relative concentrations of elements in the sample, given that the cross sections can be calculated. Normally only the matrix term is used to calculate cross sections and details about the quantification techniques can be found in Egerton (1996). The DOS term produces oscillations superimposed on the basic edge shape and it is this term that contains information about the local environment and bonding.

A consequence of the assumption of small q is that the well-known dipole-selection rules will now apply (see French and Taylor (1979) or an alternative quantum mechanics text for a discussion of dipole-selection rules). The dipole-selection rules state that if l and l' are the angular momentum quantum numbers of the initial and final state respectively, then only transitions that satisfy $l'=l\pm1$ can occur. This can be partially understood based on symmetry arguments; for the overlap integral of the matrix term to be non-zero, the final and initial states wavefunctions must have opposite parity, which is only satisfied when l is even (odd) and l' is odd (even). In an EEL spectrum, K edges arise from excitations of electrons from 1s states where l=0. Therefore, only unoccupied p states (l'=1) are accessible in this transition. Similarly $L_{23}$ edges arise from excitations from 2p states, so both s (l'=0) and d (l'=2) states are accessible. Another important consequence of the matrix element follows from the fact that the initial state is highly localized to the excited atom. For the overlap integral, $\langle f|r|i\rangle$, to be non-zero, the final state must also be localized to this atom, and hence ELNES measures a local DOS. Because of the matrix term, the EELS is often described as measuring an unoccupied symmetry- and site-projected DOS.

In many cases it is found that the observed ELNES exhibits a structure specific to the arrangement and type of atoms in the first coordination shell. This kind of structure is sometimes called a "coordination fingerprint" (Brydson et al. (1992)). Coordination

fingerprints are expected to arise when the DOS is dominated by the bonding of the probed atom with its nearest neighbors. The band structure of molecular or ionic solids may often be directly related to the molecular orbitals of the molecular or ionic building blocks. As an example, the ELNES of graphite ($sp^2$ bonded) displays a peak due to transitions to the empty $\pi^*$ states whereas this peak is absent in the ELNES of diamond which is $sp^3$ bonded (no $\pi^*$ states) (Egerton and Whelan (1974)). Coordination fingerprinting allows the interpretation of the ELNES of a material for which the electronic structure is unknown by comparing it to a large number of near edge structures of reference materials. For example, there has been considerable work done with copper compounds in the hope of obtaining insight into the electronic structure of the cuprate high temperature superconductors (Lytle and Greegor (1988), Fink et al. (1994)).

The energy of the ionization edge onset is often observed to shift depending on the atomic environment of the probed atom, and this is generally termed a chemical shift. It might be thought that, in a similar manner to XPS, the valence state of the probed atom could be determined from these chemical shifts. In EELS the energy of the edge onset is given by the difference between the energy of the core states and the lowest unoccupied state and so observed chemical shifts are not usually easily interpretable. The energy of the unoccupied states will be influenced by direct bonding effects and there is rarely any simple correlation between edge energy and valence state. For example, the creation of a band-gap going from a metal to an insulator would cause a chemical shift which is in addition to the shift produced by the change in energy of the core states. Other effects make interpretation difficult, such as core-hole effects, to be discussed below. This complexity of the chemical shifts observed in EEL spectra has meant that there has been

little systematic work done. Brydson et al. (1992) gives a good review of the available chemical shift data.

Core-hole effects are due to the breakdown of the one electron approximation. When the electron is excited out of the core state it leaves behind a so-called core-hole. The presence of the core hole can modify the final state DOS. The energy of the available final states will be lowered, and in some cases, bound states below the conduction band, called core excitons can be produced. Therefore, the energy of the edge onset and even the details of the fine structure can be influenced by many electron effects. The degree to which the core-hole affects the ELNES will depend on the ability of the valence electrons to screen the effect of the core-hole from the unoccupied DOS. For metals where the valence electrons are often described as "free-electron like", screening is expected to be quite good and core-hole effects are relatively unimportant (Egerton (1996)).

It some cases it is possible to obtain some information about the electronic structure of a material from a simple analysis of the ELNES but, to completely understand the details of the near-edge structure, quantum mechanical calculations of the electronic structure should be performed. There are a number of techniques to do this (see Brydson (1991), Rez (1992) and Rez et al. (1995)) for reviews of the available calculation methods) and the suitability of each of the techniques will depend to some extent on the material under investigation. In the light of the earlier discussion, regarding the description of the band structure in terms of molecular orbitals, there are calculation approaches based on molecular orbital approaches, i.e. to take a linear combination of atomic orbitals (LCAO). One formulation of the molecular orbital approach that has found some application is the SCF-X$\alpha$ method, already mentioned in Section 2.3.

Band structure calculations can also be performed. However, not all of the available band structure calculations allow the resultant DOS to be resolved into the appropriate symmetry-projected components at a particular atomic site and hence cannot be directly compared to experimental ELNES. The Augmented Plane Wave (APW) method has been applied in spectrum analysis (Muller et al. (1982)) as has the Augmented Spherical Wave (ASW) method (Neckel et al. (1976), Grioni et al. (1992)). A reformulation of the psuedopotential method so as to give symmetry-projected states has also been used (Weng et al. (1989)). Finally the layer Korringa-Kohn-Rostoker (KKR) method has recently been applied to ELNES and shows potential for situations where the symmetry of the lattice is broken, at grain boundaries for example, which are not amenable to other band-structure calculations (Rez et al. (1998)).

A different approach to understanding ELNES is based on the "XANES" calculations where the near edge structure is calculated from the interference between the outgoing electron wave of the ejected electron and the electron wave that has been backscattered from the surrounding atoms (see for example Vvedensky et al. (1986), Weng and Rez (1988)). The XANES approach has been extensively used in the interpretation of the fine structure in XAS for which it was developed, but it is not accurate for states just above the Fermi energy.

As can be seen there are number of different theoretical methods that can be used to aid interpretation of the ELNES and no one technique has been determined to be the best for all problems. There are examples where each of the techniques has been shown to give reasonable agreement with experiment (the reviews by Brydson (1991), Rez (1992), Rez et al. (1995) show such examples). Differences between experiment and theory will also occur when many electron effects are important, as the calculations nearly always assume the ground state. Understanding changes in electronic structure at grain

boundaries is an even more challenging problem and there are relatively few studies done; some of these were mentioned in Chapter 2. Real-space methods such SCF-Xα and XANES calculations allow the use of atomic clusters which can be chosen to represent the atomic structural units at the grain boundary. With the exception of the layer KKR method, the reciprocal-space, band-structure calculations (APW, ASW and psuedopotential methods) will require large unit cells in order to properly model grain boundaries and therefore will be computationally intensive.

### *3.2.2 Transition Metals*

One class of materials in which the gross structure in the ELNES is reasonably readily interpretable, is the transition metals and their alloys, and will be of particular importance in this work. Figure 3.12 shows the ionization edges for the 3d transition metals .

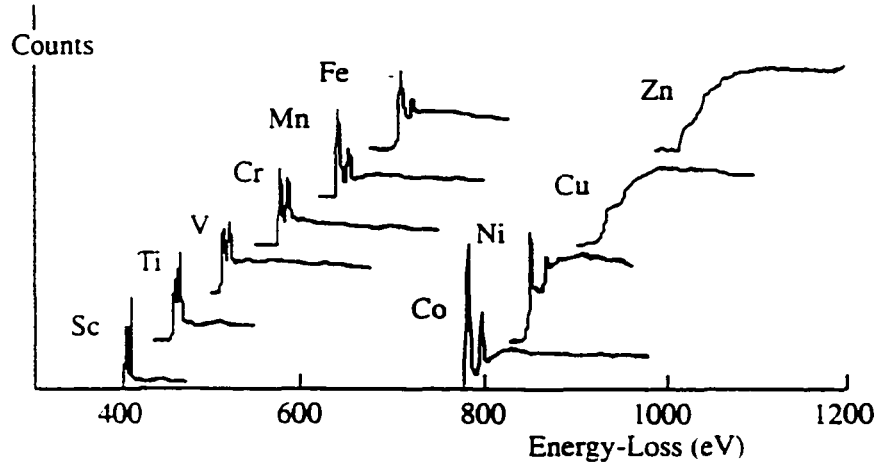


Figure 3.12 EELS ionization edges for the 3d transition metals (Taken from Williams and Carter (1998), modified from original plot of Zaluzec (1982)).

The electronic structure of the transition metals is dominated by a relatively narrow, tightly-bound d-band, the occupancy of which depends on the atomic number.

Transitions to these unoccupied d-states produce a sharp peak in the $L_{23}$ ionization edges, traditionally called white lines. Similar white lines to those shown in Figure 3.12 are also observed for the 4d transition metals. For most elements, there are two peaks visible in the spectrum and these are produced by the spin-orbit splitting of the initial state. The lowest energy peak is the $L_3$ edge (initial state $2p_{3/2}$) and the next is the $L_2$ edge (initial state $2p_{1/2}$). There is also an $L_1$ edge (transitions to p states from 2s states) but this is a smaller broader step function superimposed on the tail of the $L_{23}$ edge and has low visibility. There is some debate, due to the tightly bound nature of the d-band, as to whether the white lines are correctly described as DOS features (Grioni et al. (1989)), but given that the d-band can be adequately modeled using band structure calculations, the argument appears somewhat academic.

As can be seen in Figure 3.12, the intensity of the white lines decreases as the atomic number, and hence occupancy of the d-band increases, until at Cu, where all d-states are filled, there is no white line. Pearson et al. (1988) measured the intensity in the white lines for the 3d and 4d transition metals, normalized to the intensity in the continuum states, well above threshold, and compared these to the nominal filling of the d-states. When the intensities were corrected for the contribution of the transition matrix element (Pearson et al. (1993)), a proportionality between the normalized white line intensity and the d-state occupancy was observed.

An extensive experimental study of the transition metals and their oxides was performed by Leapman et al. (1982). In addition to the white line intensities of the transition metals increasing with atomic number, the widths of the white lines were observed to decrease. This is consistent with increasing occupancy of the d-band. However, the measured widths were broader than predicted values, even when broadening mechanisms, such as instrumental broadening and the finite lifetimes of the core hole and excited states, were

included. Also observed by Leapman et al. (1982) were anomalous values for the $L_3$:$L_2$ intensity ratio. The expected ratio of $L_3$ to $L_2$ is 2:1. This follows from the 2j+1 (j=l+s. s=spin state) degeneracy of the initial states. The white line intensity ratio was found to vary from 0.8:1 for Ti to 3.3:1 for Ni and to also be a function of the oxidation state. The anomalous white line ratios were believed to be a consequence of many electron effects.

So far only the elemental transition metals have been discussed, but significant differences in the energy, intensity and fine structure of the white lines are observed when the transition metal is bonded to other elements. For example, the intensity of the white lines in the transition metal oxides (Leapman et al. (1982)) is larger than that of the metal. The extreme case is illustrated in Figure 3.13, for Cu and the Cu oxides (experimental spectra obtained from reference materials), where a white line is now observed upon oxidation.

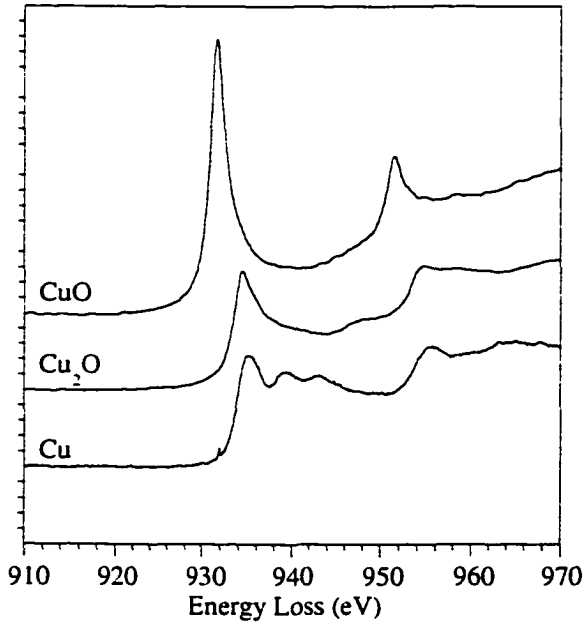


Figure 3.13 $L_{23}$ edges of Cu and the Cu oxides.

The effect of the ionic bond with O is to remove electrons from the d-band and hence there are more d-states available for the transition. It is dangerous to interpret all white lines as being a consequence of such a charge transfer. The example of $Cu_2O$ in Figure 3.13 being a case in point, as $Cu_2O$ formally has an electron configuration of $3d^{10}$ and therefore the white line is more likely to be a consequence of s-d rehybridization. Similarly the changes in intensity of the $L_{23}$ edges in the Ni-Al system and other transition metal aluminides is believed to be due to hybridization of the transition metal d-states with the Al p states (Botton et al. (1996), Muller et al. (1998)). An increase in white line intensity in the $L_{23}$ edge of a transition metal can tell you that there are less electrons in the d-band, but does not necessarily determine whether charge transfer or bond rehybridization is responsible.

Other effects are also observed in the white lines of the transition metals when the atomic environment is changed. In addition to a change in the absolute intensities in the white lines increasing, the ratio of $L_3$:$L_2$ intensities will also change, but an examination of this effect for a series of Mn and Fe oxides (Paterson and Krivanek (1990)) showed that it is difficult to determine any direct relationship between $L_3$:$L_2$ and oxidation state. Sometimes the white lines in transition metal compounds are observed to split into two or more peaks and these are a consequence of crystal field effects. That is, the different symmetries of the different d-orbitals interact with the nonspherical symmetry of the atomic environment in the crystal and the degeneracy of the d orbitals is lost.

In summary, the $L_{23}$ ionization edges in the EELS spectrum for the transition metals contain information about the shape and filling of the d-band. This information is important because it will be related to material properties and will be discussed further in Chapter 6. With the spatial resolution obtainable in a STEM, it should be possible to

investigate how the d-band, and hence material properties are altered at a grain boundary after segregation of an embrittling impurity.

# 4. EXPERIMENTAL PROCEDURE

## 4.1 Materials

### *4.1.1 S-doped Ni*

The Ni-S material was provided by Westinghouse-Bettis in the form a button with a pre-melt chemistry of Ni-0.03%S. It had been given three successive anneals at 1000°C for 1 hour, each time followed by rolling for a reduction of 30%. A piece of this button was encapsulated in an evacuated (< $10^{-6}$ Torr) quartz tube and given a final recrystallization anneal of 1000°C for 1 hour. This was followed by a 48 hour anneal at 650°C to produce segregation. From Mulford (1983) this should be sufficient to produce equilibrium segregation of S at the grain boundaries. As a check to ensure that the S will not diffuse out of the material during the heat treatment, using diffusion coefficients of S in Ni taken from Hotzler and Castleman (1972), $\sqrt{Dt}$ for the heat treatments above is on the order of $10^{-3}$ cm whereas the thickness of the piece was 0.7 cm.

### *4.1.2 Bi-doped Cu*

Bi doped materials were provided by three different sources. D. E. Luzzi of the University of Pennsylvania provided samples of the material that had been used in HREM studies of $\Sigma$=3 grain boundaries (Luzzi (1991)). This material was in the form of a 5 mm diameter rod with Bi content of 12 at ppm. Previous treatment had involved swaging from 1 cm diameter followed by solutionizing at 850°C. In the final treatment the rod was further swaged to 3 mm diameter. A piece of this rod was encapsulated in an evacuated quartz tube (<$10^{-6}$ Torr) with chips of another Cu-Bi alloy and annealed at 600°C for 48 hours. The larger surface area of chips supplies the necessary vapor pressure to prevent rapid Bi loss. This treatment has been shown to produce a large

population of Σ=3 {111}/{111} grain boundary facets (Blum et al. (1990)) and was that used by Luzzi (1991).

Bi-doped bicrystals with the Σ=3 {111}/{111} orientation with a composition of 100 wt ppm were supplied by L. -S. Chang and U. Alber of Max-PlanckInstitut, Stuttgart. They had been annealed at 500°C for a time long enough to reach thermodynamic equilibrium (2-3 weeks). They were provided in the form of 3 mm discs , ~ 200 μm thick with the boundary oriented in cross section (perpendicular to the surface of the foil).

The final material was a Cu-Bi alloy provided by J. D. Embury of Los Alamos National Laboratory. A Cu billet and a Bi donor were sealed in an evacuated quartz tube in such a way that no direct contact between the two metals could occur. They were annealed at 850°C for 16 hours, during which time diffusion of Bi, from the vapor state, into the Cu billet occurs. This was followed by a further heat treatment of 8 hours at 550°C which should produce grain boundary segregation. This material was shown to be intergranularly brittle (J. D. Embury, private communication).

*4.1.3 Ag-doped Cu*

To obtain Ag-doped Cu specimens, a similar procedure to one that had already been used successfully to obtain Bi-doped Cu specimens (Baumann and Williams (1981), Michael and Williams (1984), Bruley et al. (1996), Keast et al. (1998)), was chosen. The starting material was 250 μm thick foil of 99.999% pure Cu, from which 3 mm discs were punched out and mechanically polished down to ~100 μm. These discs were then encapsulated in an evacuated (< $10^{-6}$ Torr) quartz tube and annealed at 700°C to remove cold work. Ag (99.999% pure) was evaporated onto both sides of the discs and they were once again encapsulated and annealed at 500°C for 2 hours.

This time and temperature were chosen as being sufficient to ensure diffusion of Ag into Cu, the dominant mechanism being through grain boundary diffusion. The time, t, required to diffuse a species in from both sides of a slab, width 2L, so that the concentration in the center is 90% of that at the surface, is given by (see Appendix B for a derivation)

$$t = 0.86\frac{L^2}{D} \qquad (4.1)$$

where D is the diffusion coefficient. At 500°C, the diffusion coefficient for grain boundary diffusion of Ag in Cu is $D_{gb}=2.1\text{x}10^{-7}$ $cm^2/s$ (Schoen et al. (1979)). For a slab of width 200 μm, t=6.7 minutes. Therefore, 2 hours at this temperature should be more than sufficient to allow Ag to penetrate all the grain boundaries in the specimen. It should be noted at this point, that an excess concentration of Ag at the grain boundaries produced in this way, may not necessarily be equivalent to equilibrium segregation.

*4.1.4 Sb-doped Cu*

Sb-doped Cu specimens were made in a very similar manner to the Ag-doped specimens. However, the diffusion of Sb into Cu is reported to be very much slower than that for Ag (Halimi and Merabet (1990)). At 500°C, $D_{gb}=1.8\text{X}10^{-11}$ $cm^2/s$, in which case t=56 days! This time is reduced to 124 minutes if the anneal temperature is increased to 900°C. At this temperature, rapid grain growth will occur. To avoid obtaining an excessively large grain size, and consequently few grain boundaries in the final TEM specimen, the initial recrystallization step was eliminated. Sb (99.9999% pure) was evaporated onto the Cu discs immediately after they were punched from the Cu foil and mechanically polished. After encapsulation, the discs were annealed for 2 hours at 900°C, at which time recrystallization, grain growth and diffusion of Sb occur simultaneously and it is hoped that the diffusion of Sb does not significantly alter the

recrystallization and grain growth behavior. This was followed by a 24 hour anneal at 500°C, which should produce grain boundary segregation and embrittlement (Bokshteyn et al. (1991)).

*4.1.5 Thin Foil Preparation*

If required, the bulk materials were sliced with an alumina or SiC blade to approximately 0.5 mm thickness and 3 mm discs punched from these slices. This was followed by mechanical polishing to ~100 μm thickness. The Cu-Ag, Cu-Sb material and the Cu-Bi bicrystals were already in the form of ~100 μm, 3 mm discs and so these steps were unnecessary. The Cu-Bi bicrystals were briefly etched in a 50% nitric acid, 50% water solution so as to reveal the grain boundaries. This facilitated producing electron transparent regions at the location of the grain boundary plane. After this point the preparation procedure for all specimens was essentially the same.

One side of the discs was polished, either with 1 μm SiC paper or with a flat polishing tool on a dimpler and 0-2 μm cubic boron nitride polishing medium. Both approaches were found to be effective. The other side of the disc was then dimpled until the final thickness was ~5-20 μm. This was followed by ion milling in a Gatan precision ion polisher (PIPS) to electron transparency. Typical milling conditions were 4 keV, 5° tilt, and double-sided milling, although often in the final thinning stages the ion beam energy was reduced to 3 keV. Preliminary examination of the specimens was performed in a Philips 400T TEM. In most cases, specimens were given a brief "cleaning" in the PIPS to remove any surface oxide or contamination immediately before insertion in the STEM. When ELNES investigations were to be performed, cleaning was always performed as surface oxide is expected to influence the fine structure. Electropolishing is another reliable, and more rapid, procedure for making TEM specimens from metallic

materials. However electropolishing may change the chemistry at the grain boundaries and so was not used in this work.

## 4.2 XEDS for Elemental Information

All elemental and compositional information was obtained using XEDS on the VG 603 at Lehigh University. Although, in principle, elemental information can be obtained with EELS with similar or better detectability limits, it is experimentally easier to use XEDS. The main difficulty with EELS arises from the low visibility of the ionization edges for the elements of interest. These edges (the Ag $M_{45}$ at 367 eV, Sb $M_{45}$ at 528 eV, S $L_3$ at 165 eV (Egerton (1996))) do not have sharp edge onsets, but display a delayed maximum and so the edge onset would only be observed as a change in slope of the exponentially decaying background. In addition the S peak sits on the tail of the Ni M edge and the Sb edge is at the same energy as O. The accessible Bi edges are the $M_{45}$ at 2600 eV, an energy higher than typically used in EELS, and the $N_{45}$ at 430 eV which has low visibility. In contrast, the X-ray spectra, for all of the systems under investigation, consist of a series of well separated, distinct elemental peaks that are easily visible above the background. An example of a comparison of the two techniques will be shown in Section 5.1.4.

The VG 603 is a dedicated STEM operating at 300 kV and designed with the goal of maximizing detection sensitivity and spatial resolution in XEDS (details about microscope design can be found in Lyman et al. (1994)). It has a FEG with an electrostatic gun lens, which allows some flexibility in source size and emission current. A system of two condenser lenses and a VOA aperture is used to control convergence angle and beam current onto the specimen. The objective lens has a symmetric field, i.e. there is another crossover after the specimen, and side-entry specimen insertion. $C_s$ is

4.3 mm for this lens which is larger than that for high resolution polepieces, but allows larger specimen tilts and most importantly allows the X-ray detectors to be placed very close to the specimen. There are also a series of projector lenses after the specimen, in addition to the post-specimen field of the objective lens. These are important for the imaging and EELS conditions but have no effect on XEDS.

As described in Section 3.1.1, typical operating conditions are with a 30 μm VOA and the 1st condenser lens switched off. This produces an electron probe containing ~0.6 nA with $d_{FWTM}$ of 1.4 nm. When a larger probe current is required the 50 μm VOA can be used, in which case the probe contains ~1.7 nA and has $d_{FWTM}$ of ~2.1 nm (N.B. this is the theoretical optimum; if the VOA is changed without altering the condenser lens settings $d_{FWTM}$ =~2.7 nm).

The VG 603 is fitted with two Oxford Instruments energy-dispersive spectrometers: a windowless Si(Li) detector with a collection solid angle of 0.3 sr and an ultra-thin window intrinsic germanium detector with a collection solid angle of ~0.2 sr. These values for solid angle are higher than those typically used in other instruments (usually < 0.15 sr) and are mainly a consequence of the close proximity of the detectors to the specimen. Both spectrometers have a 20° take off-angle. Measures have been implemented to reduce sources of stray X-rays and a beam blanking scheme can be used to increase the fraction of X-rays measured when the count rate is high, however, this was not required during these experiments. The Si(Li) detector was nearly always used.

Unless necessary, specimen tilting to orient grain boundaries perpendicular to the electron beam was not performed. Instead, grain boundaries that were close to parallel to the electron beam were chosen for analysis. Most specimens contained a sufficiently large number of grain boundaries and such a selection procedure was possible. When

maximum sensitivity was required, spectra were acquired while the electron probe was placed exactly on the grain boundary plane. Alternatively, the beam was rastered over a fixed area (usually at 2-10 MX), chosen so the boundary was still visible in this area, which allowed for more accurate quantification. Collection times were on the order of 50-100 s. For the systems under investigation the elemental peaks in the X-ray spectra are well separated, and so background subtraction and peak intensity values were obtained using simple window integrals. Profiles across grain boundaries were obtained by stepping the beam along a line perpendicular to the grain boundary and collecting a spectrum at each point. The "autopoint" routine within the Link software was used to control both the position of the electron beam and the acquisition of spectra. Each spectrum was then individually quantified and compositional profiles obtained. Dwell times were typically 10-20 s and step sizes 0.5-1 nm.

2D mapping was performed using the "digital imaging" routine within the Link software. The electron beam is stepped in a 2D array and the number of counts collected within a predefined energy window at each of these points are stored as a 2D map. Several of these energy regions can be simultaneously collected. The energy regions chosen corresponded to the energies where elemental peaks were expected to be as well as, if required, background windows. Maps were usually chosen to be at 1 MX with 64x64 pixels or 500 kX and 128x128 pixels. These conditions will ensure that the pixel size is approximately equal to the probe size and the image is correctly sampled. Dwell times for each pixel were 50-500 ms and total collection times were 20-60 minutes. These dwell times are quite short and so to increase collection efficiency further (and hence number of counts in the maps) the pulse processing time of the spectrometer was reduced. This will degrade energy resolution in the spectra. When the peaks are well separated, as for these systems, this loss of energy resolution will not affect the

resultant maps. Segregation profiles were sometimes extracted from these 2D maps, integrating over a line several pixels wide.

Quantitative information was obtained using the methods discussed in Section 3.1.3 and described by equation 3.14. Values for the k-factors were obtained from theoretical calculations and are given in Table 4.1. Quantitative values for segregation levels were obtained from experimental profiles, both those obtained directly and those extracted from maps, by scaling them to the theoretical model. Quantitative information can also be obtained directly from the map, essentially by simulating a raster scan. A subarea of the map is selected and the counts in both the segregant map and the matrix map, less backgrounds, is used to calculate intensity ratios and hence segregation levels.

Segregation levels were expressed in terms of a grain boundary coverage in atoms/nm$^2$. However, to enable comparison between the different material systems, this coverage in terms of number of monolayers was also calculated, where the definition of Section 3.1.3 for a monolayer was used. The grain boundary coverage equivalent to a monolayer is given in Table 4.1 along with the compound used to determine this.

Table 4.1. Theoretical k-factors and monolayer coverages for the systems of interest.

| System (A-B) | $k_{AB}$ | $\Gamma$(monolayer) atoms/nm$^2$ | compound |
|---|---|---|---|
| S-Ni | 0.55 | 8.5 | $\beta'$ $Ni_3S_2$ |
| Bi-Cu | 3.88 | 9.3 | Bi |
| Ag-Cu | 1.75 | 15.1 | Ag |
| Sb-Cu | 2.06 | 17.6 | $\beta$ $Cu_3Sb$ |

In the samples provided by D. E. Luzzi, it was of interest to determine if any $\Sigma$=3 boundaries had detectable levels of Bi and whether these levels were consistent with the model structure proposed for these boundaries. Each of the boundaries in those samples was characterized, using diffraction analysis in the TEM, as either $\Sigma$=3 or non $\Sigma$=3. XEDS was performed on each one of the $\Sigma$=3 boundaries and most of the non $\Sigma$=3 boundaries. Segregation levels or maximum possible boundary coverages were determined for each boundary examined.

### 4.3 EELS for Electronic Structure Information

EELS measurements were performed on the VG 501 dedicated STEM at Lehigh University, fitted with a Gatan 666 parallel EEL spectrometer (PEELS). The VG 603 is also fitted with a PEELS, however, unlike for XEDS, there is no obvious advantage in using this microscope. The VG 501 is operated at 100 kV and has an FEG. Optically it is very similar to the VG 603, with the differences that there are no projector lenses and the objective lens is non-symmetric with top entry specimen insertion. It also does not have a high-resolution polepiece (exact value for $C_S$ is unknown but is between 3-5 mm). The current density in the electron probe of the VG 603 is expected to be somewhat higher than for the VG 501, thus improving detection sensitivity. However, this is offset by the lower ionization cross section due to higher accelerating voltage. The projector lenses make obtaining EELS data on the VG 603 a considerably more complex process although, in principle, it is more flexible with regard to selection of collection angles. The projector lenses also introduce chromatic aberration and the spectrometer must be refocused depending on the energy of the ionization edge. This also means that if it is desired to collect a low-loss spectrum from the same area as an ionization edge, the spectrometer must first be refocused. In the interests of simplicity,

with no appreciable loss in performance, the VG 501 was chosen for the EELS experiments.

A 50 μm ROA was selected, with the condenser lenses set to produce a relatively high beam current. Measurements of probe size and current have not been made under these conditions but are estimated to be approximately 1 nm and 0.5 nA respectively based on the work of Mory (1985), obtained from a very similar microscope. The collection angle of spectrometer was set to 20 mrad and the spectrometer has an energy resolution of ~0.8 eV. The dispersion of the spectrometer was set to 0.2 eV per channel.

The electron probe was placed on the grain boundary and an energy loss spectrum, containing the ionization edge of interest, collected, normally with an acquisition time 40-60 s. Immediately afterwards a low loss spectrum was collected, containing the ZLP, in order to deconvolute thickness effects during post-processing. A reference set of spectra from the nearby grain (within 10 nm of the grain boundary) were also always obtained.

Each spectrum was processed by removing dark current and gain variations. The dark current is the signal produced by the detector when not illuminated by electrons and was measured by collecting a spectrum under the same conditions, but with the electron beam switched off. Channel-to-channel gain variations are a consequence of variations in sensitivity across the diode array. A quick and simple way of assessing gain variations is to collect a spectrum in a region where there are no sharp or edge features, for example the exponentially decaying region after the plasmon peak (assuming there are no ionization edges in this region). A smoothing filter is then applied to this spectrum to remove any channel-to-channel gain variations and the original spectrum divided by the smoothed spectrum. This process will not account for any long range

gain variations, but will well describe the short-range gain variations that are particularly troublesome in ELNES. The exponentially decreasing background was removed from each ionization edge and plural scattering removed by deconvolution of the low loss spectrum. Comparison of spectra collected from the grain boundary region to those collected from the bulk allowed identification of features that may be attributable to the presence of grain boundary segregants.

# 5. RESULTS

## 5.1 XEDS

### *5.1.1 S-doped Ni*

The S-doped Ni provided by Westinghouse-Bettis was extremely brittle. As an illustration of this Figure 5.1 shows an SEM micrograph of a fracture surface of this material demonstrating complete intergranular failure. This sample was broken easily by hand by bending once.


Figure 5.1 SEM micrograph of the fracture surface of S-doped Ni sample showing completely intergranular fracture.

Segregation of S to a grain boundary in this material is shown in Figure 5.2, where in 5.2a the small electron probe of the STEM was placed on the grain boundary and in 5.2b it was placed within the nearby grain. For this same boundary a segregation profile was obtained by stepping the probe across the boundary and is shown in Figure 5.3. This experimental profile has been modeled using the different assumptions for interaction volume described in Section 3.1.5. In Figure 5.3a the probe size has been assumed to be at FWTM and beam broadening is neglected. The theoretical profile for such a "cylinder model" is described by equation 3.27. In Figure 5.3b it has been

assumed the interaction volume is described by a truncated cone and the theoretical profile is that given by equation 3.29. The incident probe was taken at FWHM and a thickness of 50 nm was assumed. Finally in Figure 5.3c the gaussian model of equation 3.30 is shown, assuming a thickness of 80 nm, and this model fits the experimental profile very well. The cylinder model, with the exception of the tails of the profile describes the experimental profile surprisingly well. Scaling of the gaussian profile to the experimental profile gave a S level of $11.6 \pm 0.6$ atoms/nm$^2$ or $1.36 \pm 0.07$ monolayers.

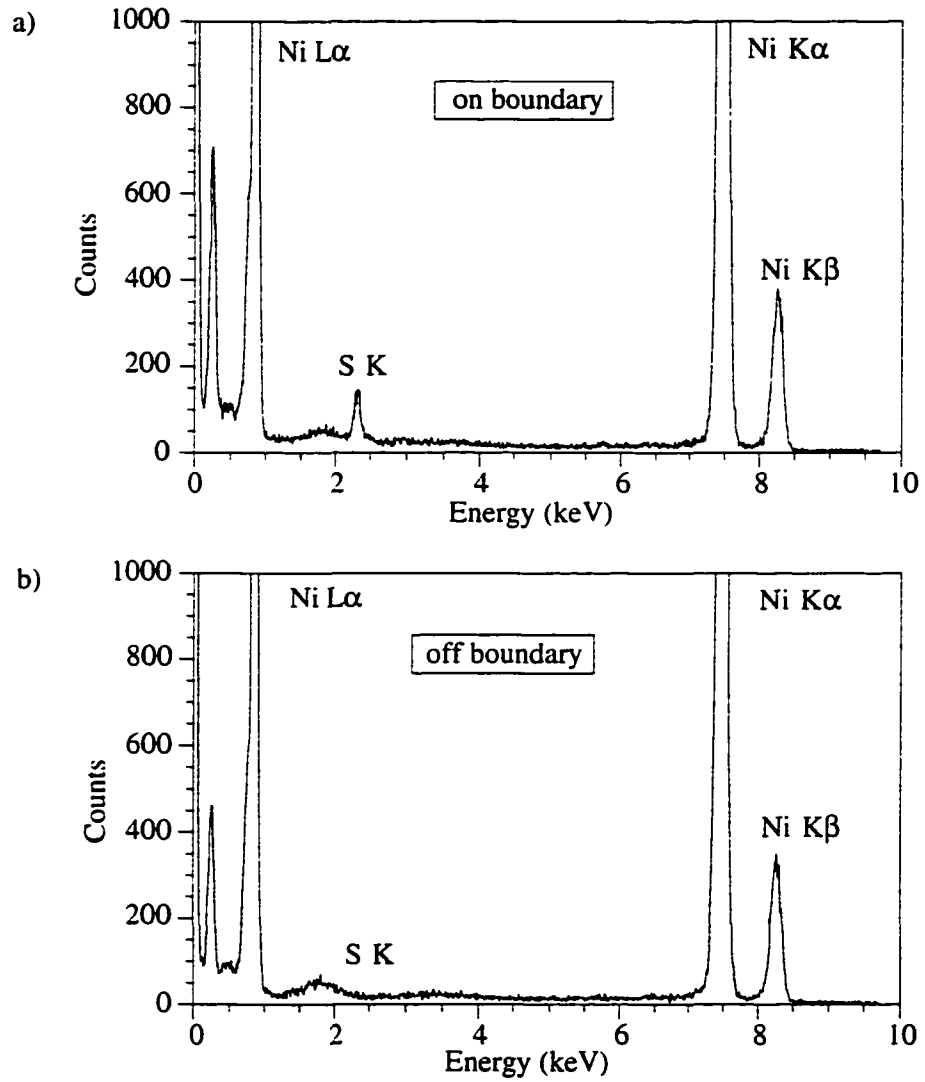


Figure 5.2 X-ray spectra taken with a) the probe placed on a grain boundary in S-doped Ni and b) in the nearby bulk. Segregation of S is clearly observed.

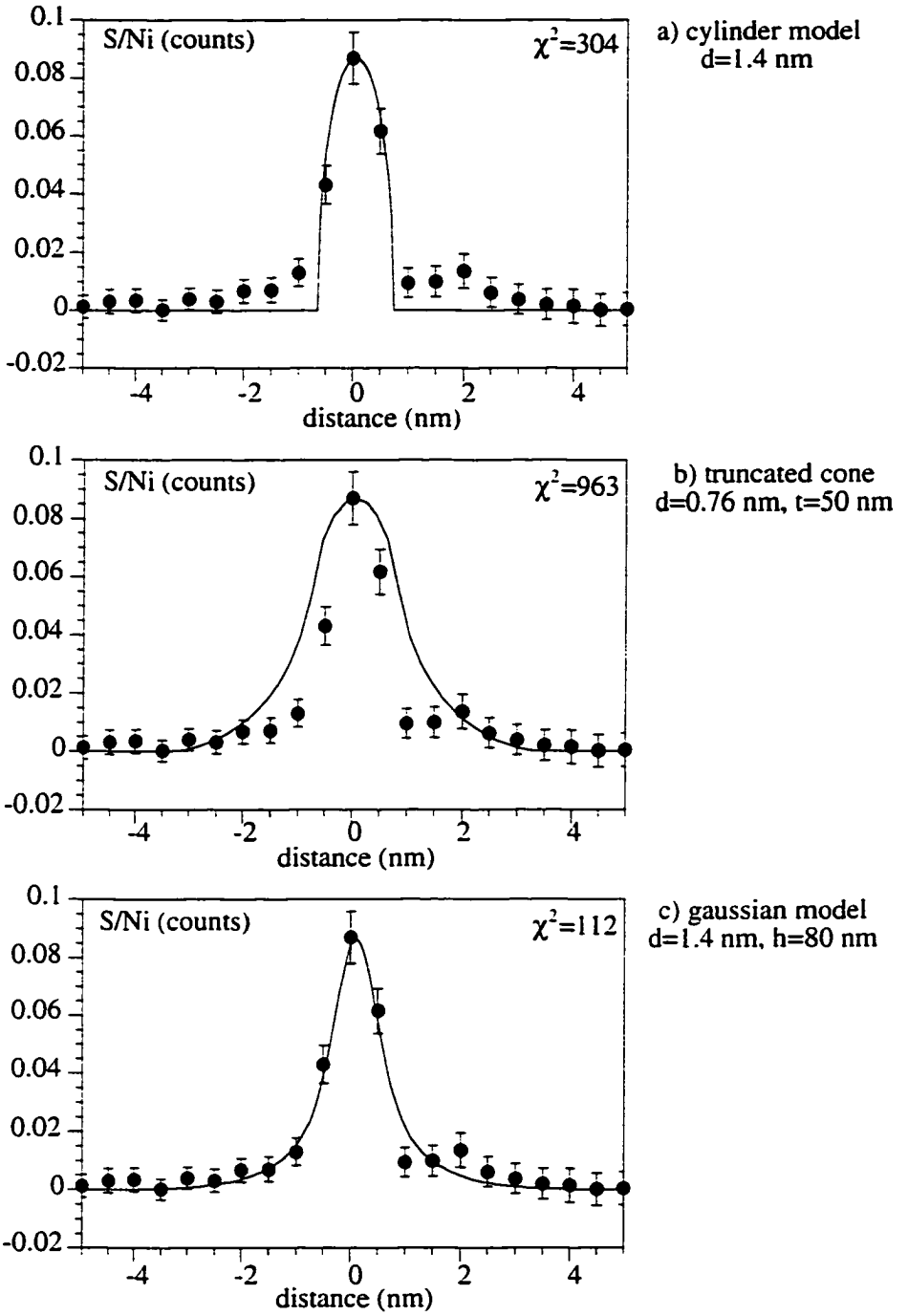


Figure 5.3 Profile of S counts/Ni counts as a function of distance from the grain boundary. Modeled using the different assumptions for interaction volume described in Section 3.1.5.

Goodness of fit described by $\chi^2 = \sum_i ((I_{exp}(x) - I_{model}(x))/\sigma)^2$.

Another grain boundary was chosen for 2D mapping of S segregation. Maps were collected at 1 MX and were 64x64 pixels with a dwell time of 500 ms for each pixel. The 30 μm VOA was used with a probe size of ~1.4 nm. Two maps were collected at two different thicknesses of 100 and 60 nm and are shown in Figure 5.4 and 5.5 respectively. The raw S and Ni maps as well as the compositional maps are given in these figures along with the BF image of the area of boundary mapped. Simulating a raster scan using the map of Figure 5.4 gave a grain boundary coverage of $19.3 \pm 1.6$ atoms/nm$^2$ or $2.3 \pm 0.2$ monolayers.

Profiles were extracted from these maps in the regions indicated and these experimental profiles are shown in Figures 5.5-8 along with a number of theoretical profiles. In this case errors were calculated to be $3\sigma$ where $\sigma$ was the standard deviation of the S/Ni ratio in the regions off the grain boundary. The profile from region B (Figure 5.7) is not symmetric and looking at the comparable region in the BF image, the distinct contrast associated with the top and bottom surfaces of the foil are clearly seen, indicating that the boundary is in inclined to the beam, with a projected width of ~3 nm. In the region from which profile A was extracted, it is not as obvious that boundary inclination is present, and the profile is symmetric. In all of the profiles shown in Figures 5.6-8, the assumption of a planar grain boundary and using the known thickness and probe sizes, poorly models the experimental profiles. As Figure 5.6b shows, increasing thickness of the sample cannot explain this discrepancy. In order to obtain good agreement it must be assumed that the grain boundary has a width of 2 nm or alternatively that the size of the incident electron probe is twice the known value.

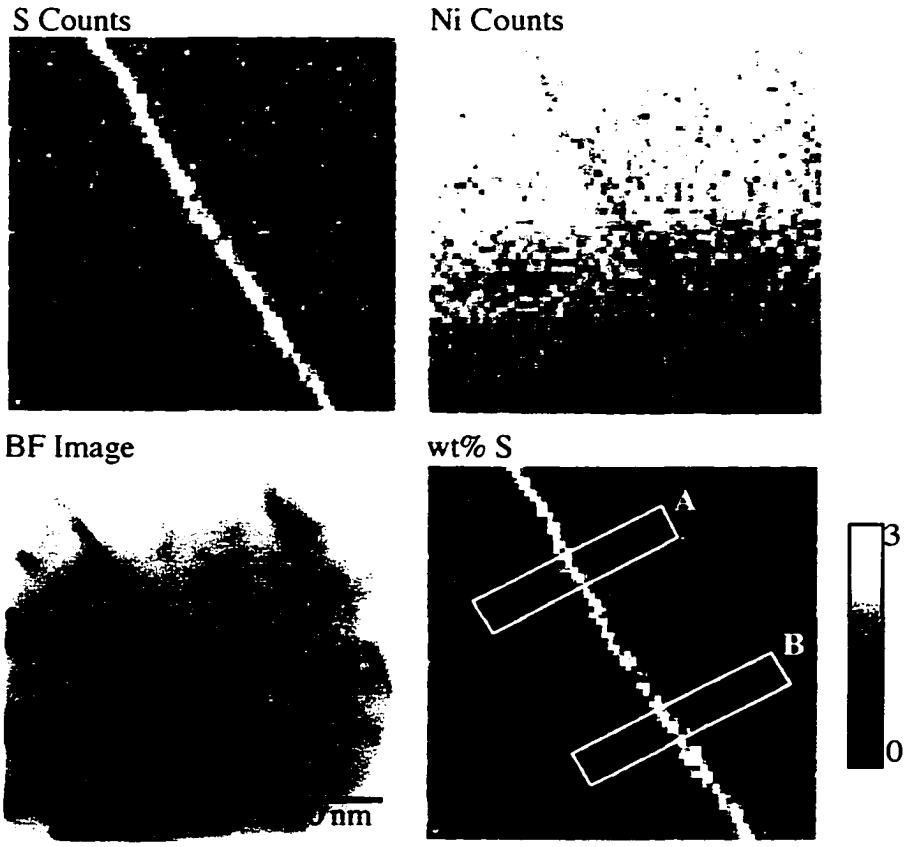


Figure 5.4 2D elemental and compositional X-ray maps from a grain boundary, shown in the BF image, in S-doped Ni. The thickness of the sample was measured using the low loss region of the EEL spectrum to be 100 nm. The segregation profiles extracted from the regions A and B are given, with different theoretical models, in Figures 5.6 and Figure 5.7 respectively.

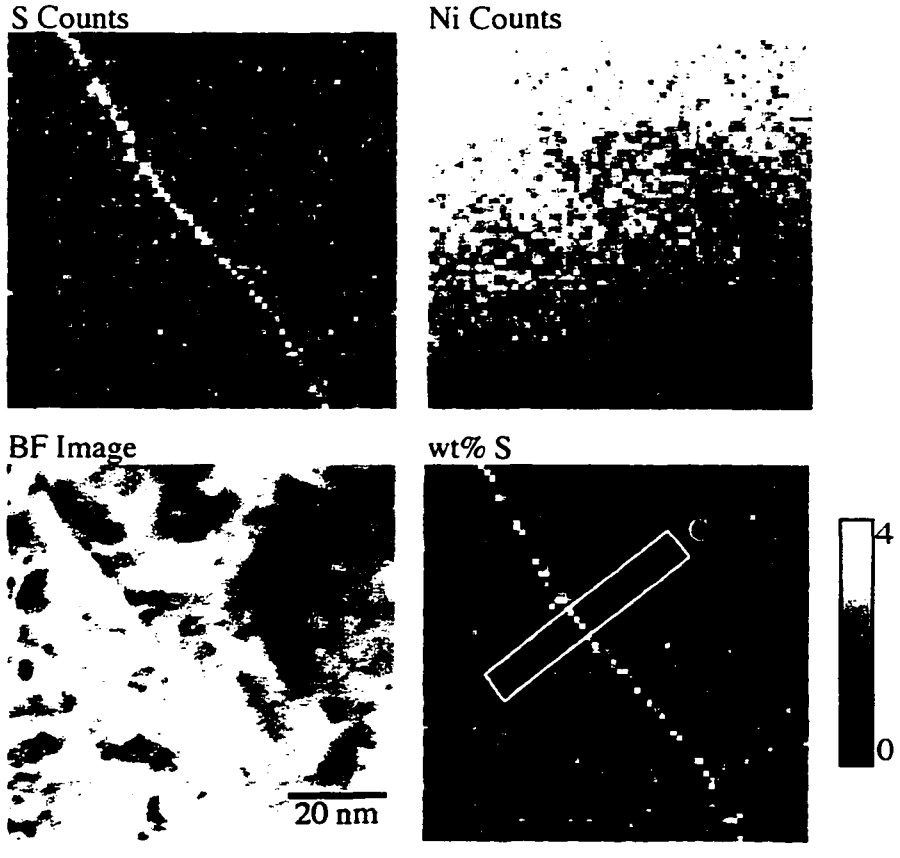


Figure 5.5 2D elemental and compositional X-ray maps from the same grain boundary as Figure 5.4, but in a thinner region. The thickness of the sample in this region was measured using the low loss region of the EEL spectrum to be 60 nm. The segregation profiles extracted from the region shown is given in Figure 5.8 with different theoretical models.

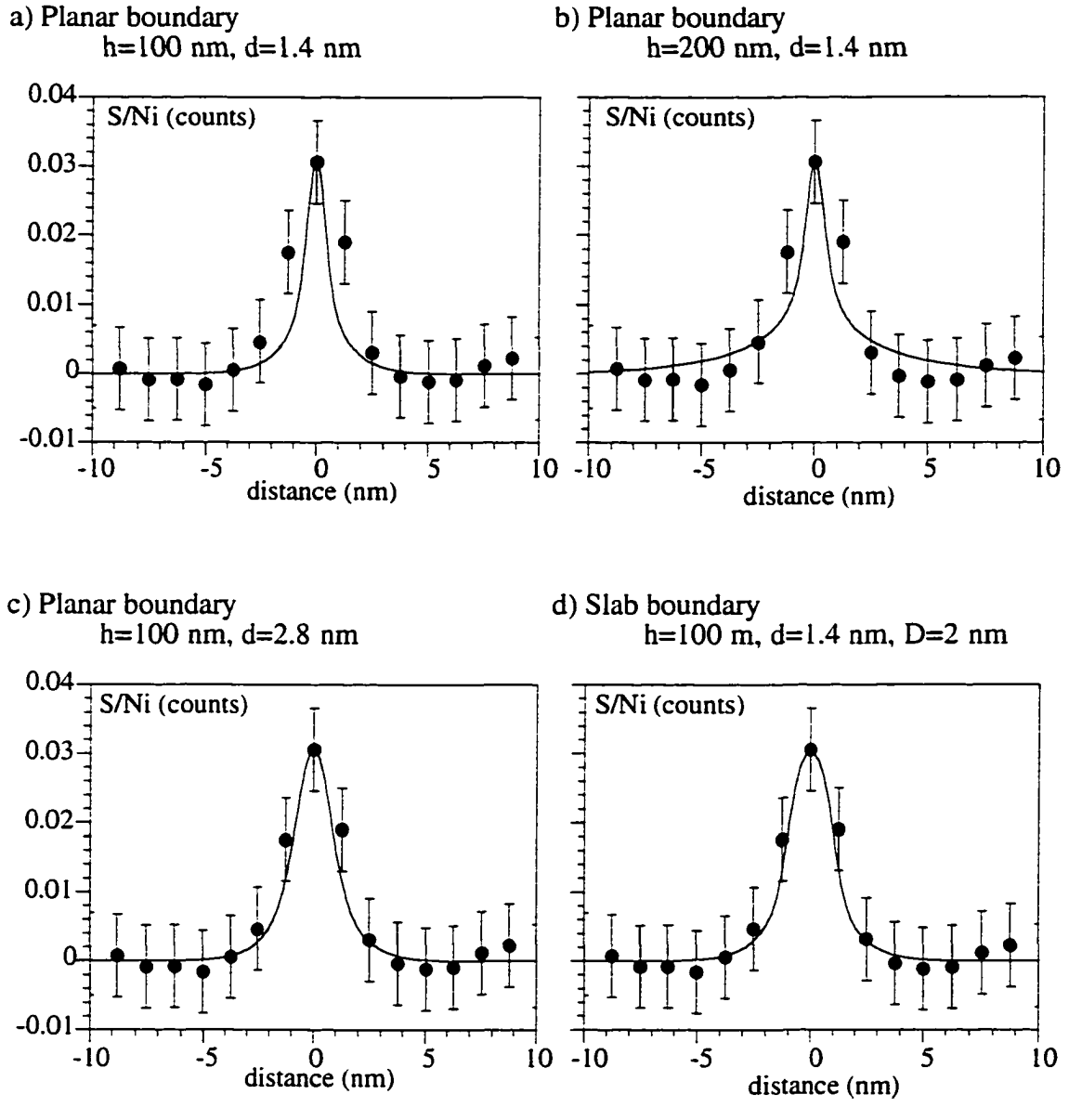


Figure 5.6 Experimental profile of S/Ni counts as a function of distance from a grain boundary. Extracted from region A of Figure 5.4 and shown with different theoretical models.

a) Inclined plane
h=100 nm, d=1.4 nm, W=3 nm

b) Inclined plane
h=100 nm, d= 2.8 nm, W=3 nm

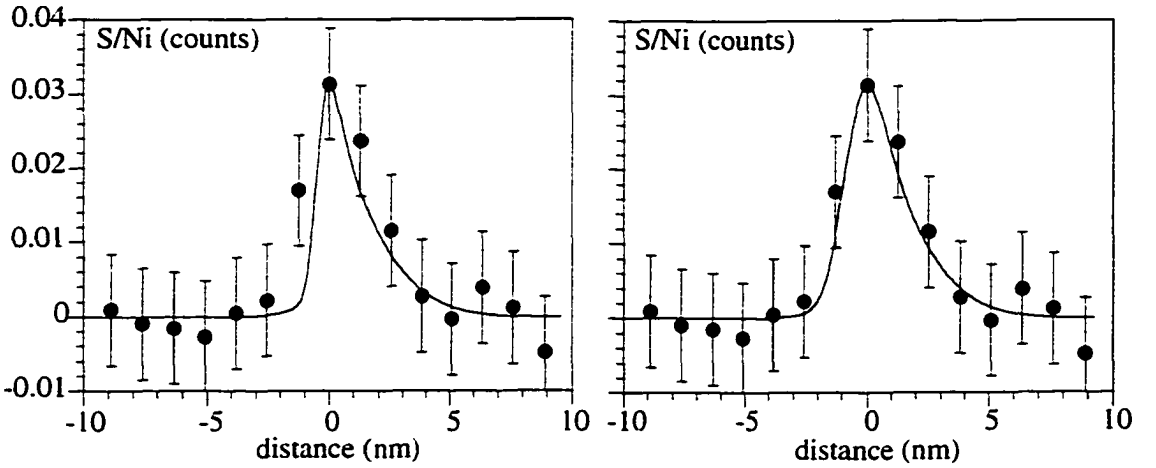


c) Inclined Slab
h=100 nm, d=1.4 nm, W=3 nm. D=2 nm

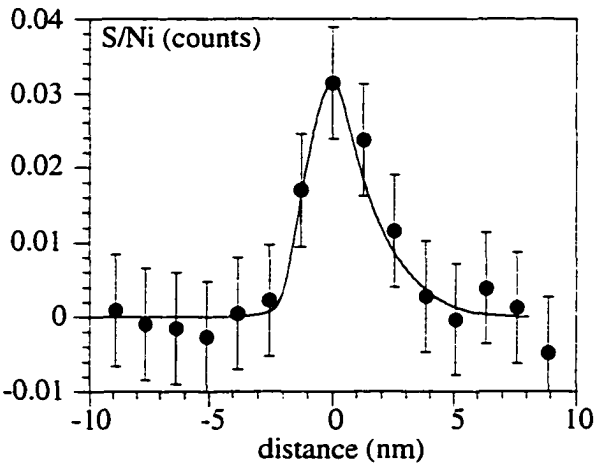


Figure 5.7 Experimental profile of S/Ni counts as a function of distance from an inclined grain boundary. Extracted from region B of Figure 5.4 and shown with different theoretical models.

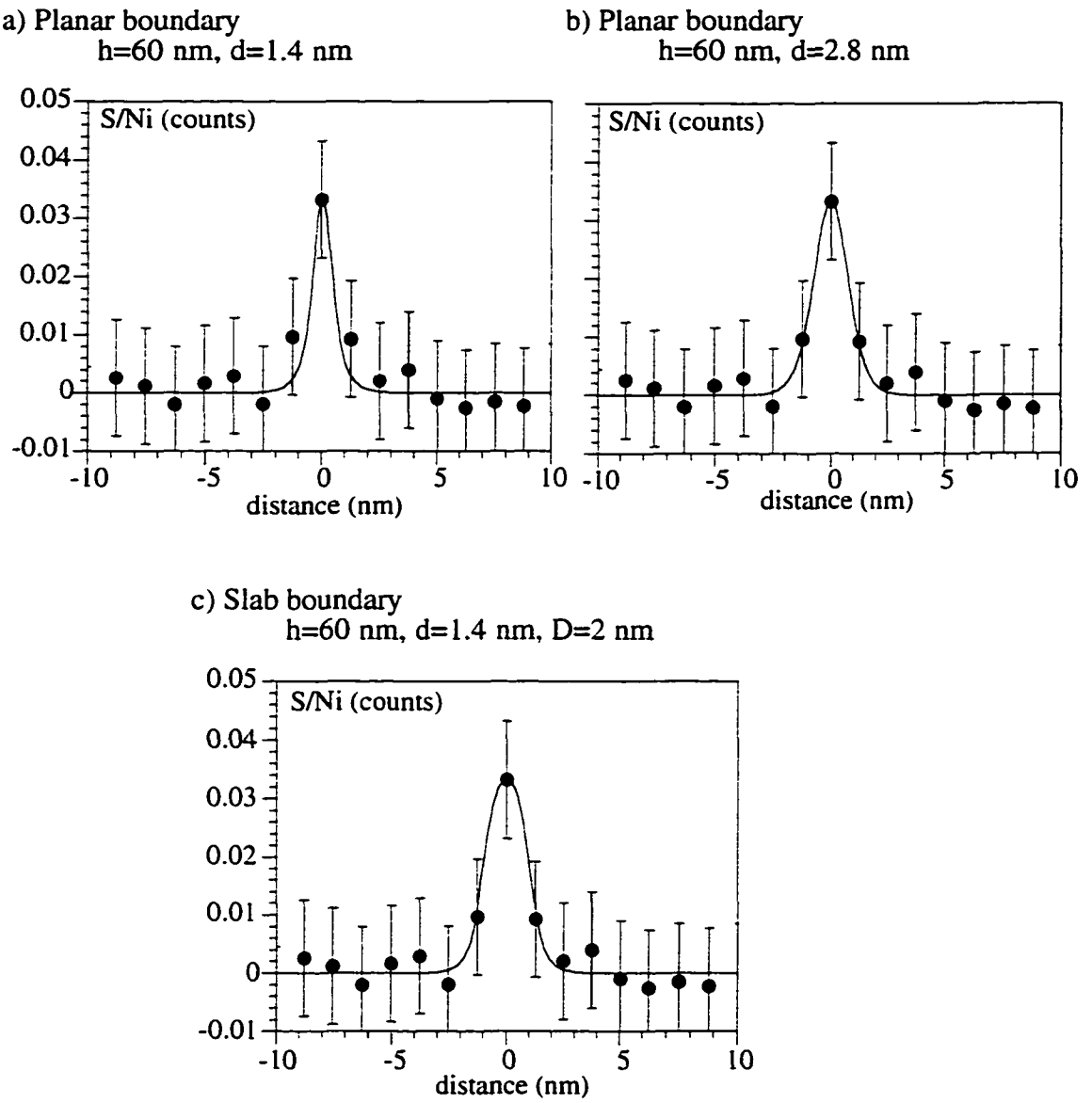


Figure 5.8 Experimental profile of S/Ni counts as a function of distance from a grain boundary. Extracted from region C of Figure 5.5 and shown with different theoretical models.

### *5.1.2 Bi-doped Cu*

#### *5.1.2.1 Application of XEDS - Profiling and Mapping*

It is well established that segregation of Bi occurs to grain boundaries in Cu and Figure 5.9a shows a profile of Bi counts divided by Cu counts as a function of distance from the grain boundary in the BF image of Figure 5.9b. This profile was obtained in previous work Keast et al. (1998) using the 50 μm VOA on the VG 603, has a full width of ~ 4 nm, and is a typical for results from segregation studies (Hall et al. (1981), Titchmarsh (1986)).

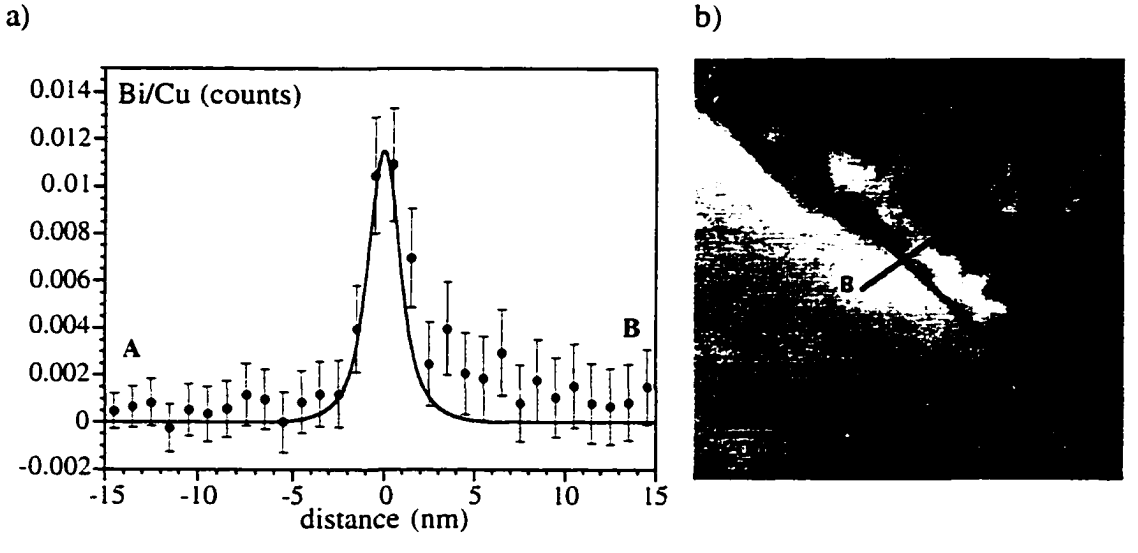


Figure 5.9 a) Segregation profile obtained in previous work (Keast et al. (1998)) of Bi segregation to a Cu grain boundary (BF image shown in 5b). The profile has been modeled using equation 3.28 and with a thickness of 100 nm.

This profile has been modeled using the gaussian model of equation 3.28 and it was assumed that the specimen was 100 nm thick. There is an asymmetry in the profile, which in this case is thought to be due to electron beam damage which was observed when this profile was obtained. Such an asymmetry could also arise from boundary inclination, however the image of the boundary does not show a significant boundary

tilt in the region where the profile was taken. Scaling of the theoretical profile to the experimental profile gave a grain boundary coverage of $\Gamma = 2.9 \pm 0.2$ atoms/nm$^2$ or 0.3 monolayer.

Figure 5.10 shows a 2D map of a faceted grain boundary in the sample provided by D. E. Luzzi. The map of Bi Lα counts is given Figure 5.10b and the simultaneously collected BF electron image is in Figure 5.10a. This map is 64x64 pixels and taken at 1 MX. The 50 μm VOA was used and a dwell time of 500 ms per pixel. The boundary was tilted so as to be parallel to the electron beam, which meant that it was tilted away from the Si detector, and the Ge detector (on the other side of the microscope column) was used instead.

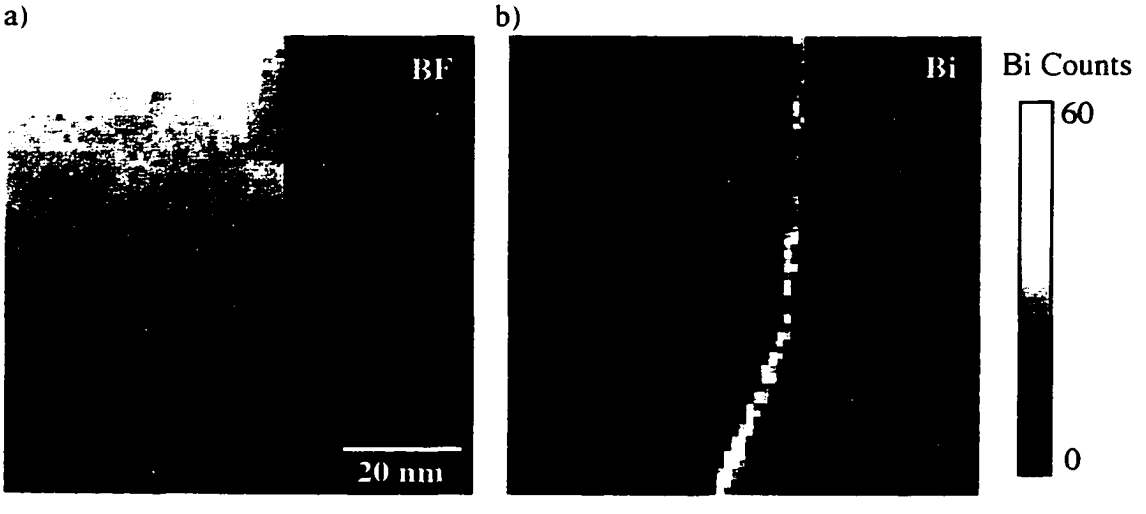


Figure 5.10 a) BF image and b) simultaneously collected map of Bi Lα counts on a faceted grain boundary in the specimen provided by D. E. Luzzi.

There is some indication in this map that the upper facet has a smaller amount of Bi. Separate raster scans (at 5 MX) on these facets gave grain boundary coverages of 10.8±1.1 atoms/nm$^2$ (1.2 monolayers) for the upper facet and 12.8±1.3 atoms/nm$^2$

(1.4 monolayers) for the lower facet. The upper facet shows an area where the Bi signal is smaller and wider and it is believed this is a consequence of electron beam damage because a spot analysis was performed at this point before the map was collected as a preliminary check for Bi segregation.

In the examples of Figures 5.9 and 5.10 shown above, the spatial resolution is relatively poor, on the order of 4 nm, however, the signal at the grain boundary is well above the detectability limits. Therefore it should be possible, using smaller probe sizes and/or thinner specimens to obtain similar information but with better spatial resolution. Figure 5.11 shows a map from another boundary, this time in the sample provided by J. D. Embury. In this case the 30 μm VOA (probe size = 1.4 nm) was used and the map was obtained from a relatively thin area of the specimen. Both Cu, Bi and background maps were collected and the Bi signal is shown in wt%.

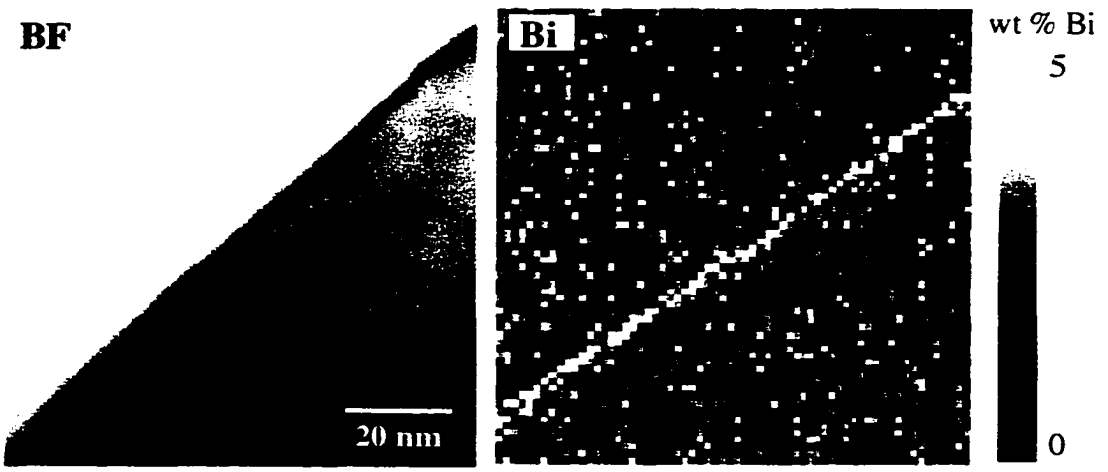


Figure 5.11 Compositional map of Bi content at a grain boundary in the Bi doped specimen provided by J. D. Embury. $\Gamma$=~0.8 atoms/nm$^2$ = 0.09 monolayer.

This map is quite noisy, but there is a significant improvement in spatial resolution, now < 2 nm (each pixel =~1.3 nm). The position of the grain boundary plane is slightly shifted between the image, collected before the map, and the Bi map and this is due to

specimen drift. A profile, showing the ratio of Bi counts to Cu counts, extracted from this map and integrated over a width of 5 pixels, is shown in Figure 5.12. The experimental data is shown with a theoretical profile, modeled using equation 3.28 and assuming a thickness of 60 nm and it appears to fit the experimental data points well. It should be noted that the Bi signal at the grain boundary is only just above the noise.

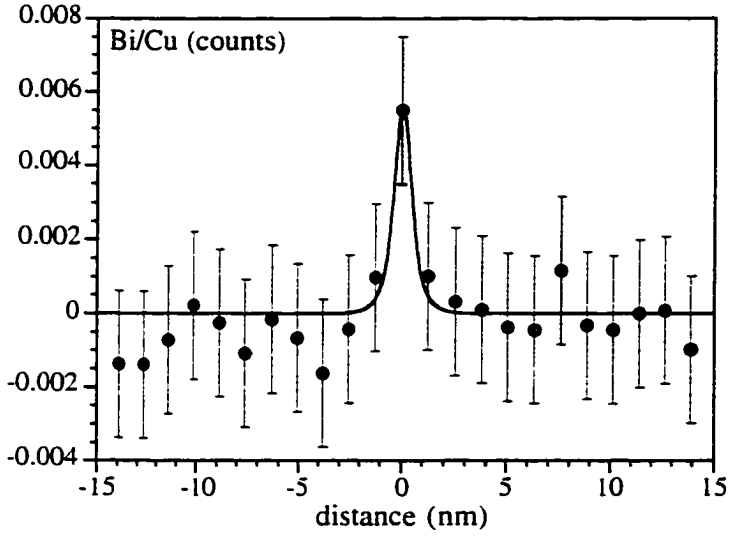


Figure 5.12 Bi segregation profile extracted from the map in Figure 5.11. Experimental points are 1.26 nm apart and the line fit is a model based on equation 3.28 assuming a thickness of 60 nm.

The segregation levels for this boundary were quantified using a number of different approaches. Separate raster scans (at 10 MX) were performed in two different regions of this grain boundary and at different thicknesses. Quantification of spectra collected during these raster scans gave $\Gamma = 0.76 \pm 0.44$ and $0.83 \pm 0.26$ atoms/nm$^2$ (0.8 atoms/nm$^2$ = 0.09 monolayer). Simulating a raster scan using the map of Figure 5.11 gave $\Gamma = 0.81 \pm 0.58$ atoms/nm$^2$ and scaling the theoretical profile to the experimental profile gave $\Gamma = 0.68 \pm 0.3$ atoms/nm$^2$. The agreement between these values is well within experimental error, indicating that the quantification procedures are quite robust.

*5.1.2.2 Σ=3 Grain Boundaries*

Quantitative XEDS was performed on a total of 46 grain boundaries in the material provided by D. E. Luzzi. 20 of these had Σ=3 orientation and 26 were non Σ=3. The measured levels of segregation for these boundaries are shown in Figure 5.13 where the segregation levels have been plotted in the chronological order that the measurements were taken. In nearly all cases grain boundary coverage was obtained using a raster scan. The few grain boundaries that were analyzed in spot mode are indicated by the open symbols in Figure 5.13.

For the spectra obtained in spot mode, quantification was done using the approximation of cylinder with diameter as FWTM of the probe size, which from Figure 3.6 may mean that the measured values are out by as much as factor of two (for sample thicknesses between 50 and 150 nm - a reasonable range). Two grain boundaries displayed anomalously large segregation levels and are excluded from these plots, but will be discussed in more detail in Section 5.1.2.3. In a couple of cases measurements were made on the same grain boundary facet but under different conditions (i.e. thickness, raster size) and agreed within experimental error. Measurements for the same grain boundary but at different facets did not always agree within experimental error. With the exception of incoherent facets of a Σ=3 boundary, which was itself a result of disassociation of a Σ=9 boundary (to be described below), there is no detectable segregation at Σ=3 grain boundaries. Nearly all non Σ=3 grain boundaries had detectable levels of segregation.

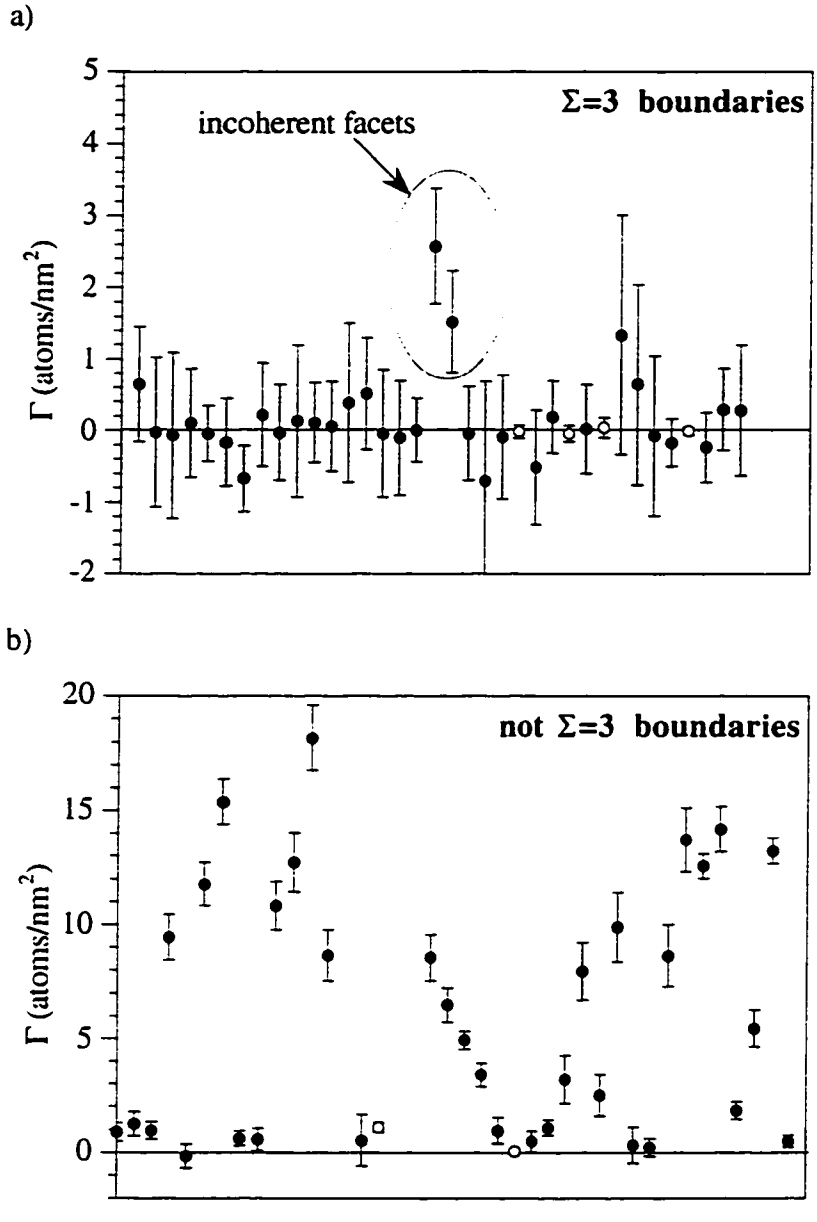


Figure 5.13 Segregation levels in atoms/nm$^2$ for a) Σ=3 and b) non Σ=3 boundaries in the samples provided by D. E. Luzzi. The shaded region corresponds to an equal range of values (-1 to 1) in both a) and b).

Figure 5.14a shows a BF image of a Σ=9 grain boundary that had disassociated into two Σ=3 grain boundaries and a schematic for this boundary is given in Figure 5.14c. In the compositional map showing Bi concentration in Figure 5.14b it can be seen that significant segregation occurs to the Σ=9 section of the grain boundary and a small amount of segregation occurs at the incoherent Σ=3 facets (those circled in Figure 5.5a). Interestingly, incoherent facets form both of the long sections of the disassociated grain boundary as opposed to one coherent facet and one incoherent facet as is usually seen (Clarebrough and Forwood (1980), Forwood and Clarebrough (1984)). It is possible that the presence of the Bi stabilizes the incoherent facets.

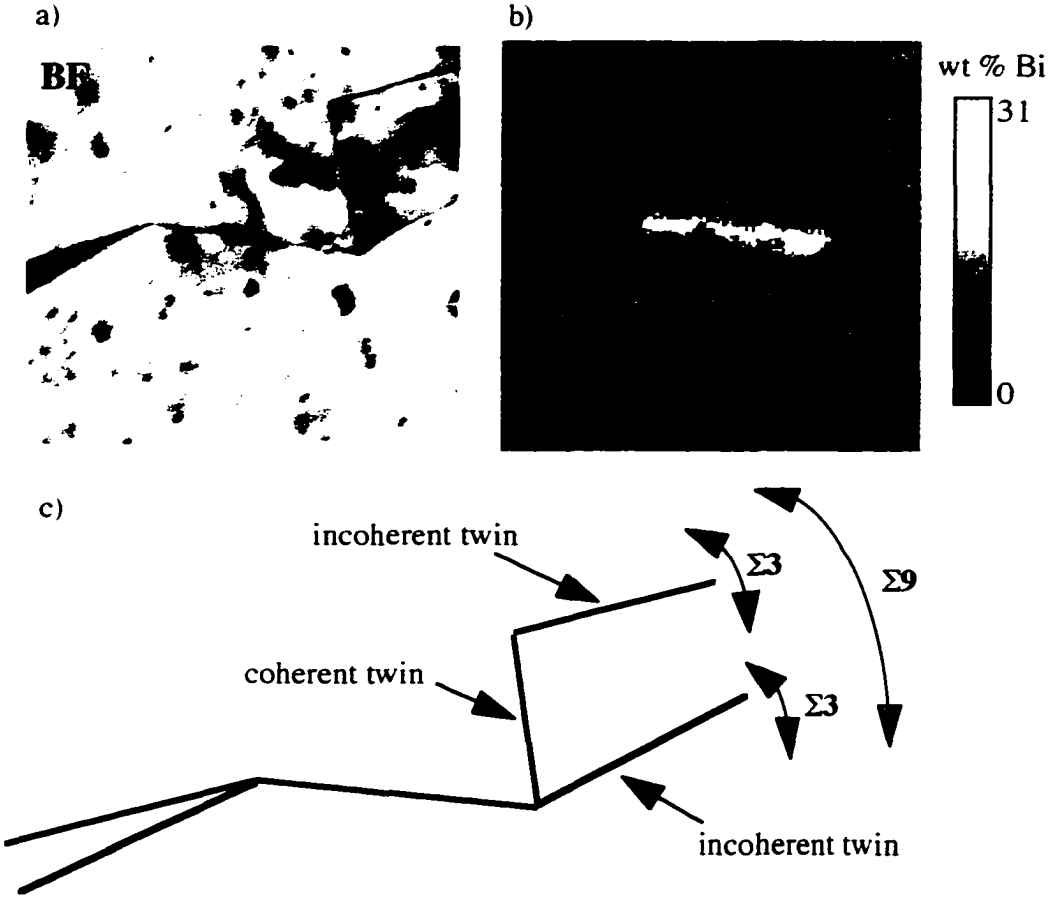


Figure 5.14 Disassociated Σ=9 grain boundary into Σ=3 boundaries, showing large Bi segregation only to a small section of Σ=9 remaining.

In the Σ=3 bicrystals provided by the Max-Planck-Institut, the grain boundaries were almost perfectly parallel to the electron beam and spot analyses were used to maximize detection sensitivity. The results of this analysis are shown in Table 5.1. Quantification using both the cylinder approximation and the full gaussian calculation (assuming a worst case of 150 nm thickness) are shown. Within experimental error, there is no detectable Bi either at these Σ=3 grain boundaries or in the bulk. The nominal bulk concentration of Bi (100 wt ppm) is well below the detectability limit for these measurements (~0.5 wt %).

Table 5.1. Bi content in a Σ=3 bicrystal

| | Bi/Cu (counts) ($x10^{-3}$) | Γ (atoms/$nm^2$) cylinder approximation | Γ (atoms/$nm^2$) full calculation |
|---|---|---|---|
| boundary | -0.50±1.4 | -0.06±0.15 | -0.12±0.32 |
| boundary | -0.16±0.8 | -0.02±0.09 | -0.04±0.18 |
| boundary | 0.45±1.0 | 0.05±0.11 | 0.11±0.23 |
| | | Concentration (wt%) | |
| bulk | -0.48±1.5 | -0.2±0.6 | |
| bulk | 0.20±0.8 | 0.08±0.3 | |

Although equilibrium segregation was not observed in Σ=3 bicrystals, precipitates on the grain boundary were observed and found to contain Bi. Figure 5.15 shows a BF image and an RGB image obtained from a set of elemental maps, where red = Al, blue = Si and green = Bi. It appears that a smaller precipitate, containing Al (or alumina) surrounded by Si (or silica), has been the nucleation site for a larger Bi precipitate. The smaller precipitate also contained O. A precipitate containing Bi was observed at one of the Σ=3 boundaries in the polycrystalline sample discussed above, but a detailed analysis was not performed.


Figure 5.15 a) BF image and b) RGB image of a precipitate on a grain boundary of a Bi doped Σ=3 {111}/{111} bicrystal.

*5.1.2.3 Inhomogeneities and Anomalous Segregation Levels*

As mentioned previously, a couple of grain boundaries showed anomalously large segregation levels and Figure 5.16 shows a BF image, ADF image and elemental maps from such a grain boundary. In addition to the large Bi segregation levels a large deficit in the Cu signal is seen at the grain boundary. The segregation level to this grain boundary was found to be 74±8 atoms/nm$^2$ or 8.0±0.8 monolayers. Another measurement on a different day gave 46±3 atoms/nm$^2$ or 5.0±0.3 monolayers. These values are well in excess of the maximum values of 1-2 monolayers normally observed. Further analysis using EELS revealed that there was also significant O at this boundary. Figure 5.17a shows EEL spectra, taken in 2nd difference mode (Shuman and Somylo (1987)), clearly indicating excess O at the grain boundary. However, after a brief cleaning in the PIPS, it was no longer obvious that excess O was present at the grain boundary (Figure 5.17b) although a residual, presumably surface oxide is still present. It is likely that the large levels of Bi segregation observed with XEDS are actually due to an accumulation of Bi on the surface of the foils at the location of the grain boundary,

perhaps in some Bi-Cu-O phase. The Cu $L_{23}$ ionization edge showed a distinct white line at this grain boundary.

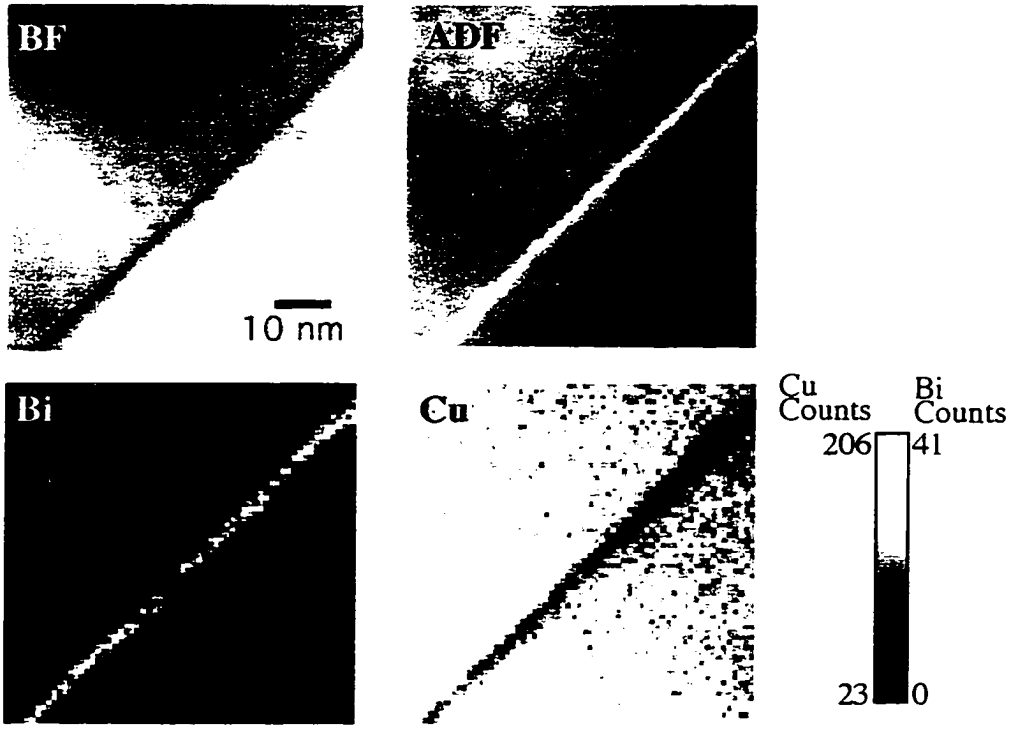


Figure 5.16 BF, ADF images and Cu and Bi maps of a grain boundary containing unusually large levels of Bi.

There is some indication in Figure 5.16 that there are inhomogeneities in the Bi content along the grain boundary and these were also observed in another boundary. Similar inhomogeneities were observed at one grain boundary in the specimen provided J. D. Embury and this is shown in the Bi map of Figure 5.18. The Cu map, however, does not obviously show these inhomogeneities although a large grain boundary deficiency is observed. For this boundary, quantification of spectra obtained from a raster scan gave a segregation levels of 4.6 ±0 .3 atoms/nm$^2$, which is not unusually large.

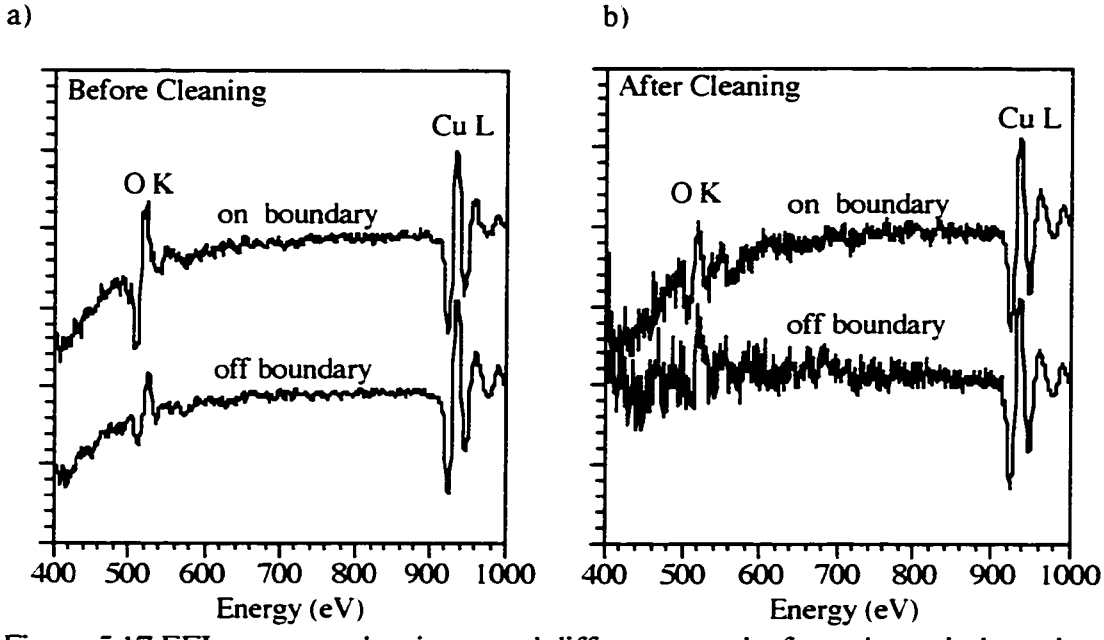


Figure 5.17 EEL spectra, taken in second difference mode, from the grain boundary of Figure 5.16, containing unusually large segregation levels. a) excess of O is observed at the grain boundary b) but is not obvious after cleaning in the PIPS.

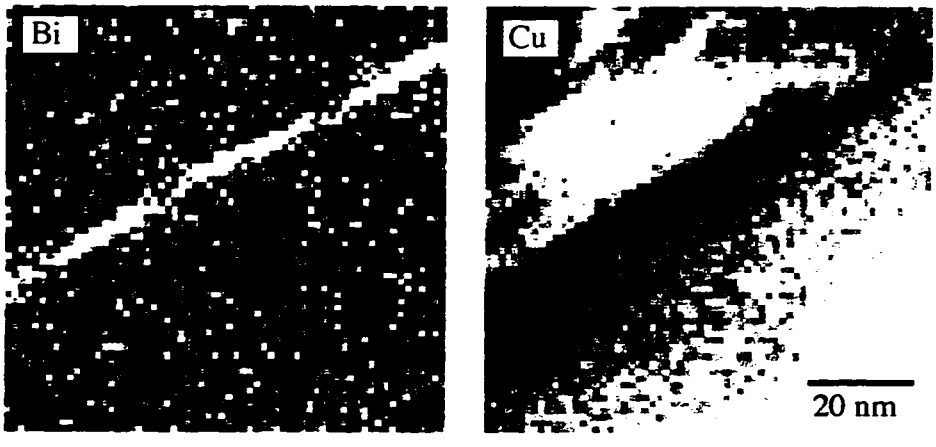


Figure 5.18 Bi and Cu maps of a grain boundary in the sample provided by J. D. Embury, indicating inhomogeneities in the Bi level along the grain boundary.

A lower magnification map in a slightly thicker area of the same boundary is shown in Figure 5.19. The boundary is inclined to the incident beam and shows excess Bi where the boundary intersects with the surface of the foil. An indication of O is also seen in these areas. This suggests that inhomogeneities in the Bi levels are most likely due to inhomogeneities in the surface accumulation of Bi. A precipitate containing Cr was also observed at this grain boundary.

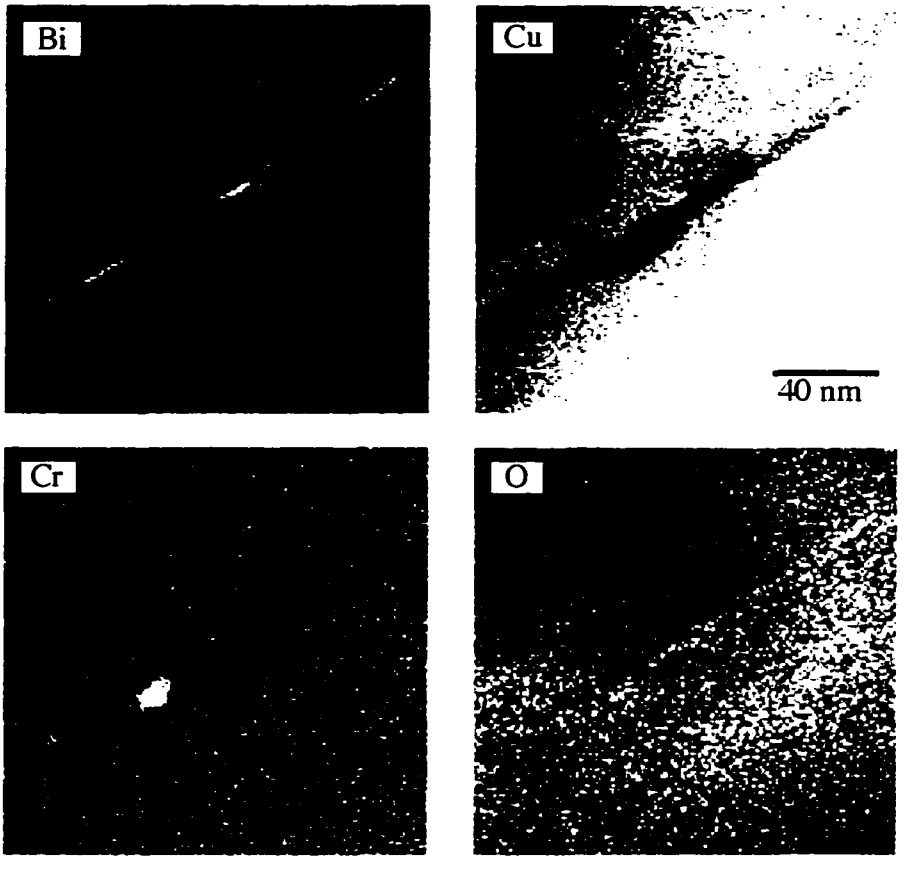


Figure 5.19 Elemental maps from the same boundary of Figure 5.18 but in a slightly thicker region. Excess Bi, and possibly O, is seen where the grain boundary intersects with the foil surface. The boundary also contains a Cr precipitate.

### *5.1.3 Sb-doped Cu*

Preliminary examination of Cu-Sb grain boundaries suggested that Sb is present, although not in particularly large quantities. To increase detection sensitivity, spot mode was used and Figure 5.20 shows X-ray spectra obtained when the electron probe was placed both on and off the grain boundary. Segregation of Sb is clearly seen. If we assume the thickness is between 50 and 150 nm then the segregation level is found to be $1.3 < \Gamma < 2.6$ atoms/nm$^2$, or 0.074 < monolayers < 0.15 . If instead we express this as wt % in a 0.5 nm wide slab at the grain boundary then 3.0 wt% $< C_{gb} <$ 6.0 wt%, which is a little low but not inconsistent with values of around 5-15 % in the literature (Chuang et al. (1982), Yu et al. (1983), Bokshteyn et al. (1991)).

A profile of Sb concentration was obtained from this grain boundary and is given in Figure 5.21, and shows the excess Sb at the boundary. The apparently larger Sb concentration on the right hand side of the profile is believed to be due to electron beam damage, as the beam was stepped from left to right and a substantial "damage track" was seen on the sample after the profile was complete. Beam damage is also believed to contribute to the relatively poor spatial resolution for this profile, as is specimen drift.

Mapping of Sb was performed on one grain boundary and the resultant map of Sb counts is shown in Figure 5.22 along with the simultaneously collected ADF image. The excess Sb at the boundary is only just visible above the noise.

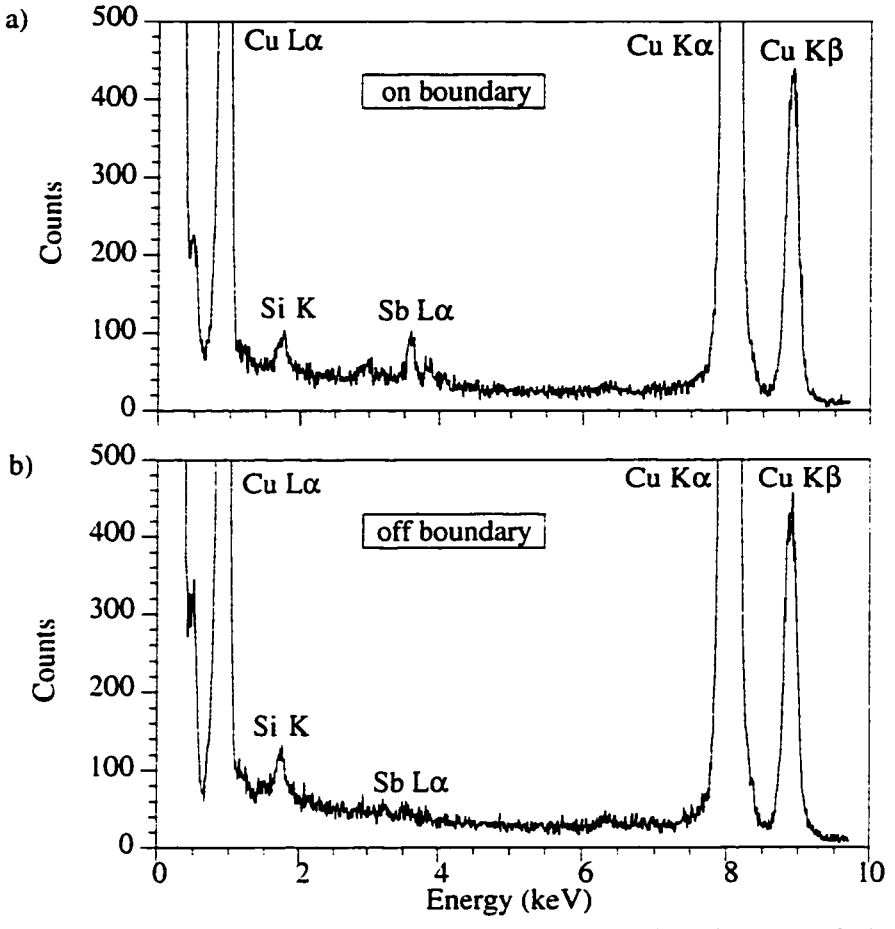


Figure 5.20 X-ray spectra taken with a) the probe placed on a grain boundary in Sb-doped Cu and b) in the nearby bulk. Segregation of Sb is clearly observed.

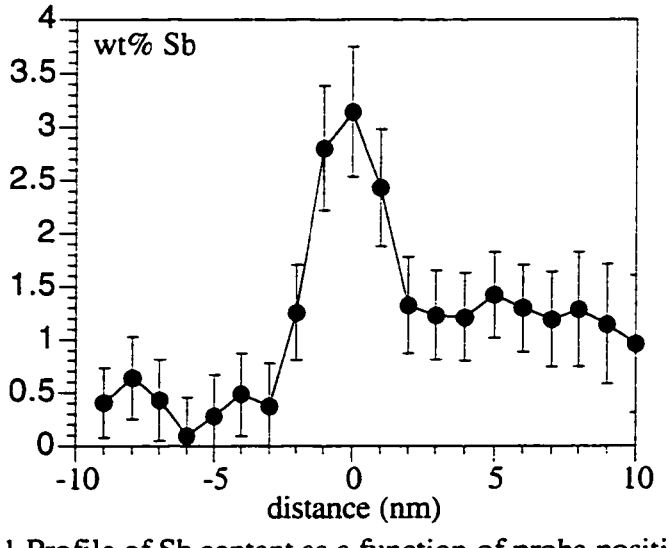


Figure 5.21 Profile of Sb content as a function of probe position from the grain boundary in Sb-doped Cu.

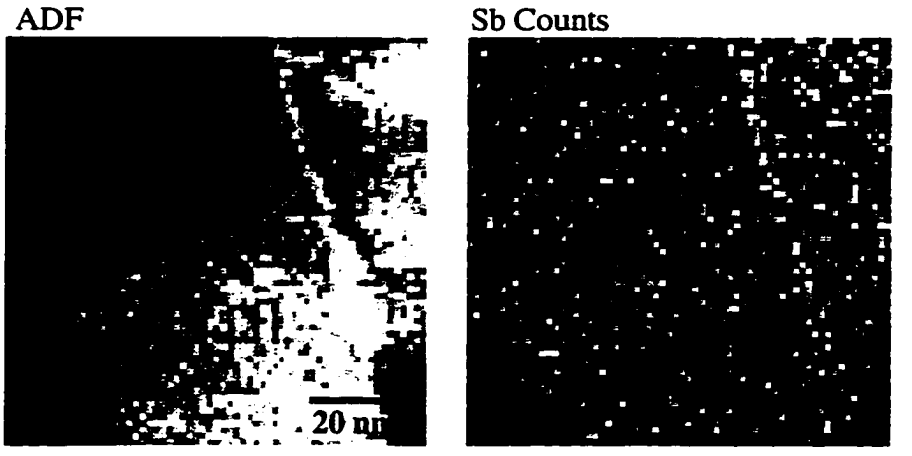


Figure 5.22 ADF image of a grain boundary in Sb-doped Cu along with Sb map. Segregation of Sb is just visible.

As part of the ELNES experiments described in Section 5.2.2, a number of grain boundaries in one Sb doped Cu sample were examined for Sb segregation and the results are summarized in Table 5.2. The quantitative segregation levels were obtained using the cylindrical approximation equation 3.15 and so the actual segregation levels may be underestimated by as much as a factor of two (cf. Figure 3.6), even though the errors given in the table, based on counting statistics, are smaller than this.

Not all boundaries examined had detectable levels of segregation, boundaries number 3C, 6 and 8 for example. Diffraction analysis was not performed and therefore it is possible that these are twin boundaries, at which we would not expect to see segregation. Surprisingly, the largest segregation level was measured at a low angle grain boundary. Numerous voids were observed in this sample, both in the bulk and at the grain boundaries. The interior of these voids were generally faceted. It is not known why these voids form and it may be related to changes in surface energy due to Sb, however further investigation was beyond the scope of this work.

Table 5.2 Segregation levels for 10 different boundaries in Sb doped Cu.

| | Sb/Cu (counts) x$10^{-2}$ | Γ (atoms/$nm^2$) |
|---|---|---|
| boundary 1 | 1.04 | 1.04±0.27 |
| boundary 2 | 0.68 | 0.68±0.18 |
| boundary 3B | 1.21 | 1.22±0.27 |
| boundary 3C1 | 0.0 | 0.0±0.11 |
| boundary 3C2 | 0.0 | 0.0±0.09 |
| low angle boundary | 1.27 | 1.28±0.43 |
| boundary 4 | 0.55 | 0.56±0.15 |
| boundary 5 | 0.73 | 0.74±0.22 |
| boundary 6 | 0.17 | 0.17±0.23 |
| boundary 7 | 0.92 | 0.93±0.21 |
| boundary 8 | 0.16 | 0.16±0.23 |
| boundary 9 | 1.08 | 1.09±0.25 |

*5.1.4 Ag-doped Cu*

Ag was relatively readily detected at the grain boundaries in Ag-doped Cu material. Figure 5.23 shows a comparison of X-ray spectra acquired while the probe was placed on and off a grain boundary. The acquisition time for this spectrum was 20 s and was collected while the beam was rastered at 10 MX. Figure 5.24 shows the EEL spectra collected simultaneously with the X-ray spectra of Figure 5.23. While the Ag elemental peak is easily visible with XEDS, the Ag M EEL ionization edge is not observed, primarily because the Ag signal is spread over a large energy range, reducing visibility. There is a detectable amount of Ag within the bulk, 0.6 ± 0.3 wt%. The excess Ag at this grain boundary was found to be 4.0 ± 1.0 atoms/$nm^2$ (0.26 monolayer).

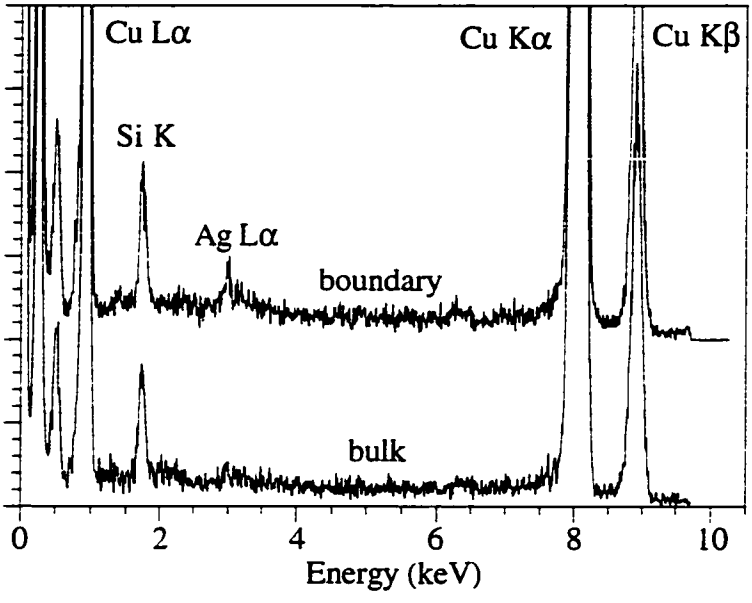


Figure 5.23 X-ray spectra acquired while rastering at 10 MX both on a grain boundary and in the adjacent bulk. Segregation of Ag is observed. A simultaneously acquired EELS spectrum is given in Figure 5.24.

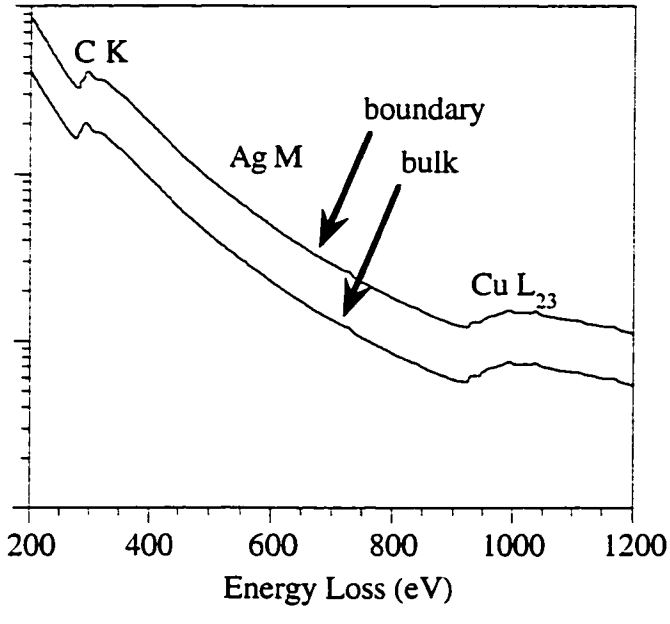


Figure 5.24 EEL spectra collected simultaneously with the X-ray spectra of Figure 5.23. The Ag M edge is not visible.

Figure 5.25 shows a profile of Ag content as a function of distance from this same grain boundary and Figure 5.26b shows an Ag elemental map from a region of this grain boundary, also shown in the BF image of 5.26a. The segregation width is relatively narrow although larger than would be theoretically predicted based on the interaction volume and is not inconsistent with the resolution degradation expected from experimental factors such as specimen drift, contamination, boundary inclination and electron beam damage.

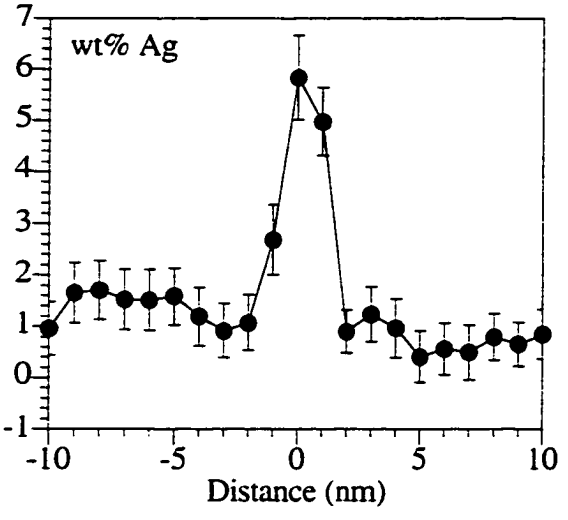


Figure 5.25 A profile of Ag content as a function of distance from a grain boundary

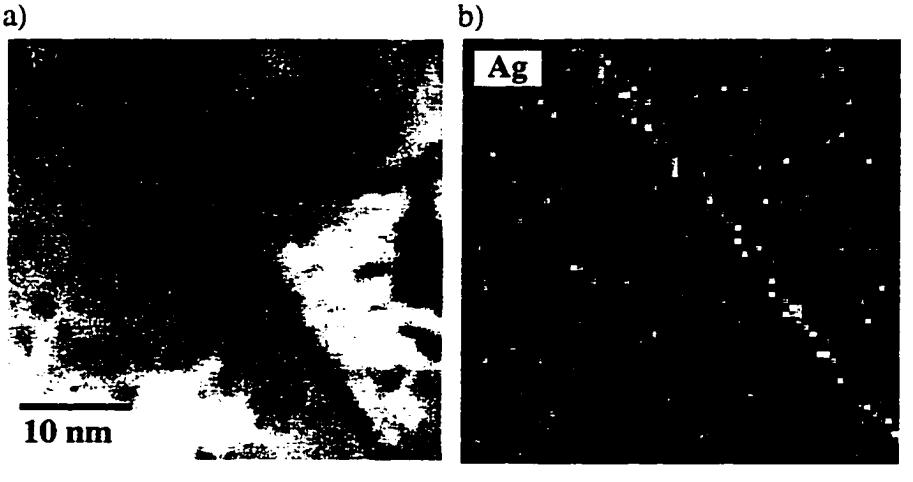


Figure 5.26 a) BF image and b) elemental map of Ag segregation to a grain boundary in Ag-doped Cu.

## 5.2 ELNES

### *5.2.1 S-doped Ni*

Before presenting ELNES results obtained from grain boundaries in S-doped Ni, the importance of eliminating the effects of specimen thickness will be illustrated. Figure 5.27a shows Ni $L_{23}$ edges collected from two different regions within a Ni grain, where the only difference between the two regions is a difference in thickness. When the edges are scaled to match at energies far above ionization threshold, the spectrum taken from the thinner region (thickness = 41 nm) has an apparently larger white line than the thicker region (thickness = 52 nm). When deconvolution of the low-loss spectrum is performed to remove plural scattering, the spectra, shown in Figure 3.27b are indistinguishable.

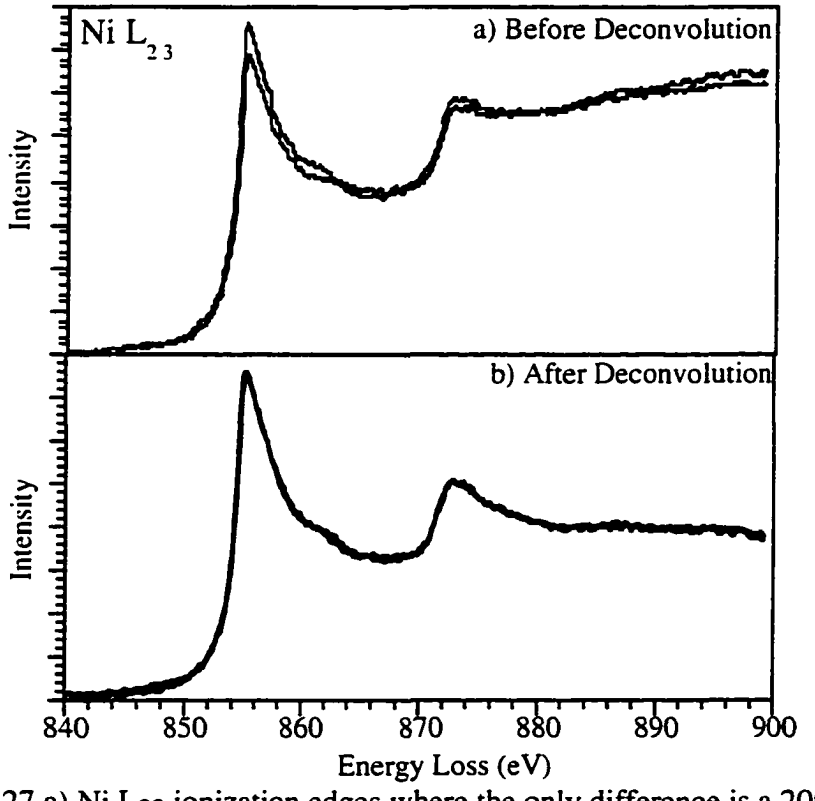


Figure 5.27 a) Ni $L_{23}$ ionization edges where the only difference is a 20% difference in thickness. A decrease in thickness increases the apparent white-line intensity. b)

Deconvolution of the low loss spectrum to remove plural scattering renders the spectra indistinguishable.

This demonstrates that although the effect of thickness can be removed, it must be certain that the low-loss spectrum used to do this truly represents the specimen thickness. If not, the deconvolution procedure itself could artificially introduce a white line into the spectra. Therefore, contamination is very undesirable as it will alter the apparent thickness of the sample as spectra are collected.

Figure 3.28 shows two Ni $L_{23}$ ionization edges where one spectrum was obtained with the electron probe placed on the grain boundary and the other in the adjacent grain (within 10 nm of the boundary). The difference in thickness between these two areas was measured to be less than 3% and contamination was not observed during spectral acquisition. An increase in white line intensity is observed at the grain boundary.

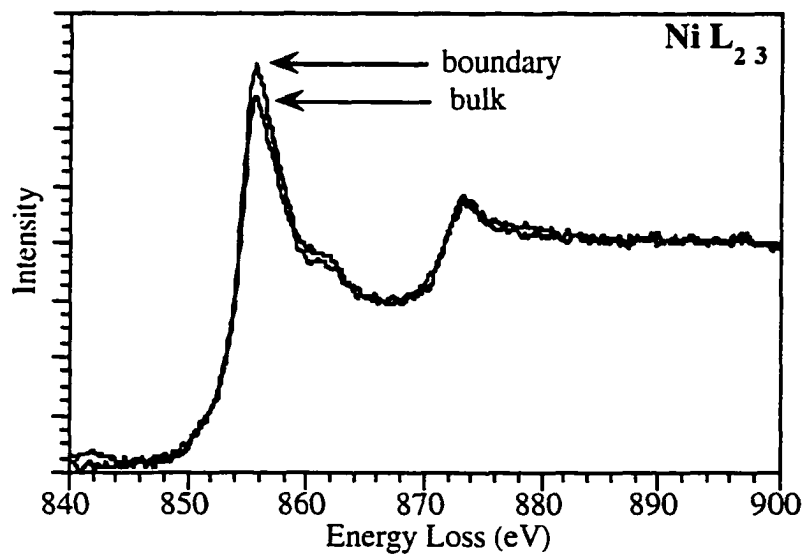


Figure 5.28 Ni $L_{23}$ ionization edges obtained with electron probe placed on the grain boundary and in the nearby bulk. An increase in white line intensity is observed at the grain boundary.

*5.2.2 Sb-doped Cu*

Figure 3.29 shows a BF image of a grain boundary in Sb-doped Cu and Figure 3.30 shows the Cu $L_{23}$ ionization edges obtained from this grain boundary and from within the nearby grain. This boundary is boundary 7 of Table 5.2 and does contain Sb.

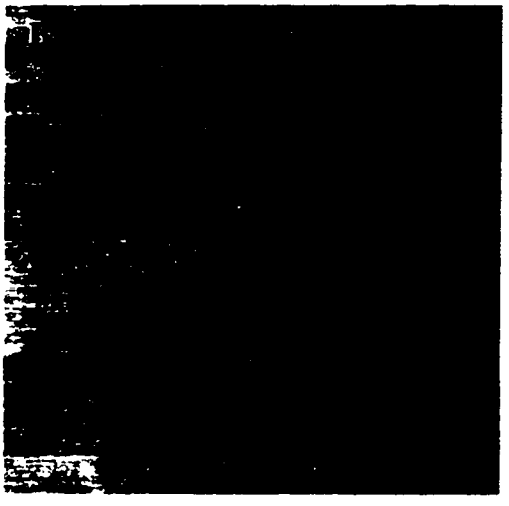

Figure 5.29 BF image of a grain boundary in Sb doped Cu from which the ELNES spectra shown in Figure 5.30 were obtained.

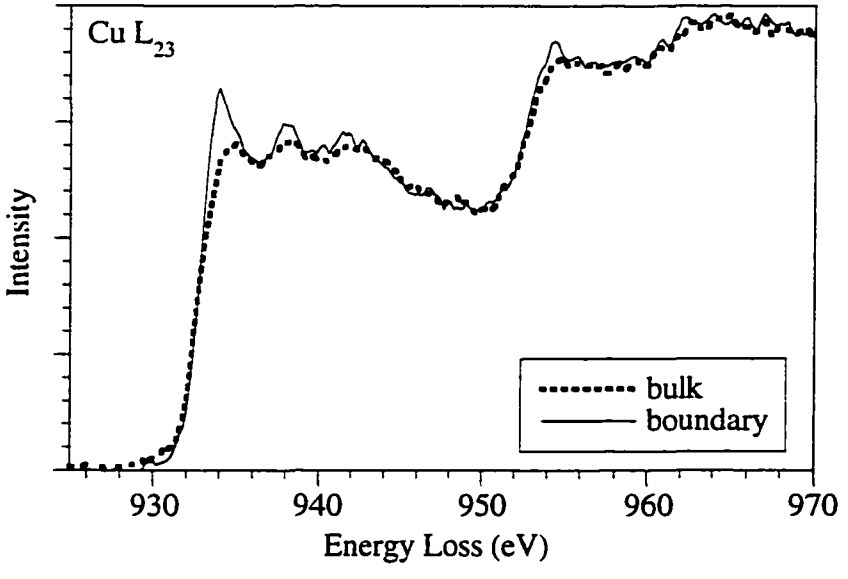


Figure 5.30 Cu $L_{23}$ edges from a grain boundary containing Sb and from within the nearby bulk. An increase in white line intensity at the grain boundary is observed.

An increase of intensity just above the edge onset is observed at the grain boundary, relative to the bulk spectrum. It should be noted that all of the grain boundaries in Table 5.2 were examined with EELS (with the exception of the low angle grain boundary which was not aligned parallel to the beam). Boundary 7 was the only boundary in which such a change in the fine structure was observed. Often analysis was limited by energy drift, specimen drift and/or contamination and so it cannot be absolutely stated that there is no change in fine structure at the other grain boundaries, but rather that we were unable to detect changes at these other boundaries.

Unlike in Ni, the effect of thickness on the Cu $L_{23}$ edges is easily distinguished from the effect observed in Figure 3.30. Figure 5.31 shows Cu L23 ionization edges from regions of differing thickness (50 and 62 nm). When scaled to match at regions far above the ionization edge the difference in intensity extends for nearly 50 eV above the edge threshold.

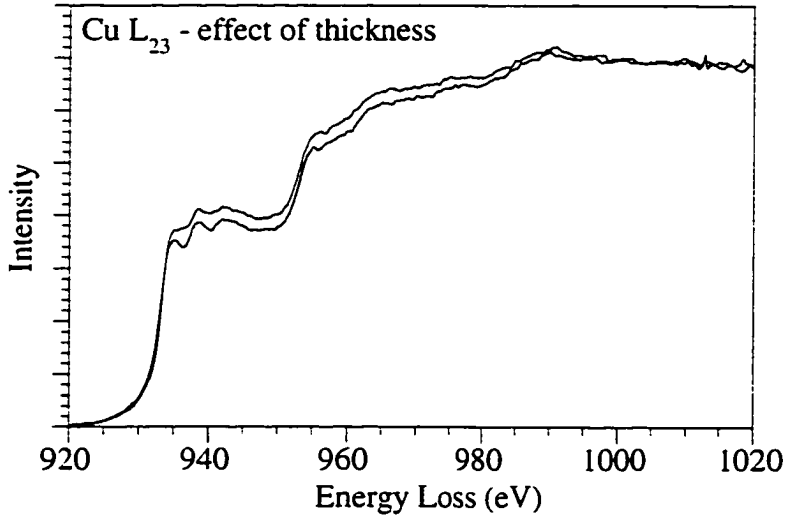


Figure 5.31 Effect of thickness on the shape of the Cu $L_{23}$ edges.

### *5.2.3 Ag-doped Cu*

In the Ag-doped Cu sample no changes in the ELNES were observed at any of the grain boundaries examined. Figure 5.32 shows a typical example of spectra acquired on a grain boundary in this material and from the nearby grain. There are no significant differences in the fine structure between the grain boundary and the bulk.

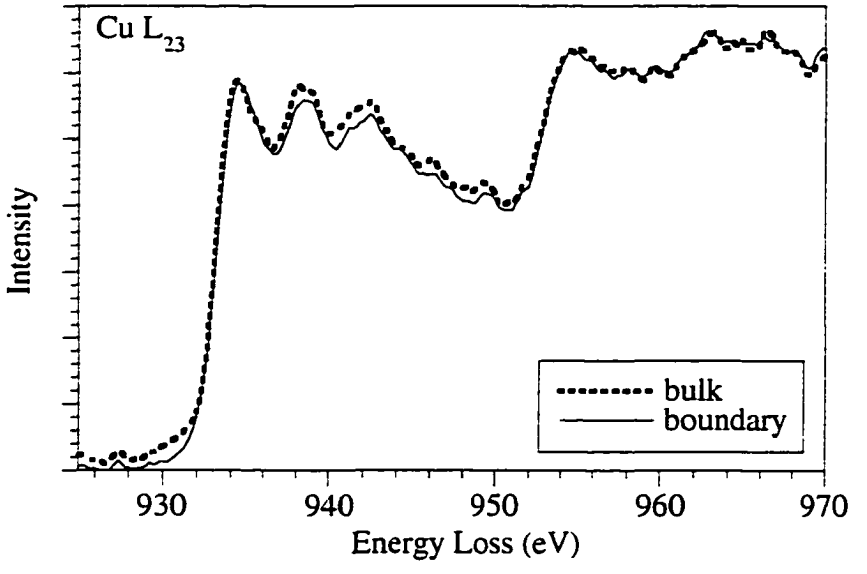


Figure 5.32 Cu $L_{23}$ edges from a grain boundary in Ag-doped Cu and from within the nearby bulk. No significant differences in the fine structure are observed.

# 6. DISCUSSION

## *6.1 XEDS Measurements of Segregation*

A number of segregating systems have been investigated in this work and for the Ni-S, Cu-Sb and Cu-Ag systems this is the first time, to our knowledge, that XEDS has been used to examine these materials. The results on Ag segregation presented in Section 5.1.4 are the first time that Ag segregation has been directly observed in Cu. Prior to this, grain boundary segregation of Ag could only be inferred from surface segregation studies (Menyhard (1993)).

Evidence of segregation can be directly, most simply and quickly observed by placing the small electron probe at the grain boundary and comparing the X-ray spectrum acquired to one acquired within the nearby grain. The Figures 5.2 (Ni-S), 5.20 (Cu-Sb) and 5.23 (Cu-Ag) show such experiments and the presence of excess impurity at the grain boundary is clearly observed by the extra intensity in the characteristic X-ray peaks for these impurity elements.

In Figure 5.24 it was shown that, at least for the case of Cu-Ag, it is more difficult to detect segregation using EELS. The main reason for this is that in EELS the intensity under the ionization edge is spread over a large energy range, rather than contained in a distinct peak as in XEDS. When EELS has good visibility, due to white lines for example, it can detect segregation as easily as XEDS and with better spatial resolution (Bruley et al. (1998)). In this work, the ionization edges for each of the impurity elements have very poor visibility due to the edge shape.

It was not one of the goals of this research to obtain detailed quantitative segregation levels. However, when segregation levels were obtained for a number of boundaries,

for example, the non $\Sigma$=3 grain boundaries in Bi-doped Cu shown in Figure 5.13b or the segregation levels in Sb doped Cu of Table 5.2, a large variation between boundaries was observed. This should serve as a caution against applying too carefully the segregation isotherms outlined in Section 2.1. The variation in segregation levels between individual grain boundaries is likely to be larger than that due to different thermal treatments.

The Ag- and Sb-doped materials were not studied in order to perform a detailed segregation study, but rather to discover what effect, if any these elements have on the electronic structure at the grain boundary and how this might relate to mechanical properties. The results of the segregation studies confirm that the material preparation procedure was successful in producing an excess concentration of these impurities at the grain boundary. Therefore, it was appropriate to perform an ELNES examination of grain boundaries in these materials.

A next step, after a simple comparison of spectra acquired on and off the grain boundary, is to acquire a profile of segregant distribution. Traditionally this is done by stepping the electron beam in a line perpendicular to the grain boundary. Examples of this approach for each of the systems were given in Figures 5.3 (Ni-S), 5.9 (Cu-Bi), 5.21 (Cu-Sb) and 5.25 (Cu-Ag). Quite often electron beam damage at 300 keV is the principal limitation while acquiring segregation profiles and the profiles of Figure 5.9 and 5.21 both show the effects of beam damage. In addition to the visual evidence of damage in the images of the sample after a profile, beam damage manifests itself by introducing an asymmetry into the segregation profile. Specimen drift is often a limitation, but can be all but eliminated if the specimen stage is allowed to mechanically stabilize for ~ 1 hour after the shifts have been used. Under the right conditions, it is possible to obtain segregation profiles with very good spatial resolution, as shown by

Figure 5.3, where the full width of the profile is ~ 2 nm. Section 6.3 contains a more complete description of the prediction of segregation profiles and resolution.

In this work we have introduced the approach of extracting segregation profiles from 2D maps. The advantages of mapping will be discussed below, but as can be seen with reference to Figure 5.12, profiles obtained in this way can have very high spatial resolution. In addition, beam damage and specimen drift are no longer limitations. As demonstrated by the asymmetric profile of Figure 5.7 grain boundary inclination is now easily identified and separated from other sources of asymmetry (specimen drift, beam damage).

*6.2 Mapping with XEDS*

It has been shown that it is possible to obtain 2D compositional maps with high spatial resolution using XEDS in a STEM. Mapping has been applied to detecting segregation in all of the systems of interest. As illustrated by Figure 5.11, which shows Bi segregation to a grain boundary in Bi-doped Cu, low levels of segregation, less than 1/10th monolayer, can be mapped and with a spatial resolution better than 2 nm. To our knowledge, no other laboratory is producing similar maps. When the segregation levels are quite low, as in Figure 5.11 and also the map of Sb in Cu (figure 5.22), the maps will be quite noisy.

Quite apart from their visual impact, quantitative information about segregation levels can be extracted from such maps. For example a raster scan can be simulated by integrating the counts, from elemental and background maps, within a defined area of the map and then following the same quantification procedures as are usually used for a raster scan. As shown by the example taken from Figure 5.11, such a quantification procedure gives segregation levels that agree very well with those measured using actual

raster scans. The profile extracted from Figure 5.11 and shown in Figure 5.12 shows that the spatial resolution in this map is on the order of the pixel size (and probe size) as the Bi signal at the boundary is only 1 pixel wide. Quantification of a segregation profile can be performed by scaling of a theoretical model to the experimental profile.Scaling of the profile of Figure 5.12 to a model segregation profile gave a segregation level which agreed, within experimental error, to segregation levels obtained with the other approaches described above. Similarly, the different Bi segregation levels to two different boundary facets, suggested by the map shown in Figure 5.10, was confirmed by measurements using raster scans (admittedly the difference in segregation level is only just statistically significant).

Therefore, a 2D map contains the same information as the traditional approaches of placing the electron probe on the grain boundary, rastering over a fixed area or obtaining a profile by stepping the beam along a line perpendicular to the boundary. Mapping has some advantages over these approaches. When acquiring a map an electron image is usually simultaneously acquired and therefore specimen drift, if present, is easily identified and its severity determined. In addition, for each point in the map, the electron probe only spends a very short time at the corresponding point on the specimen, therefore beam damage, which is often observed, especially at 300 keV, is minimal. The disadvantage being that the short dwell times mean that counting statistics at each point are also very poor, although integrating over many pixels will to some extent offset this. More often than not it is experimental factors such as specimen drift and electron beam damage that limit performance. When these factors are reduced, the full capabilities of the microscope can be utilized.

The main disadvantage of mapping is the long acquisition times. For example, a raster scan with good counting statistics can be acquired within 100 s, a profile will take 2-10

minutes, whereas a 2D map can take 20-60 minutes. When the information that is required is purely quantitative segregation levels or a large number of segregation profiles, mapping may not be the method of choice. Although it is possible in a fine grain material and optimizing mapping at lower magnifications (~200 kX) to obtain segregation levels for up to 30 grain boundaries in a single map (Williams et al. (1997)).

It has been demonstrated here that 2D X-ray mapping of grain boundary segregation is both possible and can provide the same information as other approaches. However the principal advantage of mapping is in the information that cannot be obtained reliably through any other approach. An example of this is the inhomogeneities in Bi segregation levels shown in Section 5.1.1.3. A series of spot analyses along a grain boundary may show such differences in the segregation levels, but there will always be doubt as to how well the electron probe was located on the grain boundary. A number of segregation profiles taken across different portions of the same boundary can be used, however, this is still less reliable than a map but is similarly time intensive. The inhomogeneities observed in the Cu-Bi system are believed to be a consequence of inhomogeneities in a surface accumulation of Bi, probably in a Bi-O-Cu phase. EELS experiments combined with surface cleaning of the sample suggested that such a surface phase might be responsible for both the unusually large Bi levels and the inhomogeneities. It was the maps of Figure 5.19 where the excess Bi was observed at the intersection of the grain boundary with the top and bottom surfaces of the foil that confirmed this supposition. It should be noted that a similar surface accumulation of Bi has been described by Donald and Craven (1979) and Grovenor and Rae (1981). This example illustrates the importance of cleaning samples immediately before insertion in the microscope, particularly if either quantitative segregation levels or electronic structure information is desired .

Even when a map only contains information that could be obtained in some other fashion, it may be the preferred way to present this information. For example, the same information shown in the map of the dissociated $\Sigma$=9 grain boundary of Figure 5.14 could be presented as a table showing the relationship between crystallography and segregation levels. However, the combination of an image and the compositional map demonstrates clearly and visually the preferential segregation to the $\Sigma$=9 section of this boundary. In a similar way the RGB image of the Bi/Si/Cr precipitate of Figure 5.15 is more readily interpretable with the aid of 2D mapping.

### *6.3 Simulation of Segregation Profiles and Spatial Resolution*

Experimental segregation profiles have been obtained, both directly and extracted from maps, with a spatial resolution as good as or better than any in the literature. The various approaches to modeling segregation profiles, outlined in Section 3.1.5 and based upon different assumptions about the interaction volume, have been used with the experimental conditions in this work. More importantly, detailed comparisons to experiment have been made. Figure 5.3 showed an experimentally obtained segregation profile of S at a grain boundary in Ni and compared to the different models. The approach of Doig and Flewitt (1982), describing the incident probe as having a two dimensional gaussian distribution that is broadened as it passes through the sample, gave a remarkably good fit to the experimental data. The truncated cone model of Baumann and Williams (1981) could not be made to agree with the experimental data using reasonable estimates for specimen thickness. The simplest model, where beam broadening is neglected, describes the profile surprisingly well, with the exception of the extended tails. The model of Doig and Flewitt (1982) was also able to adequately describe the segregation profiles obtained in a Bi-doped Cu specimen and given in

Figures 5.9 and 5.12. We can conclude from this that the gaussian model will best account for the interaction volume.

In the maps and segregation profiles of a boundary in S-doped Ni, shown in Figures 5.4-8, good agreement between the experimental and theoretical profiles was only obtained when it was assumed that either the segregated region at the grain boundary had a finite width of ~2 nm or alternatively the incident probe is size twice the previously measured value. Assuming a larger interaction volume due to the specimen being thicker than measured could not account for the discrepancy, as the main effect of thickness is to increase the tails of a segregation profile while maintaining a relatively sharp narrow profile at the center (also shown in earlier work by Hall et al. (1981)). One possible mechanism that could increase the effective probe size is specimen drift, however, in this example, specimen drift was minimal (< 0.1 nm/minute). Similarly, beam damage has also been observed to influence spatial resolution, mainly by sputtering and redistributing the segregant species. Beam damage was not observed while mapping. If a significant contamination layer were to build on the entrance side of the foil, then this C layer could broaden the incident probe before it reaches the actual specimen. Using the expression of equation 3.8 for electron intensity distribution as it passes through a specimen, it would require 100 nm of C to double the incident probe size from its known value. While this is a very thick contamination layer, it is not beyond the bounds of possibility.

It is also possible that the segregation layer itself does have a finite width and, to date, XEDS experiments have not had the spatial resolution to discriminate between a planar boundary and one with a small but finite width. Sputtering profiles in AES studies are consistent with planar segregation (Hondros and Seah (1977)) but the depth resolution is still 0.5-1 nm (that is 1-2 nm for the intact boundary) and so we cannot be entirely

certain that the segregated region is not 1-2 nm wide. Note that we also see a deficit in the Ni signal at the grain boundary, as we might expect from a "slab" boundary. It should be noted that this grain boundary is an isolated case and that the planar model provided a good description of the other boundary examined in the Ni-S specimen as well as boundaries in Bi-doped Cu. The grain boundaries in the Sb- and Ag-doped Cu specimens also showed quite broad measured segregation widths but, in these profiles and maps, specimen drift and damage were a concern. Conclusions about segregant distribution cannot be drawn except to say they are not inconsistent with equilibrium segregation. All the models used are analytic expressions and it would be interesting to compare the theoretical models and the experimental profiles to results from Monte-Carlo calculations.

These examples of modeling and segregation profiles, prompt the questions, "what is spatial resolution in the AEM?" and "how does it relate to what we can actually measure?". Equilibrium grain boundary segregation is assumed to have a spatial extent that is very much smaller than the expected resolution of AEM. With the exception of the profiles in Figures 5.4-8, the experimental results in this work support this assumption. In addition, when models of the expected segregation profiles for a planar boundary and a slab boundary 0.2 nm wide (the typical spacing for the close packed planes in Cu) are compared they are indistinguishable. Therefore, we might expect that the width of the measured segregation profile, at FWTM or FWHM, is an indication of the spatial resolution. Another apparently reasonable definition of spatial resolution is the diameter of the electron distribution that contains 90% of the electron intensity (Michael and Williams (1987)). However, this is a quantity that cannot be directly measured, but can be estimated before an experiment is performed. What is measured is a compositional distribution from a nominally well known material such as the

interphase boundary measured by Michael et al. (1990) or equilibrium segregation as done here.

How well does a predicted value of resolution, based on the definition of Michael and Williams (1987), agree with what we would measure from a segregation profile? Figure 6.1 shows the relationship between the width of a segregation profile (at FWTM and FWHM) together with resolution, 2R, defined as the diameter of a cylinder that contains either 50 or 90% of the electron intensity. The resolution, 2R, was calculated following Van Cappellan and Schmitz (1992), where the radius at which a gaussian electron distribution given by equation 3.8 contains some fraction Q of the total electron intensity is given by

$$Q = \frac{1}{h}\int_0^h \int_0^{2\pi} \int_0^R \frac{1}{\pi(2\sigma^2 + \beta t^3)} \exp\left(\frac{-r^2}{2\sigma^2 + \beta t^3}\right) r\,dr\,d\vartheta\,dt \qquad (6.1)$$

which simplifies to

$$Q = \frac{1}{h}\int_0^h \left[1 - \exp\left(\frac{-R^2}{2\sigma^2 + \beta t^3}\right)\right] dt \qquad (6.2)$$

This equation was solved for R with Q=0.5 and 0.9 and as a function of thickness using numerical integration and the results are plotted in Figure 6.1. As outlined in Michael et al. (1990), R evaluated in such a manner will be for the for the 2D case and has been reduced to the 1D equivalent by dividing by a factor of $\sqrt{2}$.

The width of segregation profiles at FWTM and FWHM were evaluated from the theoretical grain boundary segregation profiles of equation 3.30, where the same gaussian electron distribution of equation 3.8 is assumed. The conclusion that can be drawn from Figure 6.1 is that an evaluation of spatial resolution based on the diameter

of the cylinder containing some fraction of the electron distribution will give a reasonable estimate of the expected resolution in segregation profiles except for thick specimens. As the specimen thickness increases, the tails of the segregation profiles increase while the sharp central section remains relatively unchanged and this is evident by the width at FWTM increasing more rapidly with thickness than the width at FWHM.

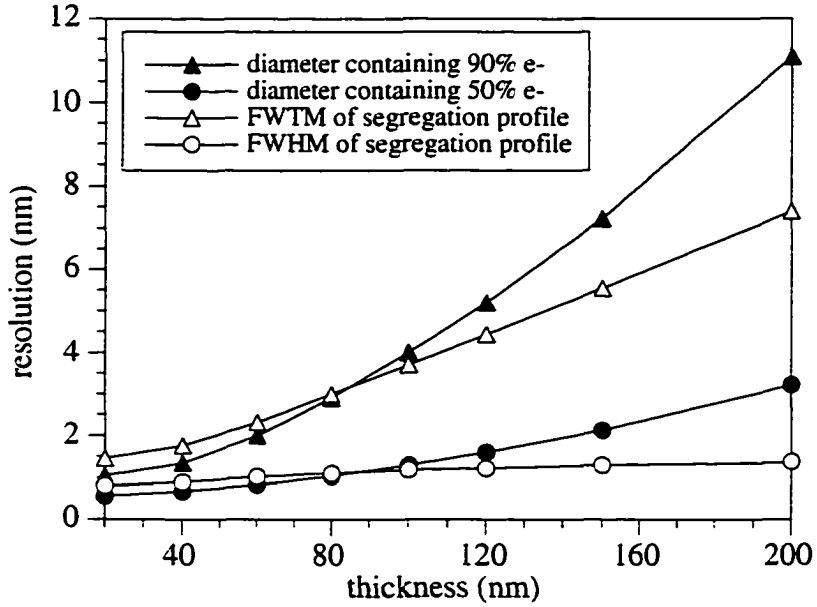


Figure 6.1 Resolution 2R, where R is the radius of the cylinder containing either 50 or 90% of the total electron intensity compared to the widths at FWTM and FWHM of the segregation profile (Matrix is Cu, beam energy 300 keV, $d_{FWTM}$ is 1.4 nm).

The approach taken above and in Michael et al. (1990) is a somewhat roundabout and arbitrary way of assessing spatial resolution. Starting from a nominally known composition distribution, an experimental distribution is obtained. Assumptions about the electron intensity through the thickness of the sample are then made and the theoretical model verified against the experimental data. An arbitrary criterion (e.g. the 90% electron intensity) is then used to place a value on spatial resolution. Perhaps a better assessment of spatial resolution in AEM would be a practical definition such as the smallest separation between two compositionally discrete regions that can be

resolved. This is analogous to criteria in other branches of microscopy such as HREM but for AEM it has been difficult to find a material that would be suitable for such a resolution test. In Chapter 8 a possible specimen for spatial resolution testing in the AEM is suggested.

*6.4 Detectability and Quantification of Grain Boundary Segregants*

In Section 3.1.2 it was shown that the assumptions made about the interaction volume can have a major influence on quantification of a grain boundary segregant and, in a similar manner, on the absolute values for the detectability limits. The effect of the interaction volume was included by a geometric factor g(d,h) (equation 3.14) and the expressions for this factor obtained using the more common assumptions about interaction volume are given in Equations 3.15-3.22. The comparisons between experimental segregation profiles and the theoretical models suggest that the best description of the interaction volume is the gaussian model introduced by Doig and Flewitt (1982). Using the truncated cone model, such as done by Baumann and Williams (1981) and Michael and Williams (1984) , could overestimate segregation levels by up to a factor of 4. When a quick rough estimate of segregation levels are required the cylindrical approach can be used, however it may still be in error by a factor of 2. It should also be noted that a reasonable estimate of the specimen thickness is also necessary if accurate quantification levels are desired. For a reasonable range of sample thicknesses (50 to 150 nm) the geometric factor, and hence calculated segregation levels can vary by up to a factor of two (cf. Figure 3.6).

The pitfalls associated with quantification, when placing the small electron probe at a grain boundary, can be avoided if instead the probe is rastered over a fixed area while X-ray spectra are collected. In this manner the interaction volume becomes well defined

and, as shown in Figure 3.7, beam broadening, and hence the effect of specimen thickness, is not as significant. The error in calculation of segregation levels will then primarily be due to counting statistics, rather than uncertainties about the interaction volume. However, improved accuracy of quantification comes at the price of significantly reduced detectability. For example, using equation 3.24 and typical values for $I^b_s$ and $I_m$ with the usual operating parameters ($d_{FWTM}$=1.4 nm, $i_b$=0.6 nA, 100 s acquisition), for spot mode one would obtain a minimum detectable level of segregation, $\Gamma_{min}$, for Bi in Cu between 0.1 and 0.2 atoms/nm$^2$ (actual value depends on thickness) or ~ 0.02 monolayer. If the spectrum was acquired instead using the raster approach with $w$=8 nm $\Gamma_{min}$=0.6 atoms/nm$^2$, a reduction in minimum detectable segregation levels of at least a factor of three.

The motivation for using a raster scan, despite the lower sensitivity than a stationary probe, is as much to overcome some of the more practical experimental limitations as it is to improve the accuracy of quantification. Firstly, electron beam damage is not as severe when using a raster scan. Secondly, the requirements on orientation of the grain boundary plane are not as stringent because the entire grain boundary plane can still be contained within the interaction volume. Lastly, specimen drift can be detected and corrected during acquisition. Various techniques can be used to overcome the limitations when using a stationary probe, for example, waiting for the sample stage to stabilize in order to minimize drift, careful orientation of the grain boundary plane and thickness measurements to improve quantification. However, these are all time-consuming measures and there is a trade-off between the number of separate grain boundaries examined and the sensitivity for each measurement.

Values for segregation levels will also be directly influenced by the values taken for the k-factor. In this work theoretical k-factor calculations were performed. If the absolute,

as opposed to relative, segregation levels must be known accurately it would be preferable to use standards for k-factor calculation.

*6.5 Σ=3 Grain Boundaries in Bi-Doped Cu*

A number of Σ=3 grain boundaries in the material provided by D. E. Luzzi were examined with XEDS for Bi segregation. Although one might not expect segregation to such grain boundaries, particularly the {111}/{111} facets, HREM studies showed a loss of symmetry at these boundaries that could be explained by an ordered Bi layer at these boundaries Luzzi (1991ab). It was argued that segregation occurs to curved Σ=3 or near Σ=3 boundaries which then facet with segments having {111}/{111} plane pairs (Blum et al. (1990)).

In this work, Bi segregation was not observed to any of the Σ=3 grain boundaries, with the exception of incoherent facets in a dissociated Σ=9 grain boundary. Some of the Σ=3 boundaries examined were obviously annealing twins at which we would not expect to see Bi segregation. Most non Σ=3 grain boundaries had detectable levels of segregation indicating that Bi was retained in the material during the further mechanical and heat treatments. The maximum possible segregation that could have occurred to the Σ=3 boundaries and not have been detected is ~1 atom/nm$^2$ (the shaded region in Figure 5.13a). This is not a particularly low detectability limit because nearly all measurements were performed with a raster scan. However, the interaction volume is well defined and the experimental limitations discussed in Section 6.3 are minimized and so we can be reasonably certain about the absolute value of this limit.

The structure for the Σ=3 grain boundary containing Bi suggested by Luzzi (1991ab) is shown below in Figure 6.2. The grain boundary coverage for such a structure is 5.6

atoms/nm$^2$ which is at least 5 times larger than the maximum possible grain boundary coverage measured here.

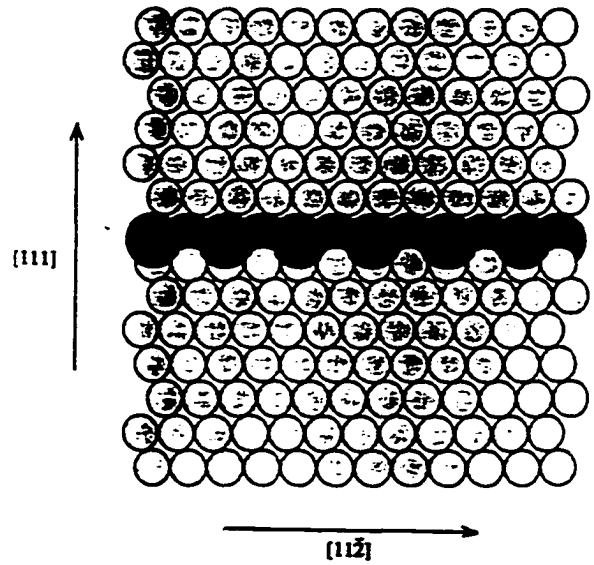


Figure 6.2 Structure of $\Sigma$=3 grain boundary containing Bi, proposed by Luzzi (1991ab) on the basis of HREM studies.

The conclusion that can be drawn is that the structure observed by Luzzi (1991ab) was not observed at the $\Sigma$=3 grain boundaries examined in this study. There are a number of different possible explanations. Firstly, in the limited number of boundaries examined, we may not have been fortunate enough to come across a grain boundary with such a structure. The mechanical and thermal treatments performed may not have properly replicated those performed by Luzzi (1991ab). Alternatively the structure observed by Luzzi (1991ab) was due to some other cause than Bi segregation, even though the image simulations based on their model gave good agreement to experimental HREM. Further understanding of this disagreement would require a combined HREM and XEDS study of a large number of grain boundaries in this material. As a $\Sigma$=3 grain boundary containing Bi was not found it was not possible in this work to compare experimental ELNES on the same grain boundary structure as had been used in the layer KKR calculations (Keast et al. (1998)).

Bi was also not observed at the Σ=3 bicrystals. One might wonder where the Bi goes and in some cases it has been seen to precipitate on the grain boundary. The map of the precipitate (Figure 5.15 in the Σ=3 bicrystal showed that another smaller precipitate, itself with a complex chemistry, was a nucleation site for Bi precipitation. In addition, the Σ=9 boundary of Figure 5.14 indicates that Bi will preferentially segregate to facets nearby that do not have the Σ=3 orientation.

*6.6 Comparison of XEDS and AES*

The other principal technique used for qualitative and quantitative information about segregation is AES. Comparisons between AES and AEM measurements on the same material have confirmed that the different measurement techniques produce similar quantitative results (Partridge and Tatlock (1992), Vatter and Titchmarsh (1997)). Quantification in AES has similar limitations to AEM. For example, assumptions must be made about the distribution of segregant and the volume of material that contributes to the measured signal. In AES the volume of interaction is controlled by the escape depth of the Auger electrons. As in AEM, conversion of Auger intensity ratios into compositional ratios requires either comparisons with standard sample or theoretical calculations. The comparisons performed by Partridge and Tatlock (1992) and Vatter and Titchmarsh (1997) showed that the errors inherent in the two techniques were of a similar order. The accuracy of AEM may be better for multicomponent systems whereas AES allows for more rapid acquisition of data (Vatter and Titchmarsh (1997)).

The main limitation in AES for grain boundary segregation studies is the requirement that the sample be fractured intergranularly. The most obvious consequence of this is that grain boundaries that are not brittle cannot be examined. The example of the segregation of Ag in Cu is a good demonstration of this limitation as Ag does not

promote embrittlement. The $\Sigma$=9 grain boundary shown in Figure 5.14 could also not have been observed with AES as this section of grain boundary has no nearby grain boundaries with significant Bi to allow a complete fracture path. Similarly, the lateral resolution of AES is often insufficient to ensure that precipitates within a grain boundary, such as the Cr precipitate in Figure 5.19, do not contribute to the measured signal.

The other question that must arise is whether the fracture process will favor analysis of grain boundaries with higher segregation levels, as these will be the most brittle. For example, the lowest recorded segregation level in Bi-doped Cu that was statistically significant in this work was 0.5±0.3 atoms/nm$^2$ (0.05 monolayer). For the same annealing temperature, the lowest measured grain boundary coverage in the AES studies of Powell and Woodruff (1976) was ~2.5 atoms/nm$^2$. This suggests that the fracture process may select boundaries with a high grain boundary coverage.

It is difficult to directly compare segregation levels obtained here to values in literature obtained with AES. Even though Partridge and Tatlock (1992) and Vatter and Titchmarsh (1997) showed that AEM and AES gave similar results, in these systematic investigations, consistent assumptions were made about segregant distribution and the coverage that constitutes a monolayer. There has been very little consistency in the assumptions used for quantitative studies in the literature and this is well demonstrated by a review of the examples of segregation measurements of Bi-doped Cu . Early examples (Joshi and Stein (1971), Powell and Mykura (1973)) calibrated Bi peak intensities in the Auger spectrum to the intensities obtained from pure Bi and expressed grain boundary composition in a wt %. Implicit in these investigations was the assumption that 100 wt% was equivalent to a monolayer and the contribution to the measured intensities from layers below the surface was not considered. Later

investigations (Powell and Woodruff (1976), Fraczkiewicz and Biscondi (1985)) calibrated the Bi intensities at grain boundaries to the Auger peak ratios when Bi was deposited on a Cu substrate. A knee is observed in the Auger peak ratio at a coverage of a monolayer, at which point the Bi signal from the first monolayer is attenuated by the second monolayer. The Bi thickness at which this knee occurred, measured by Powell and Woodruff (1976), can be converted into a $\Gamma$ equivalent to 9.8 atoms/nm$^2$ which is relatively close to the value of 9.3 used throughout this work. More recently, Chang et al. (1997) have used theoretical models to convert Auger intensity ratios into a number of monolayers. Earlier AEM studies have assumed that the segregant is contained in a boundary region 1 nm wide and expressed grain boundary concentration as a wt% in this region. Until the AEM and AES communities, both within each community and between them, come to some consensus about the best way to express grain boundary concentration it will be difficult to compare results from different studies. As stated in Section 3.1.3 it is believed that the best way to express an excess grain boundary concentration will be in a coverage in an equivalent atoms/nm$^2$ as it relies on the fewest arbitrary assumptions.

*6.7 Electronic Structure and GBE*

In both S-doped Ni and Sb-doped Cu, a change in the ELNES of the matrix elements was observed at the grain boundary. In the non-embrittling system of Ag-doped Cu no such change was observed.

The main feature of the Ni $L_{23}$ edge is the white line due to transitions to the unoccupied states in the d-band. The intensity of this white line is increased at a grain boundary in the S-doped Ni (Figure 5.28), indicating that there are less electrons in the d-band, just above the Fermi level, at the grain boundary. At a grain boundary in Sb-doped Cu, extra

intensity was observed in the Cu $L_{23}$ edge in the small peak just above edge threshold (Figure 5.30). Although the d-band of Cu is nominally full, this first peak in the ELNES of Cu is due to the tail of the d-band which just extends above the Fermi level. Therefore, the results in Sb-doped Cu also suggest that the occupancy of the d-band, just above the Fermi energy, is reduced at the grain boundary. It follows that the occupancy of the d-band at grain boundaries in Ag-doped Cu is unchanged. The experimental results thus suggest that GBE embrittlement is associated with a change in the occupancy of the d-band just above the Fermi level. The comparison between Ag and Sb at Cu grain boundaries has allowed a separation between effects due to atomic size of the segregant and those due to electron configuration.

In the case of the Ni $L_{23}$ ionization edges, care must be taken to avoid the introduction of artifacts due to small changes in thickness, as shown in Figure 5.27. A thinner specimen has an apparently larger white-line intensity, although this effect can be removed through deconvolution of the low-loss spectrum. If, however, the low-loss spectrum is obtained from an area with a slightly different thickness than the ionization edge, then deconvolution will artificially alter the white line intensity. Even when the low-loss spectrum that is used for deconvolution comes from the identical area as the ionization edge, contamination can change the apparent thickness. In the spectra of Figure 5.28, showing changes in the white line intensity at a grain boundary, the difference in thickness was measured to be less than 3% and no visible contamination occurred. Therefore, we can be reasonably certain that the increased white line intensity of Figure 5.28 is associated with the segregation of S and is not some artifact due to thickness. As shown by Figure 5.31, the effect of thickness on the Cu $L_{23}$ edge is very different to the change observed at a grain boundary containing Sb.

The experimental results presented here are consistent with the earlier work on Bi-doped Cu (Keast et al. (1998)), shown in Figure 6.3 and the results of Muller et al. (1996) on B-doped $Ni_3Al$, shown in Figure 6.4. They are not consistent with the results in P doped Fe of Ozkaya et al. (1995) where a decrease in white line intensity at the grain boundary was observed. However, it is not entirely apparent in the work of Ozkaya et al. (1995) that the effect of thickness was properly accounted for. Interestingly however, the layer KKR calculations of Alvarez and Rez (1997) predicted a decrease in white line intensity for P-doped boundaries.

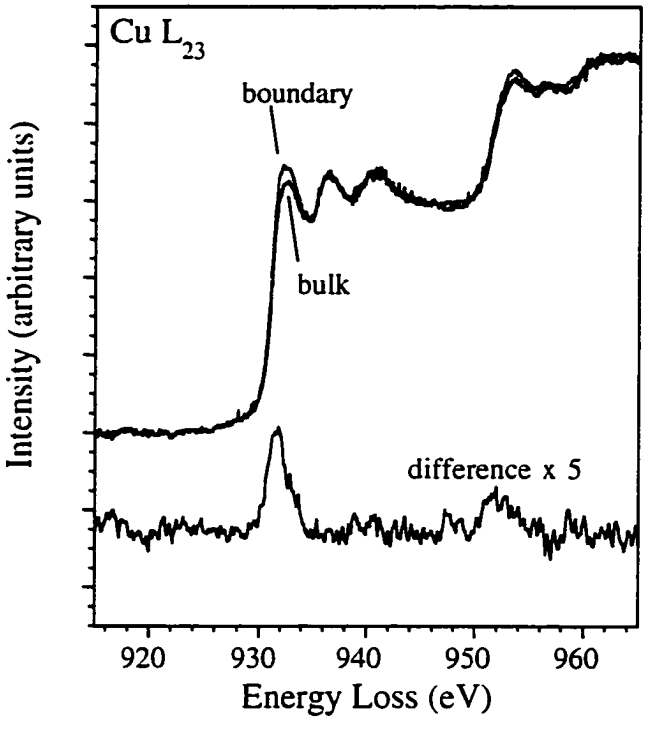


Figure 6.3 Change in the ELNES at a grain boundary in Bi-doped Cu. An increase in white line intensity is seen at the grain boundary and this is consistent with the results presented in Section 5.2 from S-doped Ni and Sb-doped Cu.

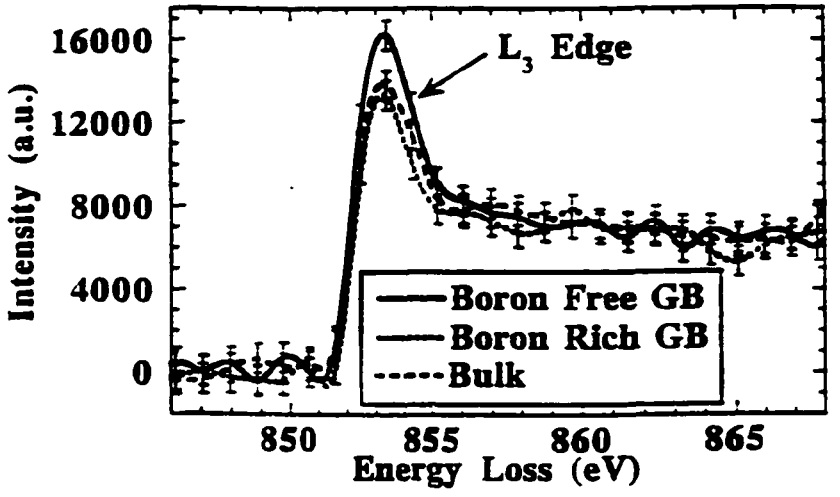


Figure 6.4 Change in the ELNES for B-doped $Ni_3Al$ (from Muller et al. (1996)). The B free grain boundaries are intrinsically brittle and show an increased white line intensity compared to the bulk value and from grain boundaries containing the ductilizing B.

One of the principal concerns about the results of the ELNES studies shown here is repeatability. For example, only one observation of a change in the electronic structure of a grain boundary containing Sb was observed. In all of the systems studied, there were many grain boundaries examined, which were known to contain a segregating impurity, and yet no change in the electronic structure was observed.

The problem arises because it is an experimentally challenging problem to detect such small changes in the ELNES. Firstly, we are looking for small changes in a large signal. In addition, the electron probe is much larger than the grain boundary region and so therefore the most of the measured spectrum arises from the bulk material. Other limitations include the ability to exactly place the electron probe on the grain boundary, specimen drift and any grain boundary inclination.

In addition to the difficulty in detecting any small changes in the ELNES, is the likelihood of introducing artifacts, the example of the effect of thickness on the Ni $L_{23}$ edges being one such case. Channel-to-channel gain variations must be carefully

eliminated, particularly if the boundary spectrum and the bulk spectrum have slightly shifted in energy. The method of correcting for gain variations described in Section 4.3 is probably most appropriate as it can be done quickly and easily at around the same time as spectra are acquired. While not accounting for long range gain variations across the diode array, it well describes the short range variations that produce spurious peaks in ELNES spectra.

Another consideration is the energy stability of the electron source. Quite often a shift in energy of ~ 1 eV or more can occur at apparently random intervals in time. During long acquisition times this will result in a "smearing" of the fine structure in the edge. Therefore if energy shifts were observed to occur, those spectra were discarded. Care should be taken as it is quite conceivable that a boundary spectrum will appear to have a sharper peak at edge onset when compared to a bulk spectrum acquired during an energy shift.

The post-collection processing of spectra is yet another area where artifacts can be introduced. The procedure to deconvolve low-loss spectra is particularly troublesome. Any small differences are accentuated by deconvolution. In this work, if no difference between the spectra was observed before deconvolution, then any differences observed after deconvolution were not considered to be real. When two spectra are compared, they are scaled to match at energies far beyond the edge onset (50-100 eV above). In order for scaling to work properly, the subtraction of the background must be performed properly, and relies on the fact the pre-edge region of the two edges are not significantly different. Any changes in thickness or contamination level will not ensure this.

To help overcome many of these limitations, a procedure was adopted where spectra were acquired in rapid succession (separated by only a few seconds), often in the sequence boundary-grain1-grain2-boundary. This sequence aided in determining whether any changes observed were a consequence of grain boundary effect or which might be due to the effects of time (e.g. energy drift, contamination). All of the regions examined would be within a 20 nm region in order to minimize effects of thickness.

It can be seen from the description above that, with careful control of the experiment, many of the experimental limitations can be mitigated. However it will rely heavily on the subjective judgment of the operator as to whether any observed effects are real or due to artifacts. Given these caveats, the results presented here are encouraging in suggesting that it should be possible to observe changes in the electronic structure at grain boundaries and should encourage further work in this area.

To overcome some of the limitations of detectability of when examining ELNES at grain boundaries we would wish to make the electron probe as small as possible so that the electronic structure at the grain boundary is the dominant contribution to the ELNES, instead of a small fraction as was the case here. Naturally very small electron probes have very little current and signal to noise becomes a problem. Spectrometers are available that use a CCD camera instead of a diode array and these have better signal to noise performance and would be preferable for such experiments.

Assuming that the ELNES results presented in Chapter 5 represent real changes in the electronic structure and can be repeated, it has been generally observed that there is an increase in the white line intensity associated with grain boundary embrittlement. The questions that must now be answered are, "how does the bonding at the grain boundary change so as to produce a decrease in occupancy of the d-band just above the Fermi

energy" and "how does this bonding change reduce cohesion at the grain boundaries and make them brittle?".

The electronic structure of Cu and Ni can be understood with reference to Figure 6.5 below (from Sutton (1993)) which shows a schematic for the DOS of the transition metals. There is a narrow, partially filled d-band which overlaps with a broad free electron like s-p band. The filling of the d-band increases, across the transition metal series, until at Cu the d-band is nominally full and the Fermi level sits just above the d-band.

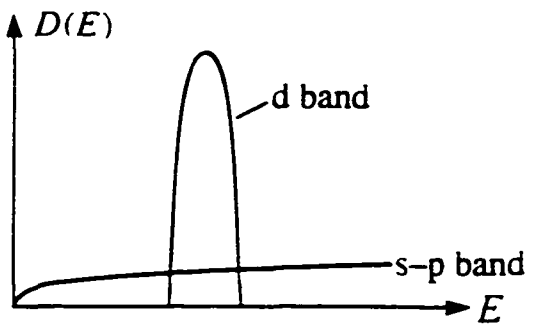


Figure 6.5 Schematic of the DOS for the transition metals (from Sutton (1993)) showing the narrow tightly bound d-band overlapping with a broad, free electron like s-p band.

The trends in the cohesive energy across the transition series can be related to the filling of the d-band. The bond energy, $U_{bond}$, the change in electronic energy, as we bring atoms together to form the solid (see Sutton (1993), Pettifor (1995) or Muller et al. (1998) for a discussion of how this term arises), is given by

$$U_{bond} = 2\int_{0}^{E_F}(E-\alpha)D(E)dE \qquad (6.3)$$

where (E-$\alpha$) is the energy of the state with energy E relative to the atomic state $\alpha$ and D(E) is the total density of states.

The Friedel model (Sutton (1993) contains a good description of the Friedel model) assumes that the d-band for the transition metals can be approximated by a rectangular DOS of width W, in which case the integral of 6.3 becomes trivial and

$$U_{bond} = -\frac{W}{20} N_d (10 - N_d) \qquad (6.4)$$

where $N_d$ is the number of d electrons per atom. This simple model was able to describe the parabolic variation in cohesive energy across the transition metal series. We already know that the intensity of the white lines in the $L_{23}$ edges for the transition metals can be related to $N_d$ (cf. Section 3.2.2). A simple analysis might say that the experimentally observed increase in white line intensity at the grain boundaries is due to a decrease in $N_d$ and hence cohesive energy. However, such an approach assumes that when a transition metal is bonded to another elemental species, the shape of the d-band remains unchanged and it is only the filling of the band that changes. This approximation is called the rigid-band model and for it to apply there must be a net flow of charge from one atomic species to the other, that is, an ionic bond is formed. The electron screening in metallic systems is very good and it has been argued that for metallic alloys we must assume a local charge neutrality and therefore the rigid-band model is not appropriate (Sutton (1993), Muller et al. (1998)). Experimentally, we would expect to see a chemical shift in the ionization edge onset if an ionic bond were formed between the matrix metal and the metal impurity and this was not observed in these experiments, within experimental limitations.

The effect of the impurity atom is therefore not to change the filling of the d-band, but rather to alter its shape. A change in the shape of the d-band will also alter cohesion,

through equation 6.2. Muller (1998) developed the relationship between changes in the bond energy of equation 6.2 and changes in the unoccupied DOS, as measured in the EELS spectrum to give

$$\Delta U_{bond} \approx \Delta E_{L_3} H_d - \Delta m_d^{(1)} \tag{6.5}$$

where $\Delta E_{L_3}$ refers to the chemical shift, $H_d$ is the number of holes in the d-band (i.e. 10-$N_d$) and

$$m_d^{(1)} = \int_0^{\infty} E n_d(E) dE \tag{6.6}$$

is the first moment of the EELS spectrum. E is measured with reference to the Fermi energy (i.e. $E_F$ =0)

If there is no core-level shift then the shape of the ionization edge can predict the trends in cohesion and Muller (1998) states

> "If the edge shape changes from sharply peaked at the edge onset to flatter and broader, then the bond strength has also increased (as the first moment of the EELS spectrum has also increased)."

This interpretation is consistent with the results presented in this work, that is an increase in the peak height above edge onset is associated with embrittlemet. It is also generally consistent with the mechanism for embrittlement suggested by Losch (1979). As outlined in Section 2.3, Losch (1979) suggested that the electrons in the partially filled p-states of the impurity atom form strong directional bonds with the host metal atoms. This impurity induced rehybridization reduces the strength of the metal-metal bonds. Unlike the mechanism of Losch (1979), Muller (1998) assumes that the number of electrons in the d-band remains unchanged, and it is only the shape of the d-band that changes. The mechanism suggested by Messmer and Briant (1982) is inconsistent with the assumptions of local charge neutrality.

Evidence supporting bond rehybridization with the p-states of the impurity atoms comes from the layer KKR calculations presented in Keast et al. (1998). In that work, the structure of a Σ=3 Cu grain boundary containing Bi, proposed by Luzzi (1991ab) and shown in Figure 6.2, was used to calculate the electronic structure.Figure 6.6 below shows the calculated Bi p DOS with the Cu d DOS at the grain boundary. A similar peak in these DOS at the same energy (~3.5 eV) is an indication of bond hybridization between these states. The peak in the experimental measurements of the Cu d DOS (Figure 6.3) occurs at a different energy than the calculated peak and this is possibly due to differences in atomic structure. Ideally one would perform both experimental measurements and calculations on a well-known grain boundary structure, and if possible comparisons between embrittling and non-embrittling segregants made. A proposed set of such experiments will be described in more detail in Chapter 8.

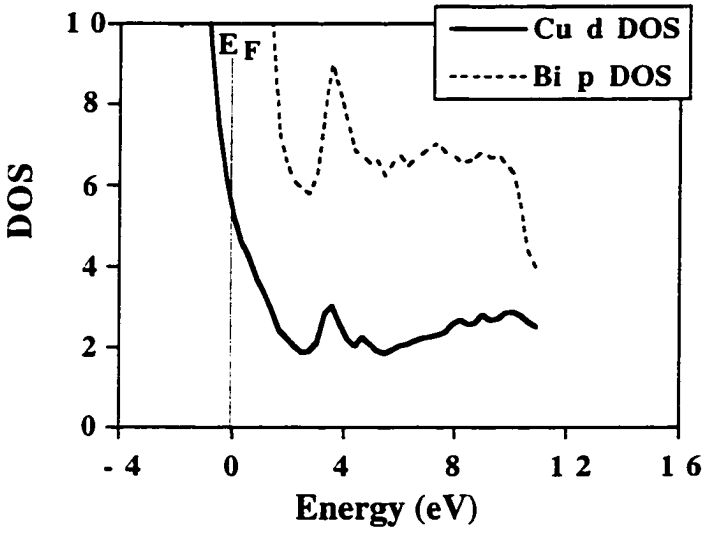


Figure 6.6 Comparisons between the calculated Cu d and Bi p DOS where the similar peak in both DOS indicates bond hybridization between these states (Figure courtesy of P. Rez).

# 7. SUMMARY AND CONCLUSIONS

A number of different systems in which grain boundary segregation occurs have been examined with AEM and compositional information with a spatial resolution equal to or better than any in the literature has been obtained. More importantly, it is now possible to collect 2D compositional maps of grain boundary segregation while maintaining good spatial resolution and sensitivity. It has been demonstrated that 2D maps contain the same information as that in more traditional approaches but with several advantages.

Segregation profiles, either obtained directly or extracted from maps have been compared to theoretical models, based on different assumptions about the interaction volume. The best description of the interaction volume is that due to Doig and Flewitt (1982) where the incident electron beam is described by a gaussian distribution that is broadened as it passes through the specimen. It follows that, if accurate quantification of segregation levels is desired when a small electron probe is placed at a grain boundary, the quantification procedures using the gaussian electron distribution and described in Section 3.1.3 should be used and a good knowledge of specimen thickness will be required. The most accurate way to obtain compositional information is through a raster scan and it has been shown that at 300 keV, beam broadening will not have a significant effect. However, improved accuracy of quantification comes at the price of a reduction in sensitivity by at least factor of 3.

For the first time a direct observation of segregation of Ag to grain boundaries in Cu has been observed and the width of the segregated region is consistent with equilibrium segregation. Segregation was not observed at $\Sigma$=3 grain boundaries in Bi-doped Cu, a result that is inconsistent with those of Luzzi (1991), Luzzi et al. (1991), and the reason for this is at this time unknown.

The ELNES investigations of the embrittling systems of S-doped Ni and Sb-doped Cu both showed an extra intensity in the white lines just above the ionization-edge onset. The effects observed here are consistent with earlier results on Bi-doped Cu and with those on B-doped $Ni_3Al$. This increase in white-line intensity is interpreted as being due to a change in the shape of the d-band, a consequence of impurity induced rehybridization. Taking the interpretation of Muller (1998) that a taller, sharper peak at in the ionization edge is indicative of a reduced cohesion, then these results are consistent with the GBE observed in these systems. On the other hand, there was no effect on the ELNES when Ag was present at the grain boundary. This suggests that the observed effects in the ELNES are indeed associated with a reduction in cohesion and not simply a consequence of structural rearrangements at the grain boundary due to the segregant.

The results presented here add to the evidence that there is a single electronic mechanism responsible for GBE, regardless of the transition metal or the impurity atom involved. It is likely that the electrons in the partially filled p-shells of the impurity atoms form directional, covalent bonds with matrix metal atoms. This bond rehybridization will alter the shape of the d-band and in doing so reduce the cohesion at the grain boundary.

# 8. FUTURE WORK

The discussion of Section 6.2 suggested that the current definitions of spatial resolution in the AEM are somewhat arbitrary and do not describe a practical resolution limit that is consistent with definitions used in other branches of microscopy. In recent years, technological advancements in the deposition of nanolayered materials has meant that materials with compositional variations below the expected resolution of the best available AEMs can be produced. For example, it has recently been shown that the layers in a Cu/Nb multilayer structure with a layer thickness of 1.5 nm can be resolved on the VG 603 (Keast et al. (1998)). Work is in progress on 1.0 nm layer spacing materials where the layer spacing is now below the $d_{FWTM}$ of 1.4 nm. An ideal test specimen of resolution in AEM would be a multilayered material consisting of sets of layers with a variety of spacings, some of which are below the expected resolution. If layers were oriented perpendicular to edge of a wedge specimen, the effect of thickness on resolution could also be examined. Figure 8.1 illustrates such a specimen.

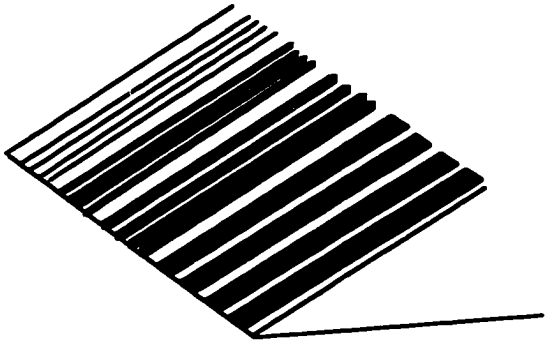

Figure 8.1 Schematic of an ideal test specimen for resolution in the AEM.

An interesting experiment would involve testing spatial resolution using such a specimen comparing the capabilities of an AEM utilizing a small spot to those of the recent generation energy filtered TEMs.

The approach to modeling XEDS segregation profiles taken in this work was an analytic approach, and appeared to agree reasonably well with experiment. Monte-Carlo techniques are also widely used to model compositional distributions obtained in AEM. It would be useful to compare simulations based on Monte-Carlo calculations, calculated using the current experimental parameters. The advantage of the Monte-Carlo approach is that it is no more difficult to model more complex compositional distributions.

The experimental results presented here are very promising in that they suggest that a single mechanism is responsible for grain boundary embrittlement. However the only way to be more certain that the interpretation that has been taken for the ELNES results is correct is by comparison with quantum mechanical calculations. The difficulty with calculations is that a well-known and periodic grain boundary structure must be used and yet experimental results are usually from random, non-periodic boundaries. Ideally we would like to perform experimental and theoretical examinations of the same grain boundary structure. In the Cu system the $\Sigma$=5 boundary is an ideal candidate. Atomic simulations have shown that Sb, Bi and Ag all segregate to the same sites in this structure and yet have a different effect on mechanical properties. Experimental observations have confirmed the validity, for the case of Bi, of this atomic structure. Experimental investigations of the electronic structure using $\Sigma$=5 bicrystals with each of these segregants, in addition to calculations of the expected electronic structure would aid considerably in deciding whether the interpretation of the mechanism for GBE used so far is correct.

## REFERENCES


U. Alber, H. Müllejans and M. Rühle, *Ultramicroscopy*, **69** (1997) 105.

J. R. Alvarez and P. Rez, *Proceedings of Microscopy and Microanalysis*, (edited by G. W. Bailey, R. V. W. Dimlich, K. B. Alexander, J. J. McCarthy and T. P. Pretlow), Springer, Cleveland, Ohio, 1997, p. 973.

I. Ames, F. M. d'Heurle and R. Hostman, *IBM J. Res. Develop.*, **14** (1970) 461.

K. Aoki and O. Izumi, *J. Japan Inst. Met.*, **45** (1979) 1190.

P. E. Batson, *Nature*, **366** (1993) 727.

S. F. Baumann and D. B. Williams, *J. Microsc.*, **123** (1981) 299.

J. Bentley, *Proceedings of Microscopy and Microanalysis*, (edited by G. W. Bailey, R. V. W. Dimlich, K. B. Alexander, J. J. McCarthy and T. P. Pretlow), Springer, Cleveland, 1997, p. 533.

B. Blum, M. Menyhard, D. E. Luzzi and C. J. McMahon, Jr., *Scripta Met. et Mat.*, **24** (1990) 2169.

B. S. Bokshteyn, G. S. Nikol'sky and A. N. Smirnov, *Phys. Met. Metall.*, **72** (1991) 142.

B. Bokstein, E. Glickman, G. Nikolsky and A. Smirnov, *Materials Science Forum*, **126-128** (1993) 583.

G. A. Botton, G. Y. Guo, W. M. Temmerman and C. J. Humphreys, *Phys. Rev. B*, **54** (1996) 1682.

D. Bouchet and L. Priester, *Scripta Met*, **20** (1986) 961.

C. L. Briant, *Acta metall.*, **31** (1983) 257.

C. L. Briant, *Met. Trans.*, **21A** (1990) 2339.

C. L. Briant, *Phil. Mag. Lett.*, **73** (1996) 345.

N. D. Browning and S. J. Pennycook, *J. Microsc.*, **180** (1995) 230.

J. Bruley, J. Cho, J. C. Fang, A. M. Thompson, Y. Z. Li, H. M. Chan and M. P. Harmer, *J. Mater. Res.*, (1998) in press.

J. Bruley, V. J. Keast and D. B. Williams, *J. Phys. D: Appl. Phys.*, **29** (1996) 1730.

R. Brydson, *EMSA Bulletin*, **22** (1991) 57.

R. Brydson, H. Sauer and W. Engel, in *Transmission Electron Microscopy in Materials Science*, (edited by M. M. Disko, C. C. Ahn and B. Fultz), The Minerals, Metals and Materials Society, 1992, p. 131.

J. H. Bulloch, *Materials at High Temperature*, **12** (1994) 311.

H. K. Chang, R. S. Weidman and J. K. Lee, *Surf. Sci.*, **144** (1984) 224.

L. S. Chang, E. Rabkin, B. Straumal, P. Lecek, S. Hofmann and W. Gust, *Scripta Met. et Mat.*, **37** (1997) 729.

L. S. Chang, E. Rabkin, B. B. Straumal, S. Hofmann, B. Baretzky and W. Gust, *J. Phase Eq.*, **18** (1997) 128.

J. Cho, M. P. Harmer, H. M. Chan and J. M. Rickman, *J. Am. Ceram. Soc.*, **80** (1997) 1013.

T. H. Chuang, W. Gust, L. A. Heldt, M. B. Hintz, S. Hofmann, R. Lucic and B. Predel, *Scripta Met.*, **16** (1982) 1437.

L. M. Clarebrough and C. T. Forwood, *phys. stat. sol.*, **60** (1980) 51.

G. Cliff and G. W. Lorimer, *J. Microsc.*, **103** (1975) 203.

G. Cliff and G. W. Lorimer, in *Quantitative Microanalysis with High Spatial Resolution*, (edited by G. W. Lorimer, M. H. Jacobs and P. Doig), Metals Society, Manchester, 1981, p. 47.

C. Colliex, M. Tence, E. Lefevre, C. Mory, H. Gui, D. Bouchet and C. Jeanguillaume, *Mikrochim. Acta*, **114/115** (1994) 71.

A. V. Crewe, *Ultramicroscopy*, **23** (1987) 159.

P. Doig and P. E. J. Flewitt, *J. Microsc.*, **112** (1977) 257.

P. Doig and P. E. J. Flewitt, *Met. Trans. A*, **13** (1982) 1397.

P. Doig, D. Lonsdale and P. E. J. Flewitt, *Phil. Mag. A*, **41** (1980) 761.

P. Doig, D. Lonsdale and P. E. J. Flewitt, in *Quantitative Microanalysis with High Spatial Resolution*, (edited by G. W. Lorimer, M. H. Jacobs and P. Doig), Metals Society, Manchester, 1981, p. 41.

A. M. Donald and L. M. Brown, *Acta metall.*, **27** (1979) 59.

A. M. Donald and A. J. Craven, *Phil. Mag.*, **39** (1979) 1.

M. E. Eberhart, K. H. Johnson and R. M. Latanision, *Acta metall.*, **32** (1984) 955.

R. F. Egerton, *Electron Energy Loss Spectroscopy in the Electron Microscope*, Plenum Press, New York and London, 1996.

R. F. Egerton and M. J. Whelan, *J. Electron Spectrosc.*, **3** (1974) 232.

J. Fang, A. M. Thompson, M. P. Harmer and H. M. Chan, *J. Am. Ceram. Soc.*, **80** (1997) 2005.

R. G. Faulkner and T. C. Hopkins, *X-Ray Spectrometry*, **6** (1977) 73.

T. G. Ference and R. W. Ballufi, *Scripta Met.*, **22** (1988) 1929.

F. Fink, N. Nücker, E. Pelligrin, H. Romberg, M. Alexander and M. Knupfer, *J. Electron Spectrosc.*, **66** (1994) 395.

S. Floreen and J. H. Westbrook, *Acta metall.*, **17** (1969) 1175.

C. T. Forwood and L. M. Clarebrough, *Acta metall.*, **32** (1984) 757.

R. H. Fowler and E. A. Guggenheim, *Statistical Mechanics*, Cambridge University Press, Cambridge, 1939.

A. Fraczkiewicz and M. Biscondi, *J. de Phys.*, **C4** (1985) 497.

A. P. French and E. F. Taylor, *An Introduction to Quantum Mechanics*, Van Nostrum Reinhold, London, 1979.

J. I. Goldstein, J. L. Costley, G. W. Lorimer and S. J. B. Reed, in *Scanning Electron Microscopy*, (edited by O. Johari), IITRI, Chicago, 1977, p. 315.

J. I. Goldstein, D. B. Williams and G. Cliff, in *Principles of Analytical Electron Microscopy*, (edited by D. C. Joy, A. D. Romig and J. I. Goldstein), Plenum Press, New York and London, 1986, p. 155.

M. Grioni, J. B. Goedkoop, R. Schoorl, R. M. F. d. Groot, J. C. Fuggle, F. Schafers, E. E. Koch, G. Rossi, J. M. Esteva and R. C. Karnatak, *Phys. Rev B*, **39** (1989) 1541.

M. Grioni, J. F. van Acker, M. T. Czyzyk and J. C. Fuggle, *Phys. Rev. B*, **45** (1992) 3309.

C. R. M. Grovenor, P. E. Batson, D. A. Smith and C. Wong, *Phil. Mag. A*, **50** (1984) 409.

C. R. M. Grovenor and C. M. F. Rae, *Scripta Met.*, **15** (1981) 1305.

M. Hagiwara and J. Chene, *Scripta Met.*, **18** (1984) 877.

R. Halimi and A. Merabet, *C. de Phys.*, **C1 51** (1990) 501.

E. L. Hall, D. Imeson and J. B. Vander Sande, *Phil. Mag. A*, **43** (1981) 1569.

K. R. Hallam and R. K. Wild, *Surface and Interface Analysis*, **23** (1995) 133.

W. Hampe, *Z. Berg-Hütten u. Salinen-Wesen*, **22** (1874) 93.

M. Hashimoto, Y. Ishida, S. Wakayama, R. Yamamoto, M. Doyama and T. Fujiwara, *Acta metall.*, **32** (1984) 13.

M. B. Hintz, L. A. Heldt, S. P. Clough and J. F. Moulder, *Scripta Met.*, **17** (1983) 1415.

J. P. Hirth and J. R. Rice, *Met. Trans. A*, **11A** (1980) 1501.

J. E. Hoffmann, *JOM*, **46** (1994) 10.

S. Hofmann, *Vacuum*, **40** (1990) 9.

E. D. Hondros and D. McLean, *Phil. Mag.*, **29** (1974) 771.

E. D. Hondros and M. P. Seah, *Int. Metals Rev.*, **222** (1977) 262.

E. D. Hondros and M. P. Seah, *Met. Trans.*, **8A** (1977) 1363.

E. D. Hondros and M. P. Seah, in *Physical Metallurgy*, (edited by R. W. Vahn and P. Haasen), North Holland, Amsterdam, 1983.

R. K. Hotzler and L. S. Castleman, *Met. Trans.*, **3** (1972) 2561.

J. A. Hunt and D. B. Williams, *Ultramicroscopy*, **38** (1991) 47.

R. Hutchings, M. H. Loretto, I. P. Jones and R. E. Smallman, *Ultramicroscopy*, **3** (1979) 401.

J. S. Ikeda, Y.-M. Chiang, A. J. Garratt-Reed and J. B. Vander Sande, *J. Amer. Ceram. Soc.*, **76** (1993) 2447.

M. C. Inman, D. McLean and H. R. Tipler, *Proc. Roy. Soc. A*, **273** (1963) 538.

Y. Ishida and M. Mori, *J. de Phys.*, **C4** (1985) 465.

C. Jeanguillaume and C. Colliex, *Ultramicroscopy*, **28** (1989) 252.

W. C. Johnson, *Scripta Met.*, **8** (1974) 971.

R. H. Jones, S. M. Bruemmer, M. T. Thomas and D. R. Baer, *Proceedings of Third International Conference on the Effect of Hydrogen on the Behavior of Materials*, (edited by I. M. Bernstein and A. W. Thompson), TMS-AIME, 1980, p. 369.

A. Joshi and D. F. Stein, *J. Inst. Metals*, **99** (1971) 178.

D. C. Joy, *Monte Carlo Modelling for Electron Microscopy and Microanalysis*, Oxford University Press, New York, 1995.

V. J. Keast, M.S. Thesis, Lehigh University (1996).

V. J. Keast, J. Bruley, P. Rez, J. M. Maclaren and D. B. Williams, *Acta Mat.*, **46** (1998) 481.

V. J. Keast, T. E. Mitchell, H. Kung and A. Misra, (1998) submitted for publication in Proceedings of ICEM 98.

H. Kimura, K. Abiko, S. Suzuki, M. Obata, J. Kumagai and H. Kimura, *Proceedings of JIMIS-4, Grain Boundary Structure and Related Properties*, The Japan Institute of Metals, 1986, p. 53.

B. W. Krakauer and D. N. Seidman, *Materials Science Forum*, **155-156** (1994) 393.

G. L. Krasko and G. B. Olsen, *Solid State Comm.*, **76** (1990) 247.

O. L. Krivanek, C. C. Ahn and R. B. Keeney, *Ultramicroscopy*, **22** (1987) 103.

D. H. Lassila and H. K. Birnbaum, *Acta. metall.*, **35** (1987) 1815.

R. D. Leapman, L. A. Grunes and P. L. Fejes, *Phys. Rev. B*, **26** (1982) 614.

R. D. Leapman and J. A. Hunt, *Microsc. Microanal. Microstruct.*, **2** (1991) 231.

R. D. Leapman, P. Rez and D. F. Mayers, *J. Chem. Phys.*, **72** (1980) 1232.

T. C. Lee, I. M. Robertson and H. K. Birnbaum, *Acta metall.*, **37** (1989) 407.

T. C. Lee, R. Subramanian, I. M. Robertson and H. K. Birnbaum, *Scripta Met. et Mat.*, **25** (1991) 1265.

P. Lejcek and S. Hofmann, *Critical Reviews in Solid State and Materials Sciences*, **20** (1995) 1.

G. Li, X. Wu, M. Cai, Q. Qiu and Q. Tang, *Scripta Met. et Mat.*, **24** (1990) 2129.

C. Loier and J. Boos, *Met. Trans*, **12A** (1981) 1223.

N. J. Long and R. W. Glaisher, *Inst. Phys. Conf. Ser.*, **98** (1990) 277.

W. Losch, *Acta metall.*, **27** (1979) 1885.

D. E. Luzzi, *Phil. Mag. Lett.*, **63** (1991a) 281.

D. E. Luzzi, M. Yan, M. Sob and V. Vitek, *Rhys. Rev. Lett.*, **67** (1991b) 1894.

C. E. Lyman, J. I. Goldstein, D. B. Williams, D. W. Ackland, S. von Harrach, A. W. Nicholls and P. J. Statham, *J. Microsc.*, **176** (1994) 85.

F. W. Lytle and R. B. Greegor, *Phys. Rev. B*, **37** (1988) 1550.

S. T. Manson, in *Topics in Applied Physics Vol 26*, (edited by M. Cardona and L. Ley), Springer Verlag, New York, 1978, p. 135.

H. L. Marcus and N. E. Paton, *Met. Trans.*, **5** (1974) 2135.

D. E. Mason, *Phil. Mag. A*, **39** (1979) 455.

R. Mast, H. J. Grabke, M. Jenko and M. Lucas, in *Intergranular and Interphase Boundaries in Materials*, (edited by A. C. Ferro, J. P. Conde and M. A. Fortes), Transtec Publications, Ltd., Switzerland, 1996, p. 401.

D. McLean, *J. Inst. Metals*, **73** (1947) 791.

D. McLean, *J. Inst. Metals*, **81** (1952) 121.

D. McLean, *Grain Boundaries in Metals*, Clarendon Press, Oxford, 1957.

C. J. McMahon, *Mater. Sci. Eng.*, **25** (1976) 233.

E. S. K. Menon, W. T. Reynolds and A. G. Fox, *Proceedings of Microscopy and Microanalysis*, (edited by G. W. Bailey, R. V. W. Dimlich, K. B. Alexander, J. J. McCarthy and T. P. Pretlow), Springer, Cleveland, Ohio, 1997, p. 553.

M. Menyhard, *Materials Science Forum*, **126-128** (1993) 205.

M. Menyhard and C. J. McMahon, Jr., *Scripta Met. et Mat.*, **25** (1991) 935.

M. Menyhard, B. Rothman, C. J. McMahon, Jr., P. Lejcek and V. Paider, *Acta metall. mater.*, **39** (1991) 1289.

M. Menyhard, M. Yan and V. Vitek, *Acta metall.*, **42** (1994) 2783.

P. D. Merica and R. G. Waltenberg, *U. S. National Bureau of Standards Tech. Paper*, **281** (1925)

R. P. Messmer and C. L. Briant, *Acta metall.*, **30** (1982) 457.

J. R. Michael, C.-H. Lin and S. L. Sass, *Scripta Met.*, **22** (1988) 1121.

J. R. Michael and D. B. Williams, *Met. Trans.*, **15A** (1984) 99.

J. R. Michael and D. B. Williams, *J. Microsc.*, **147** (1987) 289.

J. R. Michael, D. B. Williams, C. F. Klein and R. Ayer, *J. Microsc.*, **160** (1990) 41.

H. Miura, H. Nakata and T. Sakai, *Appl. Phys. Lett.*, **65** (1994) 705.

H. Miura, T. Yoshida, T. Sakai, M. Kato and T. Mori, *J. Japan Inst. Metals*, **57** (1993) 479.

M. Mori and Y. Ishida, *Proceedings of Proceedings of JIMIS-4, Grain Boundary Structure and Related Properties*, The Japan Institute of Metals, 1986, p. 361.

C. Mory, C. Colliex and J. M. Cowley, *Ultramicroscopy*, **21** (1987) 171.

R. A. Mulford, *Met. Trans.*, **14A** (1983) 865.

D. A. Muller, (1998) submitted to Phys. Rev. B.

D. A. Muller, P. E. Batson and J. Silcox, (1998) submitted to Phys. Rev. B.

D. A. Muller, D. J. Singh and J. Silcox, *Phys. Rev. B*, **57** (1998) 8181.

D. A. Muller, S. Subramanian, P. E. Batson, J. Silcox and S. L. Sass, *Acta mater.*, **44** (1996) 1637.

J. E. Muller, O. Jepson and J. W. Wilkins, *Solid State Commun.*, **42** (1982) 365.

A. Neckel, P. Rastl, R. Eibler, P. Weinberger and K. Schwarz, *J. Phys. C*, **9** (1976) 579.

H. Ohtani, H. C. Feng and J. C. J. McMahon, *Met. Trans. A*, **7A** (1976) 1123.

D. Ozkaya, J. Yuan, L. M. Brown and P. E. J. Flewitt, *J, Microsc.*, **180** (1995) 300.

A. Partridge and G. J. Tatlock, *Surface and Interface Analysis*, **18** (1992) 713.

J. H. Paterson and O. L. Krivanek, *Ultramicroscopy*, **32** (1990) 319.

D. H. Pearson, C. C. Ahn and B. Fultz, *Phys. Rev. B*, **47** (1993) 8471.

D. H. Pearson, B. Fultz and C. C. Ahn, *Appl. Phys. Lett.*, **53** (1988) 1405.

B. Peng, X. Wu, F. Zhou and Q. Tang, *J. Appl. Phys.*, **71** (1992) 1229.

D. G. Pettifor, *Bonding and Structure of Molecules and Solids*, Clarendon Press, Oxford, 1995.

N. L. Piret, *JOM*, **46** (1994) 15.

B. D. Powell and H. Mykura, *Acta metall.*, **21** (1973) 1151.

B. D. Powell and D. P. Woodruff, *Phil. Mag.*, **34** (1976) 169.

S. J. B. Reed, *Ultramicroscopy*, **7** (1982) 405.

L. Reimer, *Energy-Filtering Transmission Electron Microscopy*, Springer, Berlin Heidelberg, 1995.

P. Rez, *Ultramicroscopy*, **12** (1983) 29.

P. Rez, in *Transmission Electron Energy Loss Fine Structure in Materials Science*, (edited by M. M. Disko, C. C. Ahn and B. Fultz), TMS, 1992, p. 107.

P. Rez, J. Bruley, P. Brohan, M. Payne and L. A. J. Garvie, *Ultramicroscopy*, **59** (1995) 169.

P. Rez, J. M. MacLaren and D. K. Saldin, *Phys. Rev. B*, **57** (1998) 2621.

J. R. Rice and J.-S. Wang, *Mat. Sci. and Eng.*, **A107** (1989) 23.

J. D. Russell and A. T. Winter, *Scripta Met.*, **19** (1985) 575.

G. A. Sawatzky, *Microsc. Microanal. Microstruct.*, **2** (1991) 153.

J. M. Schoen, J. M. Poate, C. J. Doherty and C. M. Melliar-Smith, *J. Appl. Phys*, **50** (1979) 6910.

E. M. Schulson and I. Baker, in *Ordered Intermetallics-Physical Metallurgy and Mechanical Behaviour*, (edited by C. T. Liu, R. W. Cahn and G. Sautoff), Kluwere Academic Publishers, Netherlands, 1992, p. 371.

M. P. Seah and E. D. Hondros, *Proc. Roy. Soc. Lond. A*, **335** (1973) 191.

J. R. Serrano, D. Berger and J. B. Bridges, *JOM*, **46** (1994) 12.

H. Shuman and A. P. Somylo, *Ultramicroscopy*, **21** (1987) 23.

M. B. Small, D. A. Smith and A. J. Garratt-Reed, *Scripta Met. et Mat.*, **30** (1994) 1531.

A. P. Sutton, *Electronic Structure of Materials*, Clarendon Press, Oxford, 1993.

J. M. Titchmarsh, *Proceedings of 11th ICXOM*, London, Ontario, 1986, p. 337.

J. M. Titchmarsh, in *Microbeam Analysis*, (edited by D. E. Newbury), San Francisco Press, 1988, p. 65.

J. M. Titchmarsh, *Ultramicroscopy*, **28** (1989) 347.

J. M. Titchmarsh and S. Dumbill, *J. Microsc.*, **184** (1996) 195.

J. M. Titchmarsh and S. Dumbill, *Journal of Nuclear Materials*, **227** (1996) 203.

J. M. Titchmarsh and S. Dumbill, *J. Microsc.*, **188** (1997) 224.

N. H. Turner, in *Inverstigations of Surfaces and Interfaces - Part B*, (edited by B. W. Rossiter and R. C. Baetzold), John Wiley and Sons, 1993, p. 123.

E. Van Cappellan and A. Schmitz, *Ultramicroscopy*, **41** (1992) 193.

J. D. Vander Sande, A. J. Garratt-Reed, Y.-M. Chiang and T. Thorvaldsson, *Ultramicroscopy*, **14** (1984) 65.

I. A. Vatter and J. M. Titchmarsh, *Ultramicroscopy*, **28** (1989) 236.

I. A. Vatter and J. M. Titchmarsh, *Surface and Interface Analysis*, **25** (1997) 760.

V. Vitek, G. J. Ackland, M. Meynhard and M. Yan, in *Interfaces:Structure and Properties*, (edited by S. Ranganathan), Trans Tech Publications, New Delhi, 1993, p. 3.

E. Voce and A. P. C. Hallowes, *J. Inst. Metals*, **73** (1947) 323.

D. D. Vvedensky, D. K. Saldin and J. B. Pendry, *Comput. Phys. Commun.*, **40** (1986) 421.

J. Wang and P. M. Anderson, *Acta metall.*, **39** (1991) 779.

X. Weng and P. Rez, *Phys. Rev. B*, **39** (1988) 7405.

X. Weng, P. Rez and O. F. Sankey, *Phys. Rev. B*, **40** (1989) 5694.

D. B. Williams and C. B. Carter, *Transmission Electron Microscopy: A Textbook for Materials Science*, Plenum Press, New York and London, 1997.

D. B. Williams and A. D. Romig, *Ultramicroscopy*, **30** (1989) 38.

D. B. Williams, M. Watanabe, D. T. Carpenter and K. Barmak, *Mikrochim. Acta*, (1997) in press.

J. E. Wood, D. B. Williams and J. I. Goldstein, *J. Microsc.*, **133** (1984) 255.

R. Wu and A. J. Freeman, *Phys. Rev. B*, **50** (1994) 75.

R. Wu, A. J. Freeman and G. B. Olsen, *Science*, **265** (1994) 376.

K. S. Yu, A. Joshi and W. D. Nix, *Met. Trans.*, **14A** (1983) 2447.

N. J. Zaluzec, *Ultramicroscopy*, **9** (1982) 319.

## APPENDIX A. Measurement of Probe Sizes

In a convential TEM or a TEM/STEM, measurement of probe sizes is relatively straightforward as an image of the electron probe can be formed on the screen or camera and the probe size measured directly. In a dedicated STEM it is nor possible to directly image the incident beam and it must instead be measured through some indirect means. In an analogous way to probe size measurements in an SEM (Joy (1974), Vaughan (1976)) the probe can be scanned over a knife-edge and the resultant intensity profile measured. MgO crystals have been suggested as a suitable specimen for such measurements in the STEM (Michael and Williams (1987).)

Figure A.1 shows an example of the intensity recorded by the ADF detector as the probe was scanned across the edge of a very small, thin MgO crystal where the edge of the crystal was aligned as closely as possible parallel to the electron beam. This particular example was taken with the 30 μm VOA, at 300 keV and with only the 2nd condenser lens excited.

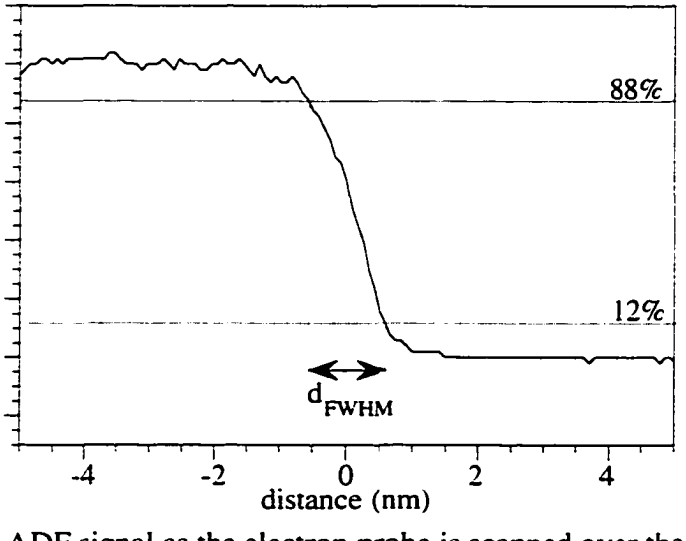


Figure A.1 ADF signal as the electron probe is scanned over the sharp edge of a thin MgO crystal aligned with its edge prallel to the incident beam.

As described in Joy (1974), Michael and Williams (1987) the FWHM of a gaussian probe is given by the distance between the 12% and 88% levels on the intensity profile (as indicated in Figure A.1). The probe size at FWTM can be measured from the 1.75% and 98.25% levels but, due to noise it is easier and more accurate to measure the FWHM value and multiply by 1.82 to obtain the FWTM. In order to the obtain the measurements shown in Figure * of probe size under a variety of electron optical conditions, a number of scans (6-10) were taken for each condition. An average of these measurements was used, neglecting the 1-2 largest measurements and errors were assessed based on the standard deviation.

A large number of measurements of the probe size for the usual operating conditions of the VG 603 (30 μm VOA, 2nd condenser lens only) have been made as part of a larger experiment to determine how brightness varies with accelerating voltage (Watanabe and Williams (1998)). The brightness was then assessed by

$$\beta = \frac{4i_b}{\pi^2\alpha^2 {d_g}^2} \qquad (A.1)$$

where the gaussian probe size was obtained from the measured probe size $d_{exp}$ using

$${d_g}^2 = {d_{exp}}^2 - \left(\frac{1}{2}C_s\alpha^3\right)^2 - \left(1.22\frac{\lambda}{\alpha}\right)^2 \qquad (A.2)$$

The probe current was measured using a Faraday cup in the plane of the selected area aperture. The convergence angle was determined by measuring the diameter of the spots in the microdiffraction pattern relative to the known spacing between the spots. The sample used for convergence angle measurements was single crystal Si. In this way the brightness was found to be 0.34 x $10^{13}$ A/m$^2$/sr. This value is 3 times smaller the nominal value of 1.0 x $10^{13}$ A/m$^2$/sr but is not inconsistent with measurement 0.8 x $10^{13}$ A/m$^2$/sr of Michael and Williams (1987) when this value is converted to account for probe size measured at FWTM rather than FWHM. The measured value of

brightness was used throughout the dissertation as it is believed to be the most appropriate.

## APPENDIX B. Diffusion into a Planar Slab

The diffusion of a species into a planar slab of width 2L can be imagined as shown in Figure B.1, where superimposed on the shape of the slab is the expected type of concentration profile, C(x,t) for some time, t > 0.

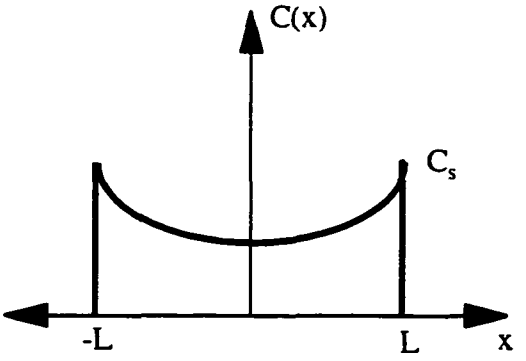


Figure B.1 Schematic of diffusion into a planar slab of width 2L.

We assume an infinite supply of the diffusing species at the surface, which will give the boundary conditions $C(L,t)=C(-L,t)=C_S$ for all t. We also have $C(x,0) = 0$ for $-L<x<L$. A concentration profile that satisfies the diffusion equation

$$\frac{\partial C(x,t)}{\partial t} = D\frac{\partial^2 C(x,t)}{\partial x^2} \qquad (B.1)$$

and these boundary conditions is

$$C(x,t) = C_S\left[2 - \mathrm{erf}\left(\frac{x+L}{2\sqrt{Dt}}\right) - \mathrm{erf}\left(\frac{-(x-L)}{2\sqrt{Dt}}\right)\right] \qquad (B.2)$$

A reasonable assumption for complete diffusion into the foil is that at the concentration at the centre is 90% of the value of the surface, i.e. $C(0,t)=0.9C_S$. In which case

$$0.9C_S = C_S\left[2 - 2\mathrm{erf}\left(\frac{L}{2\sqrt{Dt}}\right)\right]$$

which simplifies to

$$t = 0.86\frac{L^2}{D} \qquad (B.3)$$

## VITA

Vicki J. Keast was born to Bill and Sally Keast on 29th March 1971 in Adelaide, Australia. She completed her secondary education at Pennant Hills High School, Sydney, Australia in 1988. During 1989 she pursued a career in acountancy working at Deloitte Ross Tohmatsu and studying for a Bachelor of Business at the University of Technology. In 1990 she realized the error of her ways and entered the University of Sydney from which she graduated in 1993 with a Bachelor of Science with 1st Class Honours in Physics.

Her graduate studies started in May 1994 in the Department of Materials Science and Engineering at Lehigh University. She received her M.S. in June 1996 and spent the Summer of 1997 at Los Alamos National Laboratory. In July 1998 she started a post-doctoral position at the University of Cambridge, England.

# IMAGE EVALUATION TEST TARGET (QA-3)

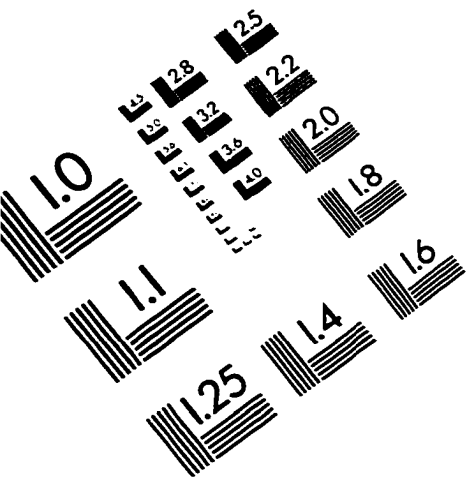


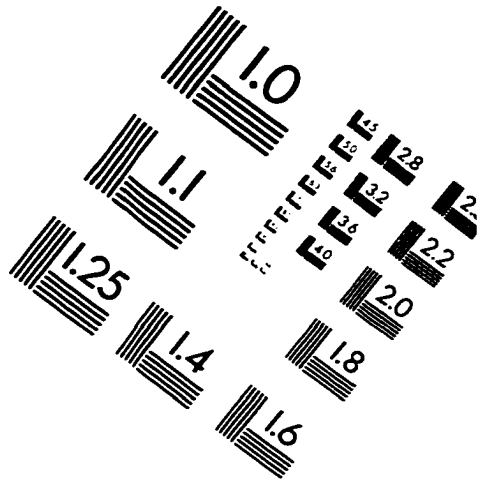


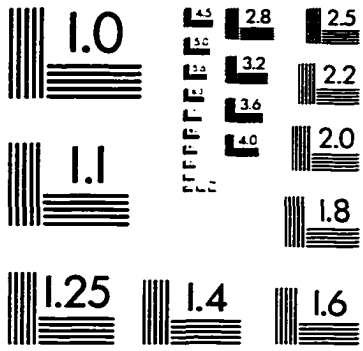


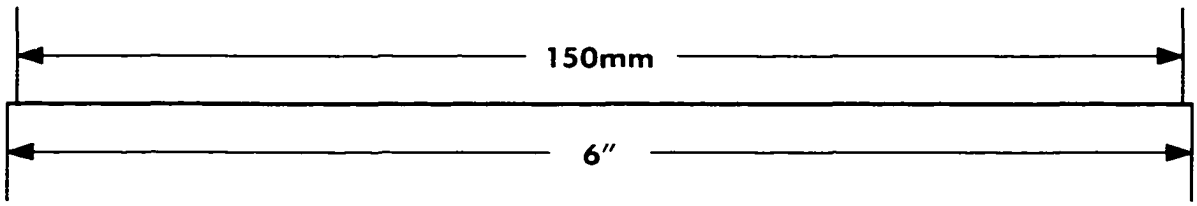


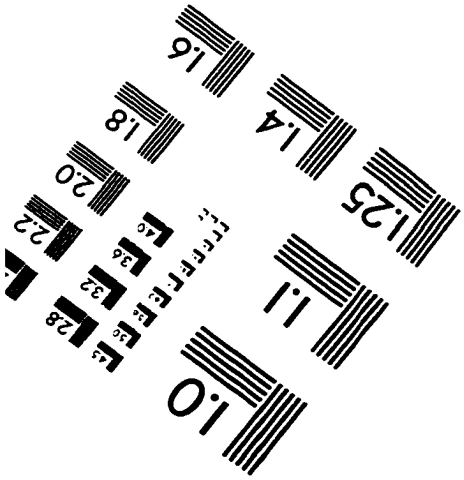


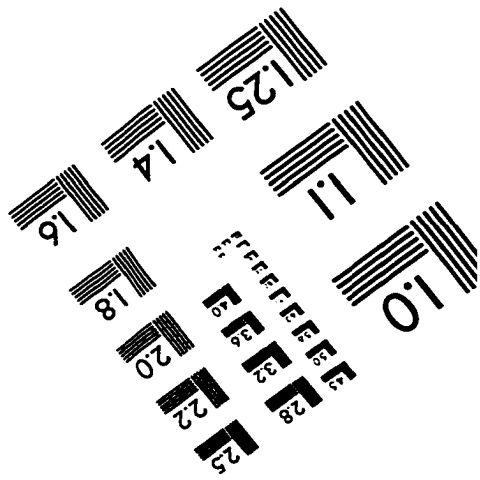


APPLIED IMAGE, Inc
1653 East Main Street
Rochester, NY 14609 USA
Phone: 716/482-0300
Fax: 716/288-5989